INFORMATION TO USERS

This manuscript has been reproduced from the microfilm master. UMI films the text directly from the original or copy submitted. Thus, some thesis and dissertation copies are in typewriter face, while others may be from any type of computer printer.

The quality of this reproduction is dependent upon the quality of the copy submitted. Broken or indistinct print, colored or poor quality illustrations and photographs, print bleedthrough, substandard margins, and improper alignment can adversely affect reproduction.

In the unlikely event that the author did not send UMI a complete manuscript and there are missing pages, these will be noted. Also, if unauthorized copyright material had to be removed, a note will indicate the deletion.

Oversize materials (e.g., maps, drawings, charts) are reproduced by sectioning the original, beginning at the upper left-hand corner and continuing from left to right in equal sections with small overlaps.

ProQuest Information and Learning
300 North Zeeb Road, Ann Arbor, MI 48106-1346 USA
800-521-0600

THE TRANSMISSION LINE MATRIX (TLM) METHOD AND ITS BOUNDARY TREATMENTS

By

ZHIZHANG CHEN

A thesis submitted to the
School of Graduate Studies and Research
in partial fulfillment of the requirements for the degree of

Doctor of Philosophy

in

Electrical Engineering

Ottawa-Carleton Institute for Electrical Engineering

Department of Electrical Engineering
Faculty of Engineering
University of Ottawa

To my grandmother
and to my mother and father

I hereby declare that I am the sole author of this document. I authorize the University of Ottawa to lend this document to other individuals or institutions for the purposes of scholarly research.

I further authorize the University of Ottawa to reproduce this document by photocopying or by other means, in total or in part, at the request of other institutions or individuals for the purposes of scholarly research.

Acknowledgments

It is a pleasure to express the author's sincere gratitude to his supervisors Dr. Michel M. Ney and Dr. Wolfgang J. R. Hoefer for their encouragement and invaluable expert guidance throughout this work. It has been a great honor and a privilege to work with them.

The author would also like to thank the advisory committee members Dr. G. I. Costache and Dr. B. A. Syrett for their many useful suggestions and discussions.

The author is grateful to all the members of Microwave group for their help and encouragement. A special note of thanks is due to P. So for his useful discussions and M. Fitzmaurice for his willingness to read the manuscript and give constructive comments.

The author wishes to thank Profs. D. C. Fang, C. G. Zhang and J. M. Shi in Fuzhou University for their assistance in making it possible for me to study at the University of Ottawa.

The author would like to acknowledge the financial assistance from the Telecommunications Research Institute of Ontario and the Scholarship from the Government of Ontario.

Last, but by no means least, the author would like to express his sincere thanks to his wife and his parents. It would not have been possible to finish this long-term work without their support.

Abstract

The Transmission Line Matrix (TLM) numerical algorithm, based on the discrete Huygens' principle, has been extensively used to solve electromagnetic structure problems. The major advantage of this method is its simplicity and flexibility as the vectorial Maxwell's Equations are transformed into a simple numerical model of digital signal processing system.

In this thesis, new and efficient numerical modeling concepts and procedures have been developed for the analysis of electromagnetic structures with the TLM method:

- With the introduction of the equivalent field quantities defined between nodes, the TLM Method has been shown to be exactly equivalent to a finite-difference time-domain (FD-TD) formulation. Therefore, the numerical foundation of the TLM approach has been fully demonstrated and the basis for mathematically understanding the TLM method has been provided. As a result, the conventional TLM boundary conditions has been verified theoretically, and hence a systematic way for constructing the TLM boundary conditions has been developed. In addition, a new boundary description for the TLM method has been proposed, which renders TLM method more flexibility in its boundary treatments.

- Based on the equivalence between the TLM method and the FD-TD method, an absorbing and a connecting boundary formulations have been developed for TLM simulations. With these formulations, the TLM method can be applied for solving more realistic scattering and radiation problems with open structures. The computation examples given in this thesis are with the structures of waveguides, two-dimensional and three-dimensional obstacles illuminated by plane waves. The numerical results show good agreement with those obtained with the Method of Moment, and thus validate the boundary conditions developed.

- By using the discrete Fourier Transform, a new algorithm has been developed for interfacing the TLM method with the frequency-domain solutions. The technique employ the *prior* knowledge of frequency-domain solutions at boundaries and combine them with TLM simulations, leading to considerable decrease in memory and CPU time. It also allows the TLM method to be used with highly conductive materials for solving shielding problems. The good results were obtained with significant reduction of the computation expenditure.

Contents

List of Figures

List of Tables

Chapter 1

Introduction

Numerical models for electromagnetic structures consisting of transmission media and their boundaries are needed for computer simulation of wave propagation. In the past, various analytical methods such as Green's function technique, conformal mapping, variational methods, Fourier transform method, Fourier integral approach, spectral domain method, and mode matching technique have been used to solve electromagnetic problems. However, these methods can not be applied to the problems with arbitrary geometry. Furthermore, the realistic features such as finite metallization thickness, mounting groove, and irregularities caused during manufacturing, cannot be easily accounted for. Therefore, very accurate characterization numerical techniques are essential to model the problems.

Numerical techniques such as the Finite Element Method (FEM), the Method of Moment (MoM), the Boundary Element Method (BEM), the Finite-Difference Frequency-Domain (FD-FD) Method, the Transmission Line Matrix (TLM) Method, and the Finite-Difference Time-Domain (FD-TD) Method have evolved in the last two decades. Recent advances in modeling concepts and technology have expanded the scope, accuracy and speed of these methods thanks to the development of powerful computers. Programs based on these techniques can be applied to solve problems with structures which the analytical approaches can not deal with. Two very useful reviews and extensive lists of references in this area can be found in [1] and [2].

As one of the numerical techniques, the TLM method has received growing international attention and found wide range of applications since P. B. Johns introduced it for solving electromagnetic structure problems in 1971 [3]. The reasons are that, firstly, the solution is solved in a sequential manner, and therefore, is very appropriate for computer operations and programming; secondly, it can be applied easily to problems with com-

plex structures which would be very difficult to solve with either analytical approaches or the other numerical techniques (the electromagnetic problem need not to be reformulated for every new structure; its parameters are simply entered in a general-purposed program in the form of codes for boundaries, permeabilities, permittivities, and excitation of the fields); Thirdly, it provides direct time-domain solutions for transient problems (as a result, to obtain the frequency-domain results over a wide range of spectrum, only one simulation or a single shot of computation are needed). Fourthly, it can account, without changing the basic algorithm significantly, for inhomogeneous, lossy, anisotropic, nonlinear, time-varying and even dispersive media. The main disadvantage of the method is its requirement for large computer memory space and long computation time for three-dimensional and large scale two dimensional problems. Overcoming of the difficulty rests on two aspects: the development of super computers and improvement on the method itself.

1.1 State of the Art

As early as in the forth decade of this century, several researchers made use of electrical networks to simulate electromagnetic wave propagation in two-dimensional (2D) waveguides [4]-[6]. The principle involved in these methods was based on the similarity between the behavior of electromagnetic fields and voltages and currents in spatial electrical networks. Inspired by these techniques, P.B. Johns and his co-workers proposed, in 1971, a novel numerical procedure [3] to solve the 2D electromagnetic problems, in which both space and time are discretized. Later on in his paper [7], P.B. Johns showed that the method is actually the time-domain model embodying the Huygens' principle in discretized form. It uses an equivalent network, or matrix, of either shunt or series interconnecting two-wire transmission lines (the method is then called the Transmission-Line-Matrix (TLM) method). At the interconnecting points (or nodes) of the transmission lines, a number of stubs, whose electrical properties are used to represent the electrical characteristics of propagation space, are attached. Analysis of the transmission line matrix leads to a system of equations. These equations can be identified with the 2D Maxwell's equations by drawing equivalences between circuit quantities in the 2D TLM network (such as node voltages, currents, line constants, and stub parameters), and the field quantities in the media (such as electric fields, magnetic fields, permittivity and permeability). The numerical procedure

entails by exciting the network, or mesh, at specific points with impulses. Then, at each subsequent time step, these impulses propagate through the transmission lines connecting two neighbor nodes, scatter at the nodes and bounce back at the boundaries. The output, which is taken from a chosen node, consists of a series of impulses separated by a constant time interval. The Fourier transform of this output function can be performed to obtain the spectral domain solution.

By the end of 1974, Johns and Akhtarzad [8, 9] had extended the 2D TLM scheme to three dimensions (3D) by alternatively shunt and series interconnecting the two-wire transmission lines in 3D space. The voltages and currents at the interconnecting points (or nodes) are equivalent to electric and magnetic fields, respectively. In this way, the equivalent six E and H field components are defined in space alternatively and separately with each other. The model is called the 3D TLM expanded or distributed node .

In 1982, Saguet and Pic [10] developed the 3D asymmetrical condensed node structure by modifying the 3D expanded node model. The network topology is simply a three-dimensional Cartesian mesh with two pairs of two-wire transmission lines, corresponding to two polarizations, in each branch. It follows that all of the field components are defined at one point (condensed), and boundary conditions can be applied halfway between nodes. However, this node model is asymmetrical in the sense that the first connection in the node is either shunt or series depending upon the direction of view. Although the errors caused by the asymmetry are insignificant for most problems [12], it does mean that boundaries viewed in one direction have slightly different properties when viewed in another. In 1986, P.B. Johns [13, 14] took yet another step and described the development of a 3D symmetrical condensed node for TLM modeling with lossless media. This node eliminates the disadvantages of asymmetry while preserving the advantages of the condensed node working. Based on this, Naylor and Desai [15] (1990) have added the loss feature to the 3D TLM symmetrical condensed node to account for lossy media. At this stage, basic formulations for the 2D and 3D TLM models have been fully developed.

Building upon the work of these authors, other researchers added other kinds of features and improvements. For example, variable mesh size [16, 17, 18] allows the propagation space to be irregularly graded for discretization according to the nature of problems under investigation. Simplified nodes [19] uses a scalar TLM network to simulate a single field component or a Hertzian potential rather than all the field components. Error correction

techniques [20] employs extrapolation techniques to obtain good accuracy. Time-domain diakoptics [22] apply substructuring techniques to store information for substructures and to form the solution by later on reconnecting the substructures. And stub techniques change stub parameters in the TLM models to solve anisotropic media [23] and non-linear problems [24]. A very useful review of the TLM method of analysis was presented in [25] by Hoefer in 1985. Ever since then, a number of new developments for the TLM method were achieved. Among them are the use of discrete time-domain Green's function (Johns matrix) [26, 27, 28], application of wide-band absorbing boundaries [29, 30], combination of fine-coarse mesh [31], computation time reduction technique with Prony-Pisarenko method [32], modeling of nonlinear active regions [33, 34], simulation of dispersive media[35], Hexagonal TLM model with less numerical dispersion [36] and numerical synthesis by reversing TLM algorithm [37].

1.2 The Motivation and the Original Contributions

In spite of many successful applications and developments of the TLM method [3]-[54], the theoretical foundation of TLM, especially for the 3D symmetrical condensed node model, has not been fully demonstrated, although some work was done by P.B. Johns for the expanded node [61, 62]. In other words, the physical relationships between the field quantities and voltage impulses in the TLM network have not been fully explained, at least mathematically. This had lead to some confusions of understanding the TLM modeling as indicated in [7].

Meanwhile, over the past decades, another numerical time-domain technique, the finite-difference time-domain (FD-TD) method, has been widely used for solving electromagnetic problems. This FD-TD method, introduced by Yee [55], is an approximate discrete mathematical model and is formulated by directly differencing Maxwell's equations under Yee's grid arrangements. The applications of this method have been ranging from solutions of scattering fields [56, 57] to determination of characteristics of planar circuits [58]. A useful introduction and review of this technique was presented by Taflove in [59] and [60].

While the origins of the TLM method and the FD-TD method are different, both of them present the same kind of numerical time-stepping technique and yield practically identical results. Therefore, they would be equivalent in a certain way. Indeed, an equiva-

lence under certain conditions was shown between the 3D TLM expanded node model and the 3D FD-TD method based on Yee's scheme [62]. However, for the TLM symmetrical condensed node, no equivalence has been reported so far. The issue is addressed in this thesis and the equivalence between the TLM method and a new FD-TD formulation has been demonstrated in general. In other words, any TLM algorithm can be rewritten in an equivalent FD-TD form (Chapter 2). Therefore, the theoretical foundation of the TLM has been explored. Based on this, new concepts and procedures for the TLM simulations have been developed in this thesis:

- The conventional boundary conditions of TLM method have been verified theoretically for the first time; a systematic way to construct the boundary conditions for the TLM method is developed; and the conversion of the TLM solutions is presented. In addition, a new boundary description for the TLM method has been proposed where boundaries are placed at nodes instead of half-way between nodes. It renders the TLM method more flexibility in treating, or positioning, its boundaries (Chapter 3).

- As a consequence of the equivalence between the FD-TD approach and the TLM method, numerical techniques employed in the FD-TD method and the TLM method can be trans-implemented into each other after appropriate modifications. Hence, the absorbing boundary conditions and connecting boundary conditions developed for the FD-TD method have been modified and reformulated for TLM modeling. The instabilities resulting from the spurious modes in the TLM model were discussed and additional factors were introduced into the absorbing boundary conditions to suppress the spurious effects. Validations of these boundary conditions were obtained with conducting obstacles illuminated by plane waves in two and three dimensions (Chapter 4).

- A new procedure for interfacing the TLM method with frequency-domain solutions is proposed. It employs the *prior* knowledge of frequency-domain solutions at boundaries and incorporated them with the TLM simulations. Consequently, it achieves considerable reduction of memory and computation time. This implies that the difficulties in some applications of the TLM method can be circumvented by taking advantage of the other techniques. For example, practically impossible implementation of TLM network in a highly conductive sheet (which would require too many

nodes and iterations) can now be accomplished by incorporating a lossy transsimission line section with the TLM mesh. The simulation results have demonstrated the efficiency of the proposed procedure (Chapter 5).

1.3 Organization of This Thesis

This thesis is divided into six chapters, where Chapter II, III, IV and V contain the main original contributions of my work.

In Chapter II, the equivalence between the TLM method and a finite-difference time-domain formulation is explored. It is concluded that the TLM method can be generally formulated in a finite-difference form. Therefore, the quantities, such as impulses, in the TLM modeling are directly related to field quantities. Additionally, the conversion of the TLM solutions to its supposed simulation solutions is derived theoretically.

In chapter III, general boundary treatments for the TLM method have been presented as result of Chapter II. The conventional boundary conditions of the TLM method are verified theoretically. A new boundary description for the TLM simulation, where the boundaries are placed at nodes rather than half-way between nodes, is proposed.

In Chapter IV, the general absorbing boundary conditions and connecting boundary conditions for the TLM method are formulated based on the corresponding FD-TD scheme. Since spurious modes exist in the 3D SCN model, unstable solutions may occur if the absorbing boundary conditions for FD-TD method are directly implemented. Consequently, additional conditions have been introduced in order to suppress the spurious effects. Validations are shown with scattering problems of obstacles illuminated by plane waves in two dimensions and three dimensions.

In Chapter V, a new procedure for interfacing the TLM method with frequency-domain solutions is described. It can be used with problems where boundary conditions in frequency-domain are known. A complete set of the formulations and some numerical results have been given. It is found that in certain situations, memory and CPU time are significantly reduced with this approach.

Finally, Chapter VI contains the overall review, conclusions and future work.

Chapter 2

Numerical Modeling: The TLM Method And The Equivalent New Finite-Difference Time-Domain (FD-TD) Formulations

2.1 Introduction

The TLM method is one of the most appropriate techniques for digital computer simulation of wave motion and has found many applications in microwave and millimeter-wave circuits, such as resonators [42], dielectric-loaded waveguides [20], microstrip lines on isotropic and anisotropic substrates [23, 41]. As mentioned before, due to different techniques used, different TLM models, such as 2D shunt and series node [3], 3D expanded node [8, 9], 3D asymmetric condensed node [10] and more recently 3D symmetrical condensed node (SCN) [14, 15], have been developed. Each model retains its own advantages and disadvantages.

In 1987, Johns [61, 62] showed that under certain conditions, the TLM expanded-node model is equivalent to the FD-TD algorithm of Yee's scheme [55]. In 1990, Voelker and Lomax [63] actually formulated the 3D expanded-node TLM model in a FD-TD form and successfully applied it to solve a nonlinear device problem. However, to the best of author's knowledge, the direct relationships between quantities of the TLM algorithm and the field components have not been fully demonstrated so far, especially for the 3D symmetrical condensed node.

This chapter shows the numerical equivalence between the symmetrical condensed code used in the TLM method and a new FD-TD formulation which is different from the FD-

TD approach of Yee's scheme [55]. That is, the TLM method can be shown to be exactly correspondent to a finite-difference formulation. Hence, the numerical foundation of the TLM is fully demonstrated and the work presented by P.B. Johns for showing equivalence between the expanded TLM-node model and the FD-TD formulations is complemented. It is concluded that due to computation of more field components and fulfillment of continuity conditions, the TLM symmetrical condensed node achieves more accurate modelling and less 3D numerical dispersion than the FD-TD method presently used. In the last section, conversion of the TLM solutions to their corresponding field solutions has been studied.

2.2 The New FD-TD Formulation for Maxwell's - Equations

2.2.1 The two-dimensional (2D) case

First consider the 2D Maxwell's equations for transverse magnetic (TM-to-y) waves in a stationary, lossless and sourceless medium.

$$E_x = E_z = 0, \quad H_y = 0, \tag{2.1}$$

$$-\mu \frac{\partial H_z}{\partial t} = \frac{\partial E_y}{\partial x}, \tag{2.2}$$

$$+\mu \frac{\partial H_x}{\partial t} = \frac{\partial E_y}{\partial z}, \tag{2.3}$$

$$+\varepsilon \frac{\partial E_y}{\partial t} = \frac{\partial H_x}{\partial z} - \frac{\partial H_z}{\partial x} \tag{2.4}$$

where μ and ε are the permittivity and permeability of the medium to be modeled.

Following Yee's notation [55], one can denote a Cartesian grid of points on the x-z plane as

$$(i_x, i_z) = (i_x\, \delta x, i_z\, \delta z) \tag{2.5}$$

and any function of discrete space and time as

$$F(i_x\, \delta x, i_z\, \delta z, n\, \delta t) =_n F(i_x, i_z) \tag{2.6}$$

where $\delta x = \delta z = \delta = c_0 \Delta t$ are the space discretization units (taken to be the same for simplicity), δt is the time increment, $\mu = \mu_r \mu_o$, ε can be chosen to be equal to either $\varepsilon_r \varepsilon_o$ or $2\varepsilon_r \varepsilon_o$ (μ_o and ε_o are the permeability and permittivity of the vacuum media, respectively), and i_x, i_z, n are integers.

Now, the 2-D region is discretized into a mesh shown in Fig.2.1. Unlike Yee's scheme [55], all three nonzero field components, E_y, H_x and H_z, are defined at a node located at the center of the 2D cell, while at the points in between two neighboring nodes (on the boundary contour S), only the magnetic field components tangential to the contour and the electric field normal to the mesh area are considered. As a result, the **E** and **H**-field components are not separated in space but are all defined at the same grid points. This grid arrangement ensures that both the tangential **E** and **H** field components are continuous across the interface of two adjacent cells.

The finite-difference formulations of the 2D Maxwell's equations at node (i_x, i_z), (2.1) to (2.4), are, therefore, as follows:

$$-\mu \frac{{}_{n+1}H_z(i_x, i_z) - {}_{n}H_z(i_x, i_z)}{\delta t} = \frac{{}_{n+\frac{1}{2}}E_y(i_x + \frac{1}{2}, i_z) - {}_{n+\frac{1}{2}}E_y(i_x - \frac{1}{2}, i_z)}{\delta x} \tag{2.7}$$

$$+\mu \frac{{}_{n+1}H_x(i_x, i_z) - {}_{n}H_x(i_x, i_z)}{\delta t} = \frac{{}_{n+\frac{1}{2}}E_y(i_x, i_z + \frac{1}{2}) - {}_{n+\frac{1}{2}}E_y(i_x, i_z - \frac{1}{2})}{\delta z} \tag{2.8}$$

$$+\varepsilon \frac{{}_{n+1}E_y(i_x, i_z) - {}_{n}E_y(i_x, i_z)}{\delta t} = \frac{{}_{n+\frac{1}{2}}H_x(i_x, i_z + \frac{1}{2}) - {}_{n+\frac{1}{2}}H_x(i_x, i_z - \frac{1}{2})}{\delta z} - \frac{{}_{n+\frac{1}{2}}H_z(i_x + \frac{1}{2}, i_z) - {}_{n+\frac{1}{2}}H_z(i_x - \frac{1}{2}, i_z)}{\delta x} \tag{2.9}$$

From the above equation, the updated values of ${}_{n+1}E_y(i_x, i_z)$, ${}_{n+1}H_z(i_x, i_z)$ and ${}_{n+1}H_x(i_x, i_z)$ at nodes can be obtained from the values of **E** and **H**-fields at the previous time step.

In order to update the E and H-field components at the boundary contour of each cell, additional operations are needed. Here, the following averaging process over time and space, which will be shown to be equivalent to the averaging process in the TLM models, is taken:

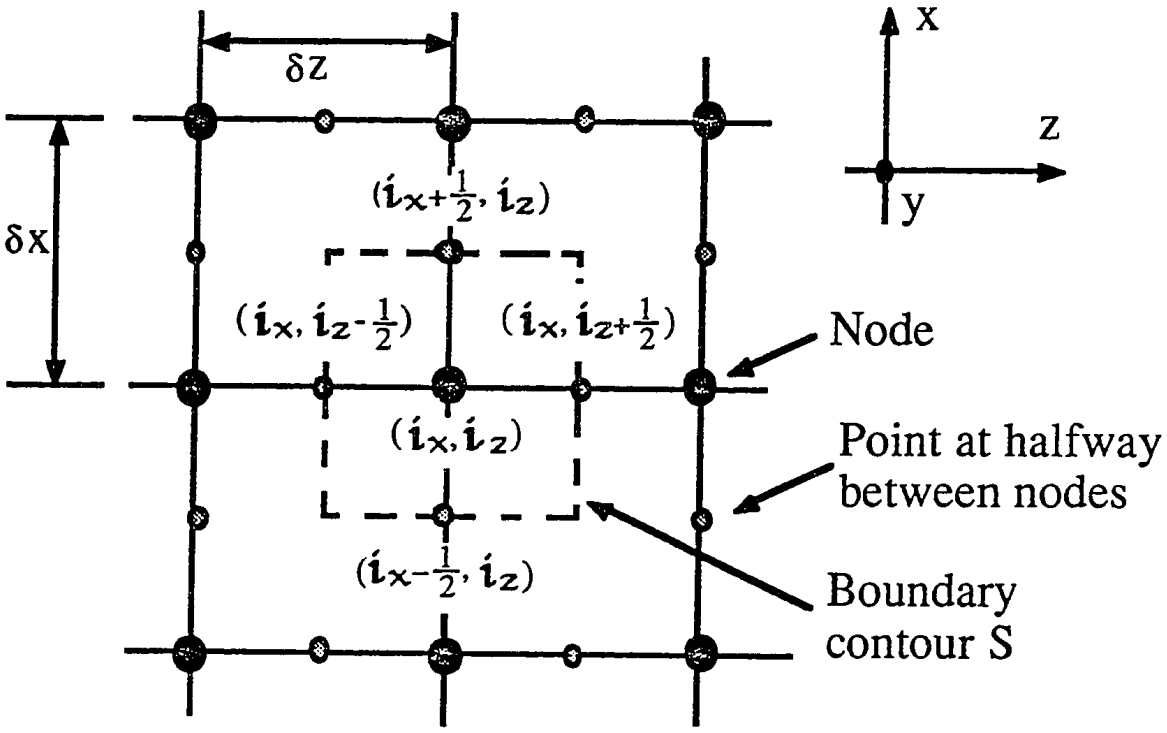

Field components defined (for TM-to-y wave):

$$\text{at } (i_x, i_z) \quad : \quad E_y \ , H_x \ , H_z$$

$$\text{at } (i_x \pm \tfrac{1}{2}, i_z) \quad : \quad E_y \ , H_z$$

$$\text{at } (i_x, i_z \pm \tfrac{1}{2}) \quad : \quad E_y \ , H_x$$

Figure 2.1: Grid Positions for the 2D FD-TD Formulation

$$ {}_nE_y(i_x, i_z) - Z_o \ {}_nH_x(i_x, i_z) = $$
$$ \frac{[{}_{n+\frac{1}{2}}E_y(i_x, i_z + \frac{1}{2}) - Z_o \ {}_{n+\frac{1}{2}}H_x(i_x, i_z + \frac{1}{2})] + [{}_{n-\frac{1}{2}}E_y(i_x, i_z - \frac{1}{2}) - Z_o \ {}_{n-\frac{1}{2}}H_x(i_x, i_z - \frac{1}{2})]}{2} \tag{2.10} $$

$$ {}_nE_y(i_x, i_z + 1) + Z_o \ {}_nH_x(i_x, i_z + 1) = $$
$$ \frac{[{}_{n+\frac{1}{2}}E_y(i_x, i_z + \frac{1}{2}) + Z_o \ {}_{n+\frac{1}{2}}H_x(i_x, i_z + \frac{1}{2})] + [{}_{n-\frac{1}{2}}E_y(i_x, i_z + \frac{3}{2}) + Z_o \ {}_{n-\frac{1}{2}}H_x(i_x, i_z + \frac{3}{2})]}{2} \tag{2.11} $$

$$ {}_nE_y(i_x, i_z) + Z_o \ {}_nH_z(i_x, i_z) = $$
$$ \frac{[{}_{n+\frac{1}{2}}E_y(i_x + \frac{1}{2}, i_z) + Z_o \ {}_{n+\frac{1}{2}}H_z(i_x + \frac{1}{2}, i_z)] + [{}_{n-\frac{1}{2}}E_y(i_x - \frac{1}{2}, i_z) + Z_o \ {}_{n-\frac{1}{2}}H_z(i_x - \frac{1}{2}, i_z)]}{2} \tag{2.12} $$

$$ {}_nE_y(i_x + 1, i_z) - Z_o \ {}_nH_z(i_x + 1, i_z) = $$
$$ \frac{[{}_{n+\frac{1}{2}}E_y(i_x + \frac{1}{2}, i_z) - Z_o \ {}_{n+\frac{1}{2}}H_z(i_x + \frac{1}{2}, i_z)] + [{}_{n-\frac{1}{2}}E_y(i_x + \frac{3}{2}, i_z) - Z_o \ {}_{n-\frac{1}{2}}H_z(i_x + \frac{3}{2}, i_z)]}{2} \tag{2.13} $$

Consequently, the field components between nodes (or on the boundary contour of the 2D cell) can be obtained:

$$ \begin{aligned} {}_{n+\frac{1}{2}}E_y(i_x, i_z + \frac{1}{2}) = & \\ & {}_nE_y(i_x, i_z) - Z_o \ {}_nH_x(i_x, i_z) + {}_nE_y(i_x, i_z + 1) + Z_o \ {}_nH_x(i_x, i_z + 1) \\ & - \frac{1}{2}[{}_{n-\frac{1}{2}}E_y(i_x, i_z - \frac{1}{2}) - Z_o \ {}_{n-\frac{1}{2}}H_x(i_x, i_z - \frac{1}{2}) \\ & + {}_{n-\frac{1}{2}}E_y(i_x, i_z + \frac{3}{2}) + Z_o \ {}_{n-\frac{1}{2}}H_x(i_x, i_z + \frac{3}{2})] \end{aligned} \tag{2.14} $$

$$
\begin{aligned}
Z_o\ {}_{n+\frac{1}{2}}H_x(i_x, i_z+\frac{1}{2}) = \\
&-{}_n E_y(i_x, i_z) + Z_o\ {}_nH_x(i_x, i_z) +{}_n E_y(i_x, i_z+1) + Z_o\ {}_nH_x(i_x, i_z+1) \\
&-\frac{1}{2}[-{}_{n-\frac{1}{2}}E_y(i_x, i_z-\frac{1}{2}) + Z_o\ {}_{n-\frac{1}{2}}H_x(i_x, i_z-\frac{1}{2}) \\
&+{}_{n-\frac{1}{2}}E_y(i_x, i_z+\frac{3}{2}) + Z_o\ {}_{n-\frac{1}{2}}H_x(i_x, i_z+\frac{3}{2})]
\end{aligned} \tag{2.15}
$$

$$
\begin{aligned}
{}_{n+\frac{1}{2}}E_y(i_x+\frac{1}{2}, i_z) = \\
&{}_nE_y(i_x, i_z) + Z_o\ {}_nH_z(i_x, i_z) +{}_n E_y(i_x+1, i_z) - Z_o\ {}_nH_z(i_x+1, i_z) \\
&-\frac{1}{2}[{}_{n-\frac{1}{2}}E_y(i_x-\frac{1}{2}, i_z) + Z_o\ {}_{n-\frac{1}{2}}H_z(i_x-\frac{1}{2}, i_z) \\
&+{}_{n-\frac{1}{2}}E_y(i_x+\frac{3}{2}, i_z) - Z_o\ {}_{n-\frac{1}{2}}H_z(i_x+\frac{3}{2}, i_z)]
\end{aligned} \tag{2.16}
$$

$$
\begin{aligned}
Z_o\ {}_{n+\frac{1}{2}}H_z(i_x+\frac{1}{2}, i_z) = \\
&{}_nE_y(i_x, i_z) + Z_o\ {}_nH_z(i_x, i_z) -{}_n E_y(i_x+1, i_z) + Z_o\ {}_nH_z(i_x+1, i_z) \\
&-\frac{1}{2}[{}_{n-\frac{1}{2}}E_y(i_x-\frac{1}{2}, i_z) + Z_o\ {}_{n-\frac{1}{2}}H_z(i_x-\frac{1}{2}, i_z) \\
&-{}_{n-\frac{1}{2}}E_y(i_x+\frac{3}{2}, i_z) + Z_o\ {}_{n-\frac{1}{2}}H_z(i_x+\frac{3}{2}, i_z)]
\end{aligned} \tag{2.17}
$$

where $Z_o = \sqrt{\frac{\mu}{\varepsilon/2}}$ if $\varepsilon = \varepsilon_o\varepsilon_r$ is chosen, or, $Z_o = \sqrt{\frac{\mu}{\varepsilon_0}}$ if $\varepsilon = 2\varepsilon_o\varepsilon_r$ is chosen. It is recommended that $Z_o = \sqrt{\frac{\mu}{\varepsilon_0}}$ and $\varepsilon = 2\varepsilon_o\varepsilon_r$ be chosen (and henceforth applied in this thesis) since (2.10) to (2.17) would be independent of permittivity. Note in this case, the FD-TD scheme virtually simulates a medium of relative permittivity $2\varepsilon_r$ rather than ε_r.

The above averaging process over time and space for (2.10) to (2.13) observes a certain rule: if the cross product of unit vector of **E**-component and unit vector of **H**-component points to the directions at which the averaging takes place, averaging of $E - Z_0\,H$ is considered; otherwise, $E + Z_0\,H_0$ is considered. For example, one may consider E_y and H_x at the boundary point $(i_x, i_z+\frac{1}{2})$ of two cells centered at nodes (i_x, i_z) and (i_x, i_z+1) as shown in Fig.2.2, respectively. Then take $E_y \pm Z_0\,H_x$ as the quantities to be averaged. When the averaging is taken with the quantities at point (i_x, i_z) and $(i_x, i_z-\frac{1}{2})$ (thus, the direction of averaging is $-\mathrm{a}_z$), $E_y - Z_0\,H_x$ is considered noting that $(\mathrm{a}_y \times \mathrm{a}_x)$ points to the direction of the averaging process $(-\mathrm{a}_z)$. When the averaging is taken with the

quantities at point (i_x+1, i_z) and $(i_x, i_z+\frac{3}{2})$ (the direction of averaging is $\mathrm{a_z}$), $E_y + Z_0\, H_x$ is considered noting that $\mathrm{a_y} \times \mathrm{a_x}$ $(=-\mathrm{a_z})$ points to the opposite direction of the averaging process . The resultant are (2.10) and (2.11)

For the transverse electric waves (TE-to-y), similar equations can be obtained.

2.2.2 The three-dimensional (3D) case

For three-dimensional cases, Maxwell's curl equations in a stationary, lossless and sourceless medium in the time-domain are

$$\mu \frac{\partial \mathbf{H}}{\partial t} = -\nabla \times \mathbf{E}, \tag{2.18}$$

$$\varepsilon \frac{\partial \mathbf{E}}{\partial t} = \nabla \times \mathbf{H} \tag{2.19}$$

In a rectangular coordinate system, (2.18) and (2.19) become the following system of scalar equations:

$$\mu \frac{\partial H_x}{\partial t} = \frac{\partial E_y}{\partial z} - \frac{\partial E_z}{\partial y} \tag{2.20}$$

$$\mu \frac{\partial H_y}{\partial t} = \frac{\partial E_z}{\partial x} - \frac{\partial E_x}{\partial z} \tag{2.21}$$

$$\mu \frac{\partial H_z}{\partial t} = \frac{\partial E_x}{\partial y} - \frac{\partial E_y}{\partial x} \tag{2.22}$$

$$\varepsilon \frac{\partial E_x}{\partial t} = \frac{\partial H_z}{\partial y} - \frac{\partial H_y}{\partial z} \tag{2.23}$$

$$\varepsilon \frac{\partial E_y}{\partial t} = \frac{\partial H_x}{\partial z} - \frac{\partial H_z}{\partial x} \tag{2.24}$$

$$\varepsilon \frac{\partial E_z}{\partial t} = \frac{\partial H_y}{\partial x} - \frac{\partial H_x}{\partial y} \tag{2.25}$$

Just like in the 2D case, a Cartesian grid of points is denoted as

$$(i_x, i_y, i_z) = (i_x\, \delta x, i_y\, \delta y, i_z\, \delta z) \tag{2.26}$$

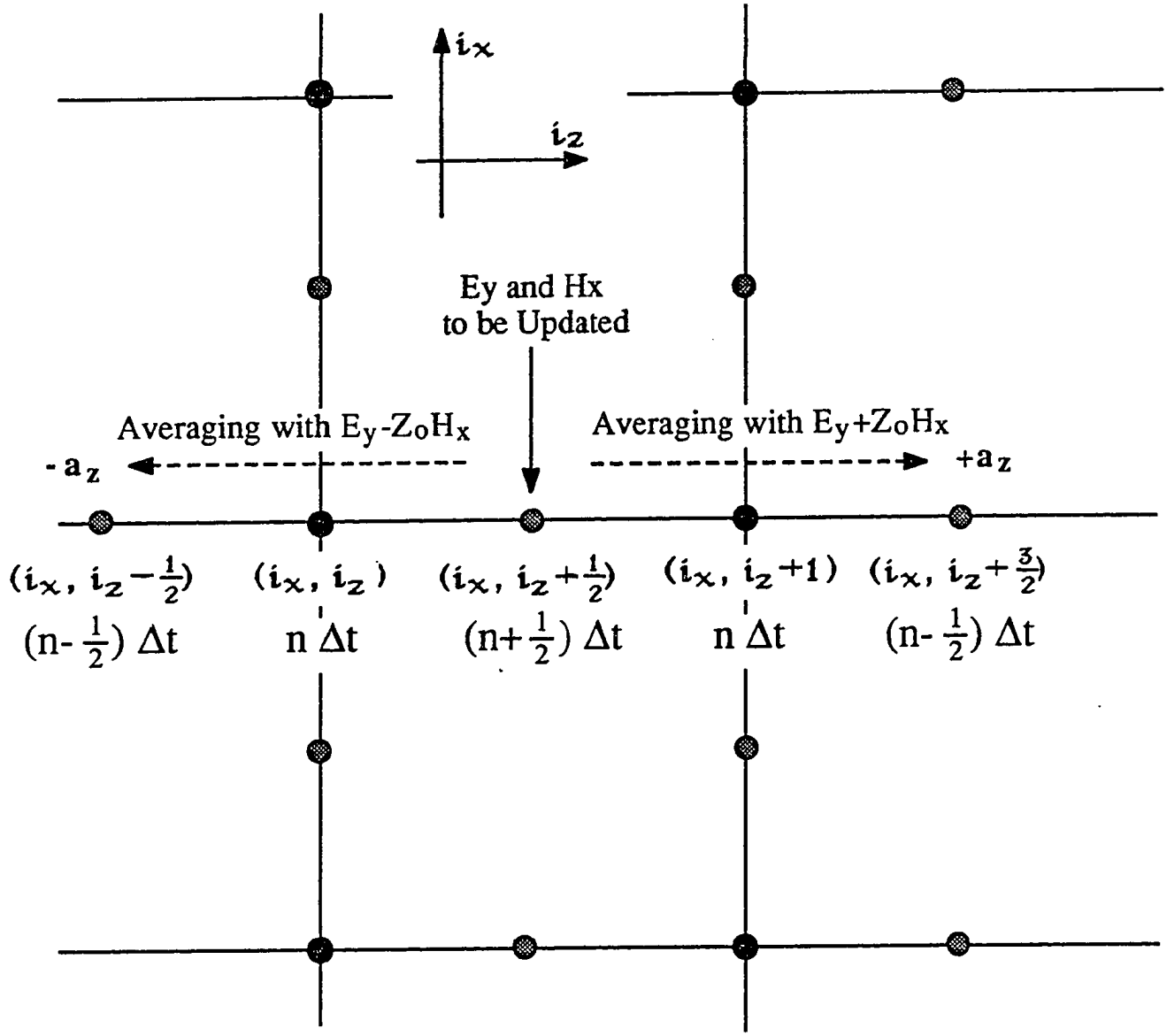

Figure 2.2: Averaging Process for the FD-TD Formulation

and any function of discrete space and time as

$$F(i_x\,\delta x, i_y\,\delta y, i_z\,\delta z, n\,\delta t) =_n F(i_x, i_y, i_z) \tag{2.27}$$

$\delta x = \delta y = \delta z = c_0\,\delta t$ are the space discretization units (taken to be the same for simplicity), δt is the time increment, ε and μ can be chosen as either $\varepsilon = \varepsilon_r\,\varepsilon_o$ and $\mu = \mu_r\,\mu_o$ or $\varepsilon = 2\varepsilon_r\,\varepsilon_o$ and $\mu = 2\mu_r\,\mu_o$ and i_x, i_y, i_z, n are integers.

In contrast to Yee's scheme [55] (see Fig.2.3), the six field components of **E** and **H** are defined at a node located at the center of the 3D cell , while at the points on the boundary surface of the 3D cell, only the field components tangential to the surface are considered (Fig.2.4). As in the 2D case, the **E**-field and H-field components are not separated in space, and both the tangential **E** and **H** field components are continuous across the interface of two adjacent cells.

By differencing 3D Maxwell's equation, (2.20) to (2.25), one can easily obtain a finite-difference formulation for Maxwell's equations.

For example, considering (2.23), one has

$$\varepsilon\frac{{}_{n+1}E_x(i_x,i_y,i_z) -_n E_x(i_x,i_y,i_z)}{\delta t} =$$
$$\frac{{}_{n+\frac{1}{2}}H_z(i_x,i_y+\frac{1}{2},i_z) -_{n+\frac{1}{2}} H_z(i_x,i_y-\frac{1}{2},i_z)}{\delta y} - \frac{{}_{n+\frac{1}{2}}H_y(i_x,i_y,i_z+\frac{1}{2}) -_{n+\frac{1}{2}} H_y(i_x,i_y,i_z-\frac{1}{2})}{\delta z} \tag{2.28}$$

Thus, ${}_{n+1}E_x(i_x,i_y,i_z)$ at the cell center can be updated from the values of **E** and **H**-field components at the previous time step.

The remaining finite difference equations corresponding to (2.20), (2.21), (2.22),(2.24) and (2.25) can be similarly constructed.

Again, in order to update both **E** and **H** on the boundary of a 3D cell, the averaging process over space and time is applied just as in the 2D situation. As a result, one has:

$$\begin{aligned} {}_nE_x(i_x,i_y,i_z) - Z_o\ {}_nH_z(i_x,i_y,i_z) = \\ \frac{1}{2}[{}_{n+\frac{1}{2}}E_x(i_x,i_y+\frac{1}{2},i_z) - Z_o\ {}_{n+\frac{1}{2}}H_z(i_x,i_y+\frac{1}{2},i_z) \\ +_{n-\frac{1}{2}}E_x(i_x,i_y-\frac{1}{2},i_z) - Z_o\ {}_{n-\frac{1}{2}}H_z(i_x,i_y-\frac{1}{2},i_z)] \end{aligned} \tag{2.29}$$

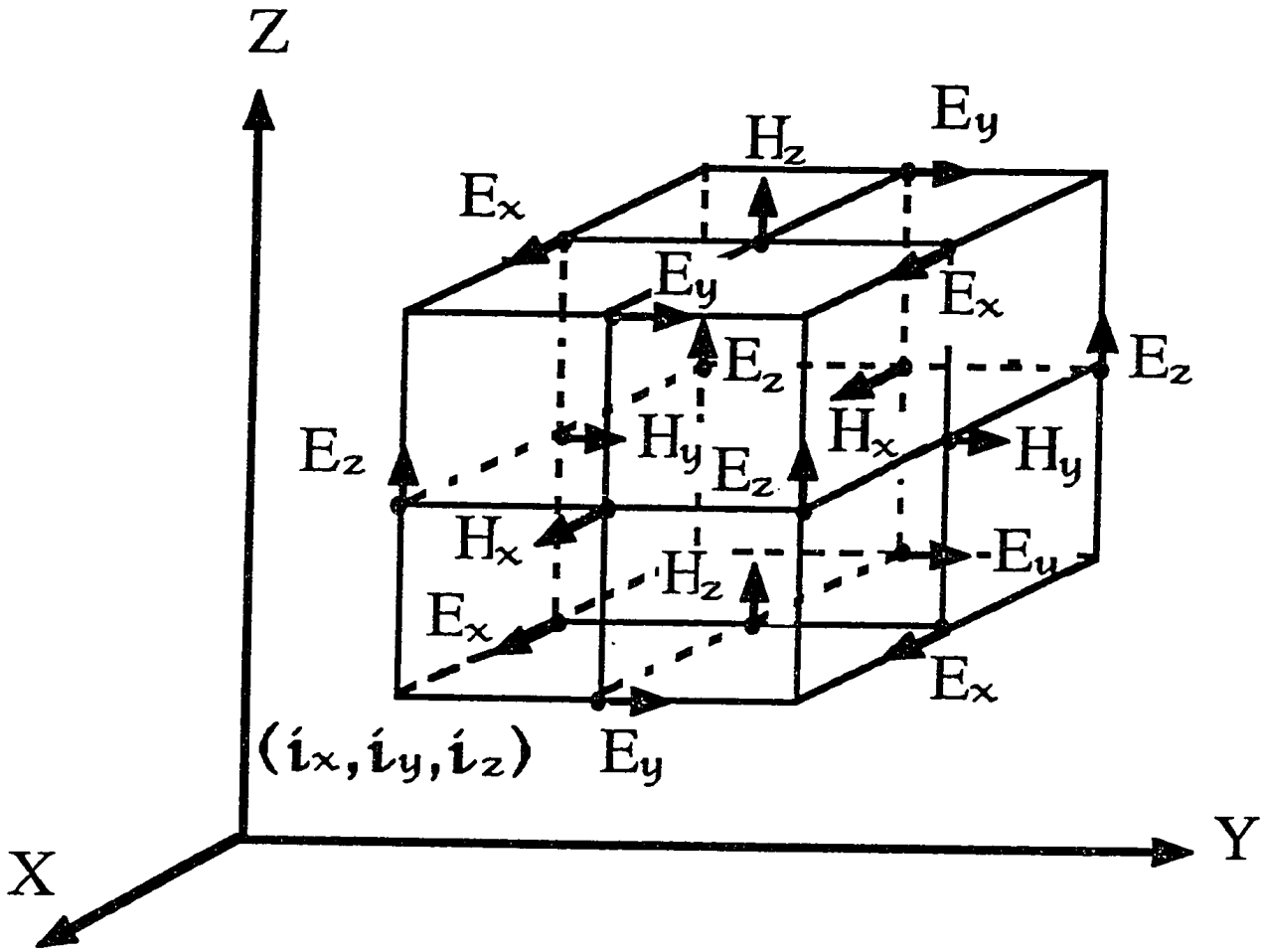

Figure 2.3: **Positions of the Field Components about a Unit Cell of the Yee Lattice**

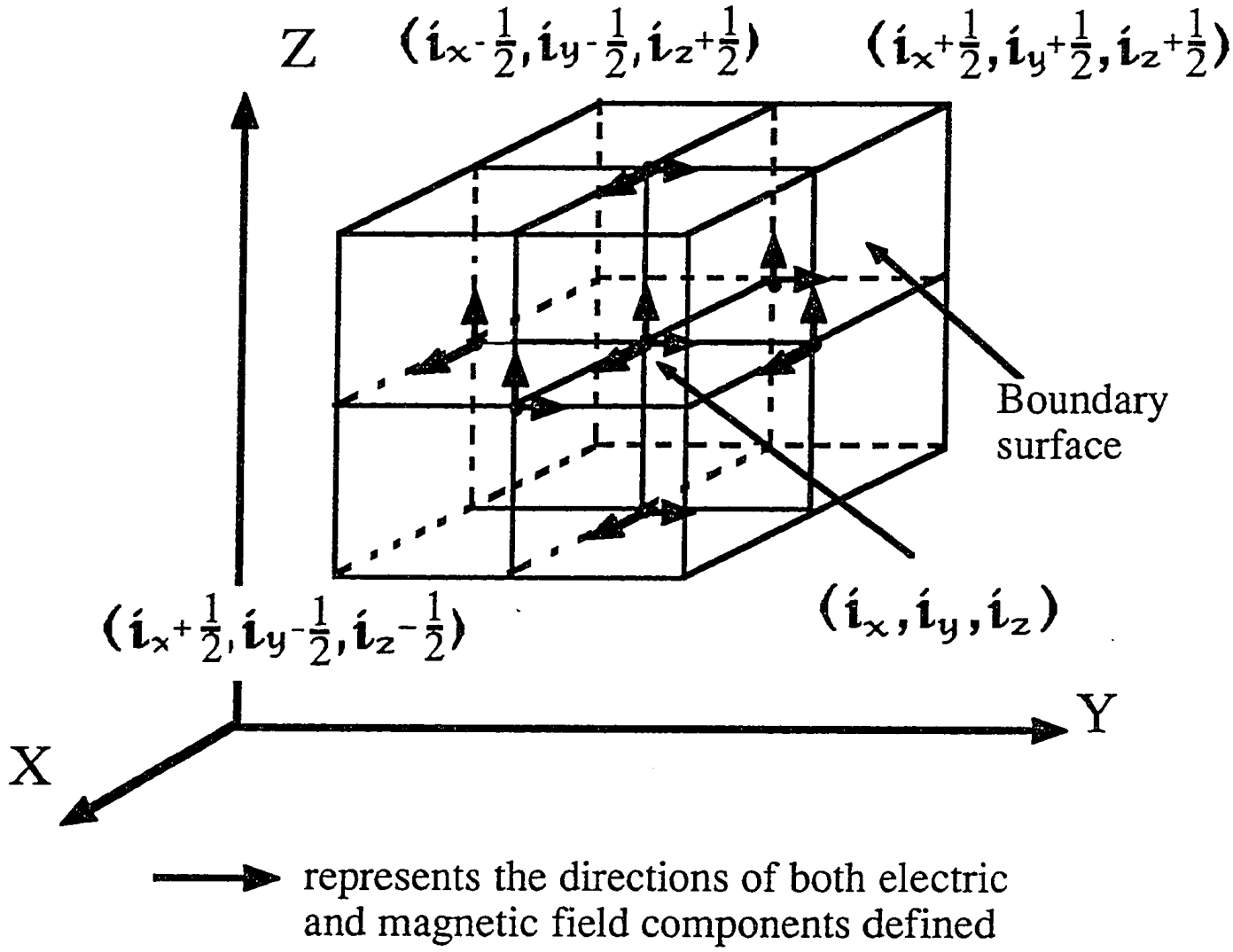

Figure 2.4: **Positions of the Field Components about a 3D Cell of the FD-TD Formulation**

$$
\begin{aligned}
&{}_nE_x(i_x, i_y+1, i_z) + Z_o\,{}_nH_z(i_x, i_y+1, i_z) = \\
&\quad \frac{1}{2}[{}_{n+\frac{1}{2}}E_x(i_x, i_y+\frac{1}{2}, i_z) + Z_o\ {}_{n+\frac{1}{2}}H_z(i_x, i_y+\frac{1}{2}, i_z) \\
&\quad +{}_{n-\frac{1}{2}}E_x(i_x, i_y+\frac{3}{2}, i_z) + Z_o\ {}_{n-\frac{1}{2}}H_z(i_x, i_y+\frac{3}{2}, i_z)] \qquad (2.30)
\end{aligned}
$$

From above, E_x and H_z on the boundary surface of the 3D cell can be obtained as follows:

$$
\begin{aligned}
&{}_{n+\frac{1}{2}}E_x(i_x, i_y+\frac{1}{2}, i_z) = \\
&\quad {}_nE_x(i_x, i_y, i_z) - Z_o\ {}_nH_z(i_x, i_y, i_z) +{}_n E_x(i_x, i_y+1, i_z) + Z_o\ {}_nH_z(i_x, i_y+1, i_z) \\
&\quad -\frac{1}{2}[{}_{n-\frac{1}{2}}E_x(i_x, i_y-\frac{1}{2}, i_z) - Z_o\ {}_{n-\frac{1}{2}}H_z(i_x, i_y-\frac{1}{2}, i_z) \\
&\quad +{}_{n-\frac{1}{2}}E_x(i_x, i_y+\frac{3}{2}, i_z) + Z_o\ {}_{n-\frac{1}{2}}H_z(i_x, i_y+\frac{3}{2}, i_z)] \qquad (2.31)
\end{aligned}
$$

$$
\begin{aligned}
&Z_o\ {}_{n+\frac{1}{2}}H_z(i_x, i_y+\frac{1}{2}, i_z) = \\
&\quad [-{}_nE_x(i_x, i_y, i_z) + Z_o\ {}_nH_z(i_x, i_y, i_z) +{}_n E_x(i_x, i_y+1, i_z) + Z_o\ {}_nH_z(i_x, i_y+1, i_z)] \\
&\quad -\frac{1}{2}[-{}_{n-\frac{1}{2}}E_x(i_x, i_y-\frac{1}{2}, i_z) + Z_o\ {}_{n-\frac{1}{2}}H_z(i_x, i_y-\frac{1}{2}, i_z) \\
&\quad +{}_{n-\frac{1}{2}}E_x(i_x, i_y+\frac{3}{2}, i_z) + Z_o\ {}_{n-\frac{1}{2}}H_z(i_x, i_y+\frac{3}{2}, i_z)] \qquad (2.32)
\end{aligned}
$$

where $Z_o = \sqrt{\frac{\mu}{\varepsilon}}$ if $\varepsilon = \varepsilon_r\,\varepsilon_o$ and $\mu = \mu_r\,\mu_o$ are chosen, or, $Z_o = \sqrt{\frac{\mu_0}{\varepsilon_0}}$ if $\varepsilon = 2\varepsilon_r\,\varepsilon_o$ and $\mu = 2\mu_r\,\mu_o$ are chosen. Again, it is recommended that $Z_o = \sqrt{\frac{\mu_0}{\varepsilon_0}}$ and $\varepsilon = 2\varepsilon_r\,\varepsilon_o$ and $\mu = 2\mu_r\,\mu_o$ be chosen (and henceforth applied in this thesis) since (2.29) to (2.32) would be independent of the medium permeability and permittivity. Note in this case, the FD-TD scheme virtually simulates a medium of relative permittivity $2\,\varepsilon_r$ and permeability $2\,\mu_r$ rather than ε_r and μ_r.

The equations pertaining to updated values of other tangential **E** and **H** field components on the other boundary surfaces of a 3D cell can be constructed in a similar way or can be obtained by simply permuting subscripts (x, y, z) and coordinates (i_x, i_y, i_z) in the above equations.

As one can see, equations (2.7) to (2.17) and (2.28) to (2.32) constitute a recursive finite-difference formulation for time-dependent Maxwell's equations based on a new grid arrangement and the averaging process. When boundaries are placed half-way between

two neighboring cells (ie. at the boundary surface of a 3D cell), the boundary conditions can be fulfilled by simply enforcing them in (2.10), (2.12) for two dimensions, or (2.29) for three dimensions. Generally speaking, this finite-difference formulation ensures the continuity of both tangential electric and magnetic field components across the interfaces of cubic cells. Therefore, the energy flowing in the whole network will be conserved and a stable non-dissipative solution will be generated. For a more general Finite-Difference Time-Domain formulations including loss and variable mesh size, see Appendix A.

2.3 Theory and Application of the TLM method

The Transmission-Line-Matrix method is a time-domain numerical technique for solving network and field problems. The theory of the method and its applications to electromagnetic problems have been well established [64] since its first formulation by P. B. Johns and his co-workers [3]. In principle, the electromagnetic problem is modeled by filling the field space with a network of interconnecting two-wire transmission lines (Fig.2.5). The voltage and current impulses at all intersection points, or nodes, are made equivalent to the electric and magnetic fields in the discretized space. Thus, the behavior of electromagnetic fields can be easily modeled quantitatively by the voltages and currents in the network of transmission lines or TLM models. Any inhomogeneity in the form of dielectric or magnetic materials can be accounted for by introducing further lengths of transmission lines as shunt or series stubs to the network. The numerical calculations start with exciting the network, or mesh, at specific points in terms of voltage or current impulses. Then, at each subsequent time step, these impulses propagate through the transmission lines connecting two neighbor nodes, scatter at the nodes and bounce back at the boundaries. The output, which is taken from a chosen node, consists of a series of impulses separated by a constant time interval. The Fourier transform of this output function can be performed and useful information about the frequency behavior of the structure extracted. The details of the TLM method and an extensive list of references on this subject can be found in [67].

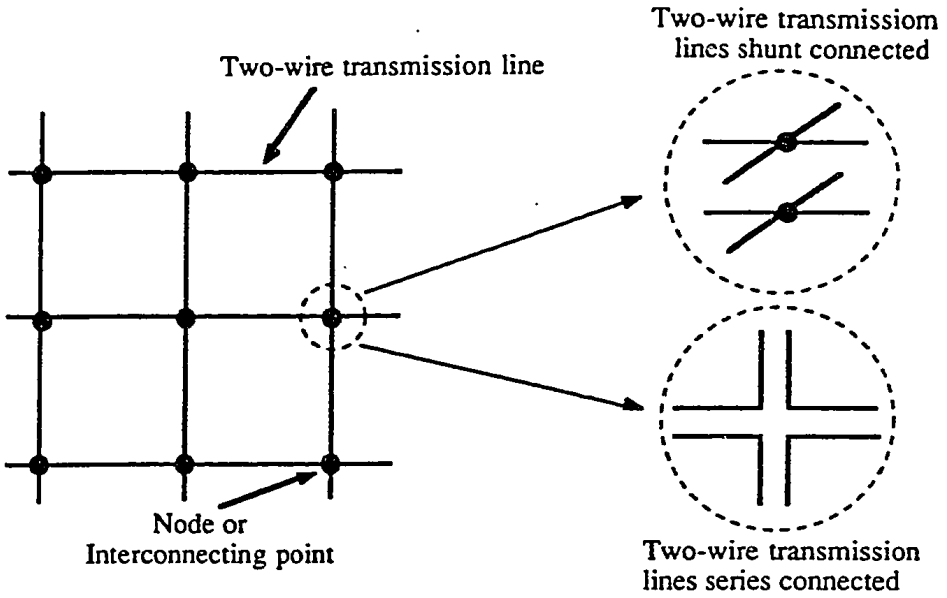

(a) A 2D TLM network (or matrix)

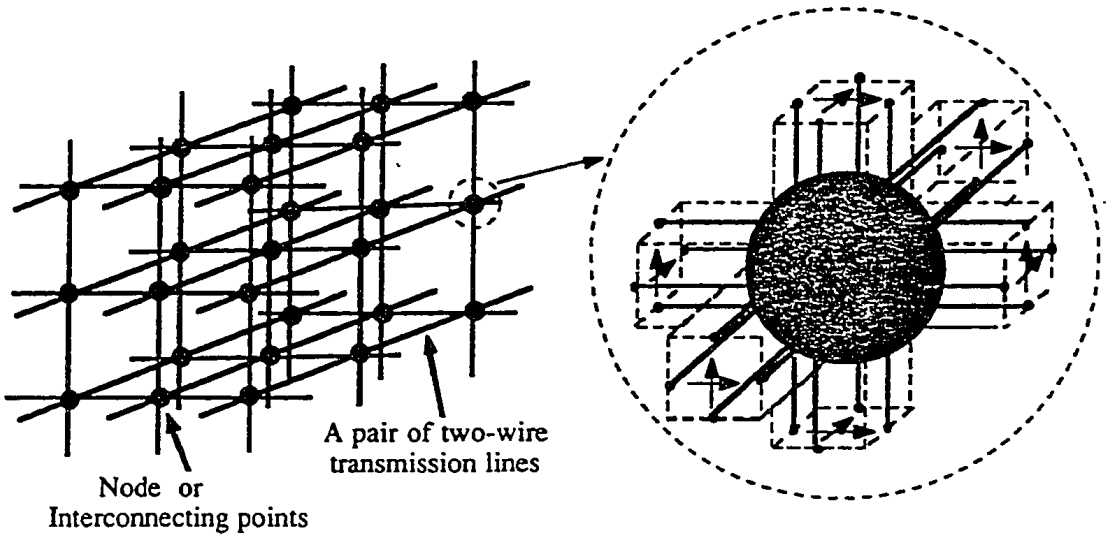

(b) A 3D TLM network (or matrix)

Figure 2.5: **A TLM Network**

2.4 Voltage and Current Relations in the TLM Symmetrical Condensed Node and Its Equivalence to the Finite-Difference Approach

Various types of nodes have been proposed for the TLM model. For 2D problems, the shunt node and the series node model [7] can be used, and for 3D problems, the expanded-node [9], the asymmetrical condensed node [10, 11] and the more recently developed symmetrical condensed node model [14] exist.

2.4.1 The 2D TLM node

Consider a 2D TLM shunt node model [3] without inductive, capacitive and loss stubs (Fig.2.6). For simplicity, suppose that each link line has the same length, $\Delta l/2$ (regular mesh), and that all the assumptions made by Johns are valid here. In addition, similarly to the denotation used in the FD-TD formulation, function of voltage $V(i_x\,\Delta l, i_z\,\Delta l, n\,\Delta t)$ is denoted as ${}_nV(i_x, i_z)$. Note that the total voltages and currents at mid points between two adjacent nodes are the sum or difference of the incident and reflected voltages on the link line, according to transmission line theory. For instance, if on link line 2, at time $(n+\frac{1}{2})\Delta t$ and position $(i_x, i_z-\frac{1}{2})$, ${}_{n+\frac{1}{2}}V_2^i(i_x, i_z-\frac{1}{2})$ is the voltage impulse going toward the node with position (i_x, i_z) and ${}_{n+\frac{1}{2}}V_2^r(i_x, i_z-\frac{1}{2})$ is the voltage impulse going away from the same node, then the total voltage at $(i_x, i_z-\frac{1}{2})$ is:

$$ {}_{n+\frac{1}{2}}V_y(i_x, i_z-\frac{1}{2}) = {}_{n+\frac{1}{2}}V_2^i(i_x, i_z-\frac{1}{2}) + {}_{n+\frac{1}{2}}V_2^r(i_x, i_z-\frac{1}{2}) \tag{2.33} $$

and the total current at position $(i_x, i_z-\frac{1}{2})$ flowing along the z direction (in link line 2) is,

$$ {}_{n+\frac{1}{2}}I_z(i_x, i_z-\frac{1}{2}) = [{}_{n+\frac{1}{2}}V_2^i(i_x, i_z-\frac{1}{2}) - {}_{n+\frac{1}{2}}V_2^r(i_x, i_z-\frac{1}{2})]/Z_0 \tag{2.34} $$

where Z_0 is the characteristic impedance of the link line.

Similar voltage and current definitions and relations with their corresponding equations can be derived on the other link lines at mid-points between the nodes. Together with the relations between voltages, currents at nodes and incidents impulses on link lines [67], it is not difficult to verify that the following relations exist in the 2D TLM shunt node (see Appendix B):

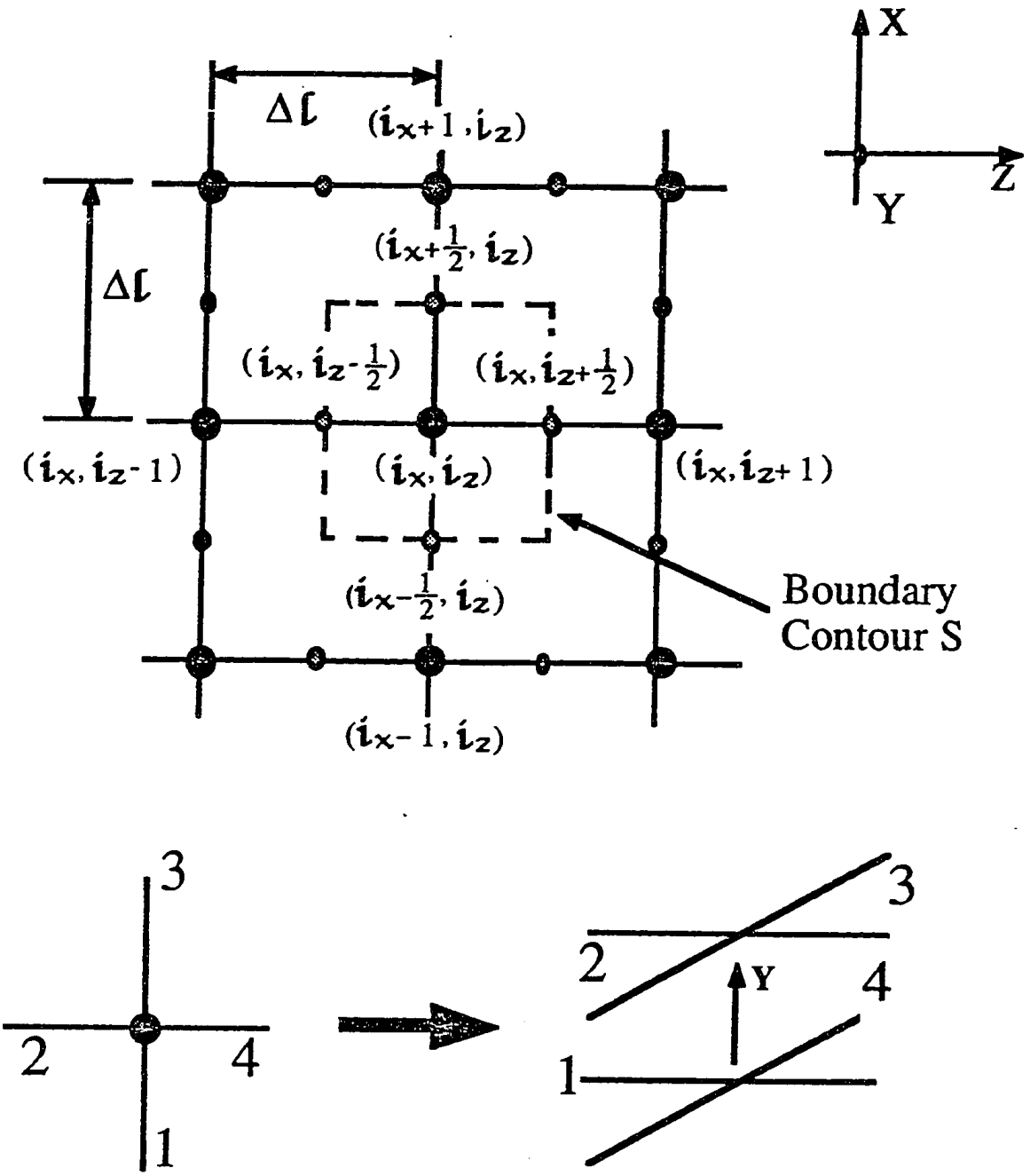

Figure 2.6: A Two-Dimensional TLM Shunt Node

$$-L\frac{^{n+1}I_x(i_x,i_z) -_n I_x(i_x,i_z)}{\Delta t} = \frac{^{n+\frac{1}{2}}V_y(i_x+\frac{1}{2},i_z) -_{n+\frac{1}{2}} V_y(i_x-\frac{1}{2},i_z)}{\Delta l} \tag{2.35}$$

$$-L\frac{^{n+1}I_z(i_x,i_z) -_n I_z(i_x,i_z)}{\Delta t} = \frac{^{n+\frac{1}{2}}V_y(i_x,i_z+\frac{1}{2}) -_{n+\frac{1}{2}} V_y(i_x,i_z-\frac{1}{2})}{\Delta l} \tag{2.36}$$

$$2\,C\frac{^{n+1}V_y(i_x,i_z) -_n V_y(i_x,i_z)}{\Delta t} = - \frac{^{n+\frac{1}{2}}I_z(i_x,i_z+\frac{1}{2}) -_{n+\frac{1}{2}} I_z(i_x,i_z-\frac{1}{2})}{\Delta l} - \frac{^{n+\frac{1}{2}}I_x(i_x+\frac{1}{2},i_z) -_{n+\frac{1}{2}} I_x(i_x-\frac{1}{2},i_z)}{\Delta l} \tag{2.37}$$

and

$$_nV_y(i_x,i_z) + Z_o\ {}_nI_z(i_x,i_z) = \frac{[_{n+\frac{1}{2}}V_y(i_x,i_z+\frac{1}{2}) + Z_o\ {}_{n+\frac{1}{2}}I_z(i_x,i_z+\frac{1}{2})] + [_{n-\frac{1}{2}}V_y(i_x,i_z-\frac{1}{2}) + Z_o\ {}_{n-\frac{1}{2}}I_z(i_x,i_z-\frac{1}{2}]}{2} \tag{2.38}$$

$$_nV_y(i_x,i_z+1) - Z_o\ {}_nI_z(i_x,i_z+1) = \frac{[_{n+\frac{1}{2}}V_y(i_x,i_z+\frac{1}{2}) - Z_o\ {}_{n+\frac{1}{2}}I_z(i_x,i_z+\frac{1}{2})] + [_{n-\frac{1}{2}}V_y(i_x,i_z+\frac{3}{2}) - Z_o\ {}_{n-\frac{1}{2}}I_z(i_x,i_z+\frac{3}{2})]}{2} \tag{2.39}$$

$$_nV_y(i_x,i_z) + Z_o\ {}_nI_x(i_x,i_z) = \frac{[_{n+\frac{1}{2}}V_y(i_x+\frac{1}{2},i_z) + Z_o\ {}_{n+\frac{1}{2}}I_x(i_x+\frac{1}{2},i_z)] + [_{n-\frac{1}{2}}V_y(i_x-\frac{1}{2},i_z) + Z_o\ {}_{n-\frac{1}{2}}I_x(i_x-\frac{1}{2},i_z)]}{2} \tag{2.40}$$

$$_nV_y(i_x+1,i_z) - Z_o\ {}_nI_x(i_x+1,i_z) = \frac{[_{n+\frac{1}{2}}V_y(i_x+\frac{1}{2},i_z) - Z_o\ {}_{n+\frac{1}{2}}I_x(i_x+\frac{1}{2},i_z)] + [_{n-\frac{1}{2}}V_y(i_x+\frac{3}{2},i_z) - Z_o\ {}_{n-\frac{1}{2}}I_x(i_x+\frac{3}{2},i_z)]}{2} \tag{2.41}$$

or,

$$
\begin{aligned}
&{}_{n+\frac{1}{2}}V_y(i_x, i_z+\frac{1}{2}) = \\
&\quad {}_nV_y(i_x,i_z) + Z_o\ {}_nI_z(i_x,i_z) + {}_nV_y(i_x,i_z+1) - Z_o\ {}_nI_z(i_x,i_z+1) \\
&\quad -\frac{1}{2}[{}_{n-\frac{1}{2}}V_y(i_x,i_z-\frac{1}{2}) + Z_o\ {}_{n-\frac{1}{2}}I_z(i_x,i_z-\frac{1}{2}) \\
&\quad +{}_{n-\frac{1}{2}}V_y(i_x,i_z+\frac{3}{2}) - Z_o\ {}_{n-\frac{1}{2}}I_z(i_x,i_z+\frac{3}{2})]
\end{aligned} \tag{2.42}
$$

$$
\begin{aligned}
&-Z_o\ {}_{n+\frac{1}{2}}I_z(i_x, i_z+\frac{1}{2}) = \\
&\quad [-{}_nV_y(i_x,i_z) - Z_o\ {}_nI_z(i_x,i_z) + {}_nV_y(i_x,i_z+1) - Z_o\ {}_nI_z(i_x,i_z+1)] \\
&\quad -\frac{1}{2}[-{}_{n-\frac{1}{2}}V_y(i_x,i_z-\frac{1}{2}) - Z_o\ {}_{n-\frac{1}{2}}I_z(i_x,i_z-\frac{1}{2}) \\
&\quad +{}_{n-\frac{1}{2}}V_y(i_x,i_z+\frac{3}{2}) - Z_o\ {}_{n-\frac{1}{2}}I_z(i_x,i_z+\frac{3}{2})]
\end{aligned} \tag{2.43}
$$

$$
\begin{aligned}
&{}_{n+\frac{1}{2}}V_y(i_x+\frac{1}{2}, i_z) = \\
&\quad {}_nV_y(i_x,i_z) + Z_o\ {}_nI_x(i_x,i_z) + {}_nV_y(i_x+1,i_z) - Z_o\ {}_nI_x(i_x+1,i_z) \\
&\quad -\frac{1}{2}[{}_{n-\frac{1}{2}}V_y(i_x-\frac{1}{2},i_z) + Z_o\ {}_{n-\frac{1}{2}}I_x(i_x-\frac{1}{2},i_z) \\
&\quad +{}_{n-\frac{1}{2}}V_y(i_x+\frac{3}{2},i_z) - Z_o\ {}_{n-\frac{1}{2}}I_x(i_x+\frac{3}{2},i_z)]
\end{aligned} \tag{2.44}
$$

$$
\begin{aligned}
&Z_o\ {}_{n+\frac{1}{2}}I_x(i_x+\frac{1}{2}, i_z) = \\
&\quad [{}_nV_y(i_x,i_z) + Z_o\ {}_nI_x(i_x,i_z) - {}_nV_y(i_x+1,i_z) + Z_o\ {}_nI_x(i_x+1,i_z)] \\
&\quad -\frac{1}{2}[{}_{n-\frac{1}{2}}V_y(i_x-\frac{1}{2},i_z) + Z_o\ {}_{n-\frac{1}{2}}I_x(i_x-\frac{1}{2},i_z) \\
&\quad -{}_{n-\frac{1}{2}}V_y(i_x+\frac{3}{2},i_z) + Z_o\ {}_{n-\frac{1}{2}}I_x(i_x+\frac{3}{2},i_z)]
\end{aligned} \tag{2.45}
$$

where $Z_o = \sqrt{\frac{L}{C}}$, $\frac{\Delta l}{\Delta t} = \frac{1}{\sqrt{LC}}$, L is the inductance per unit length of the link line and C is the capacitance per unit length of the link line. Note that in fact, (2.38) to (2.41) can be considered as the result of an averaging process over time and space for the voltages and currents in the TLM model.

Assume that at any time and grid point, one has the following correspondences:

$$V_y \equiv E_y, \tag{2.46}$$

$$I_x \equiv H_z, \tag{2.47}$$

$$I_z \equiv -H_x, \tag{2.48}$$

$$2\,C \equiv \varepsilon, \tag{2.49}$$

$$L \equiv \mu, \tag{2.50}$$

$$\Delta l = \delta x = \delta z = \delta \tag{2.51}$$

$$\Delta t = \delta t \tag{2.52}$$

Then, (2.35) to (2.45), which were derived from the 2D TLM shunt node formulation, are exactly the same as (2.7) to (2.17) pertaining to the new FD-TD scheme for the two-dimensional case. That is, the 2D TLM shunt node model is equivalent to the FD-TD formulation.

In the case of a series node model, or if stubs are added for simulation of materials, it is not difficult to prove, by following a similar procedure, that the same conclusions can be drawn.

It should be pointed out here that the achievement of the equivalence between the 2D TLM nodes and the FD-TD approach is attributed to the introduction of the total voltage and current definitions as represented by (2.33) and (2.34).

2.4.2 The 3D TLM symmetrical condensed node

Consider a symmetrical condensed node without inductive, capacitive and loss stubs [14]. Each link line has the same length, $\Delta l/2$ (regular mesh) (Fig.2.7). Also, denote $V(i_x\Delta l, i_y\Delta l, i_z\Delta l, n\Delta t)$ as ${}_nV(i_x, i_y, i_z)$. Then, similar to the 2D case, the total voltages and currents at mid points between two adjacent nodes are expressed as the sum or difference of the incident and reflected voltages on the link line. For instance, the total voltage at $(i_x, i_y - \frac{1}{2}, i_z)$ on link line 1 is:

$${}_{n+\frac{1}{2}}V_{x1}(i_x, i_y - \frac{1}{2}, i_z) = {}_{n+\frac{1}{2}}V_1^i(i_x, i_y - \frac{1}{2}, i_z) + {}_{n+\frac{1}{2}}V_1^r(i_x, i_y - \frac{1}{2}, i_z) \tag{2.53}$$

and the total current at position $(i_x, i_y - \frac{1}{2}, i_z)$ flowing along the y direction (in link line 1) is

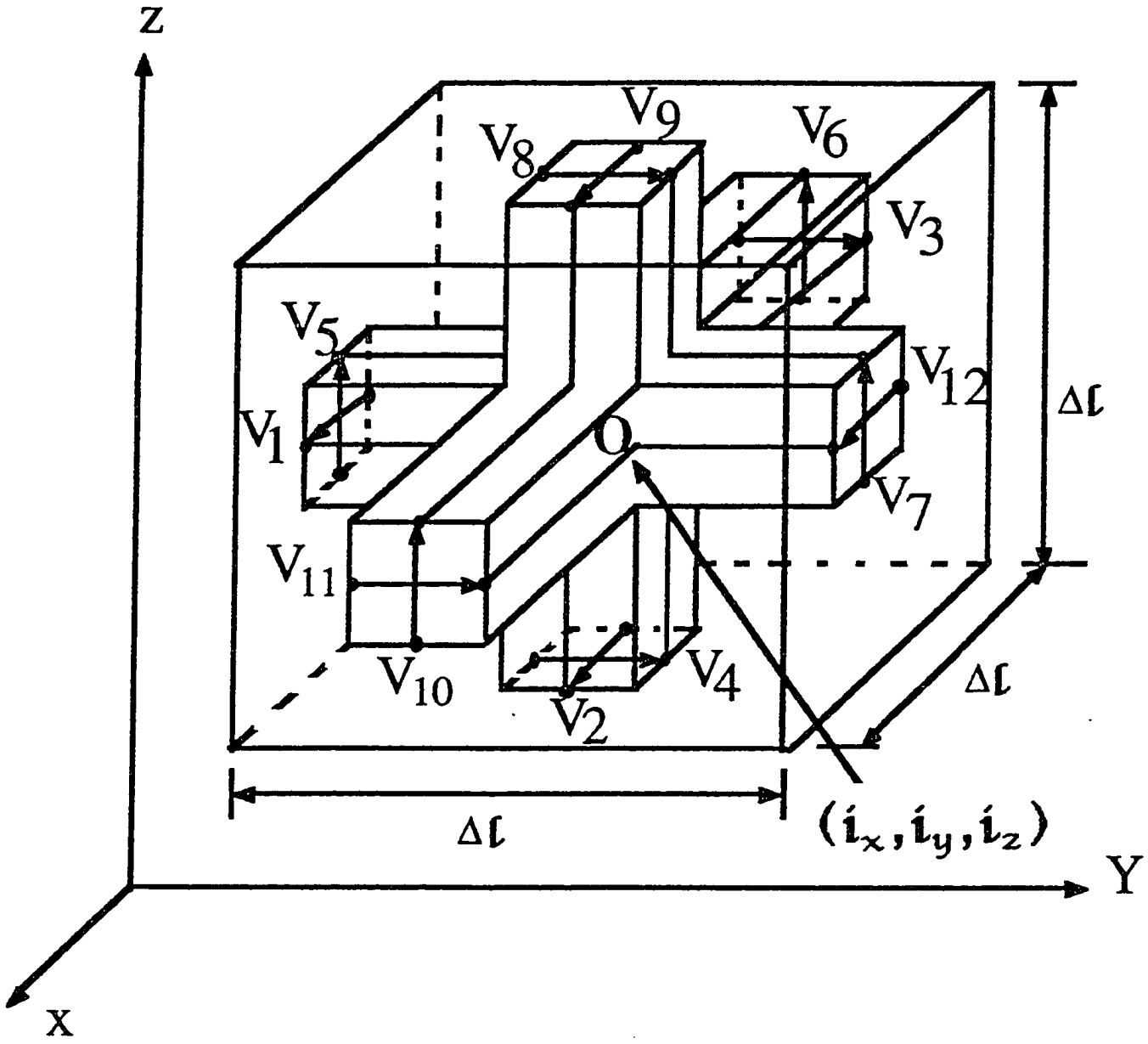

Figure 2.7: A Three-Dimensional Symmetrical Condensed Node

$$ {}_{n+\frac{1}{2}}I_{y1}(i_x, i_y - \frac{1}{2}, i_z) = [{}_{n+\frac{1}{2}}V_1^i(i_x, i_y - \frac{1}{2}, i_z) - {}_{n+\frac{1}{2}}V_1^r(i_x, i_y - \frac{1}{2}, i_z)]/Z_0 \tag{2.54} $$

where Z_0 is the characteristic impedance of the link line.

Again, with $Z_O = \sqrt{\frac{L}{C}}$ and $\frac{\Delta l}{\Delta t} = \frac{1}{\sqrt{LC}}$, one can easily verify the following relations (see Appendix C):

$$ \begin{aligned} 2\,C\frac{{}^{n+1}V_x(i_x, i_y, i_z) - {}_n\,V_x(i_x, i_y, i_z)}{\Delta t} = \\ - \frac{{}_{n+\frac{1}{2}}I_{y12}(i_x, i_y + \frac{1}{2}, i_z) - {}_{n+\frac{1}{2}}\,I_{y1}(i_x, i_y - \frac{1}{2}, i_z)}{\Delta l} \\ - \frac{{}_{n+\frac{1}{2}}I_{z9}(i_x, i_y, i_z + \frac{1}{2}) - {}_{n+\frac{1}{2}}\,I_{z2}(i_x, i_y, i_z - \frac{1}{2})}{\Delta l} \end{aligned} \tag{2.55} $$

and

$$ \begin{aligned} {}_nV_x(i_x, i_y, i_z) + Z_o\ {}_nI_{xy}(i_x, i_y, i_z) = \\ \frac{1}{2}[{}_{n+\frac{1}{2}}V_{x12}(i_x, i_y + \frac{1}{2}, i_z) + Z_o\ {}_{n+\frac{1}{2}}I_{y12}(i_x, i_y + \frac{1}{2}, i_z) + \\ {}_{n-\frac{1}{2}}V_{x1}(i_x, i_y - \frac{1}{2}, i_z) + Z_o\ {}_{n-\frac{1}{2}}I_{y1}(i_x, i_y - \frac{1}{2}, i_z)] \end{aligned} \tag{2.56} $$

$$ \begin{aligned} {}_nV_x(i_x, i_y + 1, i_z) - Z_o\ {}_nI_{xy}(i_x, i_y + 1, i_z) = \\ \frac{1}{2}[{}_{n+\frac{1}{2}}V_{x12}(i_x, i_y + \frac{1}{2}, i_z) - Z_o\ {}_{n+\frac{1}{2}}I_{y12}(i_x, i_y + \frac{1}{2}, i_z) + \\ {}_{n-\frac{1}{2}}V_{x12}(i_x, i_y + \frac{3}{2}, i_z) - Z_o\ {}_{n-\frac{1}{2}}I_{y12}(i_x, i_y + \frac{3}{2}, i_z)] \end{aligned} \tag{2.57} $$

or,

$$ \begin{aligned} {}_{n+\frac{1}{2}}V_{x12}(i_x, i_y + \frac{1}{2}, i_z) = \\ {}_nV_x(i_x, i_y, i_z) + Z_o\ {}_nI_{xy}(i_x, i_y, i_z) + {}_n\,V_x(i_x, i_y + 1, i_z) - Z_o\ {}_nI_{xy}(i_x, i_y + 1, i_z) \\ -\frac{1}{2}[{}_{n-\frac{1}{2}}V_{x1}(i_x, i_y - \frac{1}{2}, i_z) + Z_o\ {}_{n-\frac{1}{2}}I_{y1}(i_x, i_y - \frac{1}{2}, i_z) \\ +{}_{n-\frac{1}{2}}V_{x12}(i_x, i_y + \frac{3}{2}, i_z) - Z_o\ {}_{n-\frac{1}{2}}I_{y12}(i_x, i_y + \frac{3}{2}, i_z)] \end{aligned} \tag{2.58} $$

$$
\begin{aligned}
&-Z_o\ {}_{n+\frac{1}{2}}I_{y12}(i_x, i_y+\frac{1}{2}, i_z) = \\
&\quad -{}_nV_x(i_x, i_y, i_z) - Z_o\ {}_nI_{xy}(i_x, i_y, i_z) + {}_n\,V_x(i_x, i_y+1, i_z) - Z_o\ {}_nI_{xy}(i_x, i_y+1, i_z) \\
&\quad -\frac{1}{2}[-{}_{n-\frac{1}{2}}V_{x1}(i_x, i_y-\frac{1}{2}, i_z) - Z_o\ {}_{n-\frac{1}{2}}I_{y1}(i_x, i_y-\frac{1}{2}, i_z) \\
&\quad +{}_{n-\frac{1}{2}}V_{x12}(i_x, i_y+\frac{3}{2}, i_z) - Z_o\ {}_{n-\frac{1}{2}}I_{y12}(i_x, i_y+\frac{3}{2}, i_z)] \qquad (2.59)
\end{aligned}
$$

If one assumes that voltages and currents defined above are associated with the appropriate field components as indicated in [14]:

$$
\begin{aligned}
V_x &\equiv E_x \quad at\ (i_x, i_y, i_z)\ and\ (i_x, i_y \pm \frac{1}{2}, i_z) && (2.60)\\
I_{xy} &\equiv H_z \quad at\ (i_x, i_y, i_z) && (2.61)\\
I_z &\equiv H_y \quad at\ (i_x, i_y, i_z \pm \frac{1}{2}) && (2.62)\\
-I_y &\equiv H_z \quad at\ (i_x, i_y \pm \frac{1}{2}, i_z) && (2.63)\\
2\,C &\equiv \varepsilon && (2.64)\\
\Delta l &= \delta x = \delta z = \delta && (2.65)\\
\Delta t &= \delta t && (2.66)
\end{aligned}
$$

at any time step, then (2.55) to (2.59) are exactly the same as (2.28) to (2.32), one of the new finite-difference formulae for Maxwell's equations.

The remaining equations can be derived in a similar manner by assuming $V_y \equiv E_y$, $V_z \equiv E_z$, $\mu \equiv 2L$ and permutation of subscripts (x, y, z) and coordinates (i_x, i_y, i_z) in (2.60) to (2.63) for current and H-field components (L and C are the inductance and capacitance per unit length of the link lines, respectively). Thus, it has been shown that the 3D symmetrical condensed node TLM model is numerically equivalent to the finite-difference equations for Maxwell's equations. One can easily verify that the same conclusion will be reached by following a similar procedure for a condensed node with stubs, including loss stubs. Again, the achievement of the equivalence is very much attributed to the introduction of the total voltage and current definitions as represented by (2.53) and (2.54).

So far it has been shown that the 2D TLM node and the 3D symmetrical condensed TLM node are each numerically equivalent to a finite-difference formulation. On the other hand, the 3D expanded node TLM model was shown to be correspondent to Yee's finite-difference method [61, 62, 63]. For the 3D asymmetrical condensed node model, the equivalent FD-TD scheme can be found in a similar way since the 3D asymmetrical condensed node is a reduction of the 3D expanded node model. As a result, the equivalence between TLM and FD-TD formulations is now fully demonstrated in general . This suggests that any TLM algorithm can be formulated exactly in a finite-difference form and vice versa.

2.5 Conversion of the TLM Solutions

2.5.1 Conversion of the standard TLM solutions

Two-dimensional case Consider the 2D shunt node model in Fig.2.6 (which is most used for the 2D problems). Usually, $L \equiv \mu$ and $C \equiv \varepsilon_0 \varepsilon_r$ (ε_r is the relative permittivity of the medium to be modeled) are chosen for TLM simulations. According to (2.46) to (2.52) and (2.7) to (2.9), the equivalent FD-TD formulations associated with the permittivity would be:

$$-\mu \frac{{}^{n+1}H_z(i_x, i_z) - {}_n H_z(i_x, i_z)}{\delta t} = \frac{{}^{n+\frac{1}{2}}E_y(i_x + \frac{1}{2}, i_z) - {}_{n+\frac{1}{2}} E_y(i_x - \frac{1}{2}, i_z)}{\delta x} \tag{2.67}$$

$$\mu \frac{{}^{n+1}H_x(i_x, i_z) - {}_n H_x(i_x, i_z)}{\delta t} = \frac{{}^{n+\frac{1}{2}}E_y(i_x, i_z + \frac{1}{2}) - {}_{n+\frac{1}{2}} E_y(i_x, i_z - \frac{1}{2})}{\delta z} \tag{2.68}$$

$$2\varepsilon_r\varepsilon_0 \frac{{}^{n+1}E_y(i_x, i_z) - {}_n E_y(i_x, i_z)}{\delta t} = \frac{{}^{n+\frac{1}{2}}H_x(i_x, i_z + \frac{1}{2}) - {}_{n+\frac{1}{2}} H_x(i_x, i_z - \frac{1}{2})}{\delta z} - \frac{{}^{n+\frac{1}{2}}H_z(i_x + \frac{1}{2}, i_z) - {}_{n+\frac{1}{2}} H_z(i_x - \frac{1}{2}, i_z)}{\delta x} \tag{2.69}$$

with $\delta x = \delta z = \Delta l$. Note (2.10) to (2.17) are independent of permittivity as indicated before.

It can be seen that the 2D TLM shunt node is virtually simulating the medium of $2\varepsilon_r$ instead of the actual medium of ε_r. Therefore, the TLM solutions need to be converted to those with the actual medium of ε_r.

In fact, (2.67) to (2.69) can be rewritten as:

$$-\mu\frac{{}^{n+1}H_z(i_x,i_z)-{}_nH_z(i_x,i_z)}{\frac{\delta t}{\sqrt{2}}}=\frac{\sqrt{2}\,{}_{n+\frac{1}{2}}E_y(i_x+\frac{1}{2},i_z)-\sqrt{2}\,{}_{n+\frac{1}{2}}E_y(i_x-\frac{1}{2},i_z)}{\delta x} \tag{2.70}$$

$$\mu\frac{{}^{n+1}H_x(i_x,i_z)-{}_nH_x(i_x,i_z)}{\frac{\delta t}{\sqrt{2}}}=\frac{\sqrt{2}\,{}_{n+\frac{1}{2}}E_y(i_x,i_z+\frac{1}{2})-\sqrt{2}\,{}_{n+\frac{1}{2}}E_y(i_x,i_z-\frac{1}{2})}{\delta z} \tag{2.71}$$

$$\begin{aligned}&\varepsilon_r\varepsilon_0\frac{\sqrt{2}\,{}_{n+1}E_y(i_x,i_z)-\sqrt{2}\,{}_nE_y(i_x,i_z)}{\frac{\delta t}{\sqrt{2}}}\\&\quad=\frac{{}^{n+\frac{1}{2}}H_x(i_x,i_z+\frac{1}{2})-{}_{n+\frac{1}{2}}H_x(i_x,i_z-\frac{1}{2})}{\delta z}-\frac{{}^{n+\frac{1}{2}}H_z(i_x+\frac{1}{2},i_z)-{}_{n+\frac{1}{2}}H_z(i_x-\frac{1}{2},i_z)}{\delta x}\end{aligned} \tag{2.72}$$

On the other hand, the 2D Maxwell's equations for medium of ε_r can be expressed in difference form as follows:

$$-\mu\frac{{}^{n+1}H_z(i_x,i_z)-{}_nH_z(i_x,i_z)}{\delta t}=\frac{{}^{n+\frac{1}{2}}E_y(i_x+\frac{1}{2},i_z)-{}_{n+\frac{1}{2}}E_y(i_x-\frac{1}{2},i_z)}{\delta x} \tag{2.73}$$

$$\mu\frac{{}^{n+1}H_x(i_x,i_z)-{}_nH_x(i_x,i_z)}{\delta t}=\frac{{}^{n+\frac{1}{2}}E_y(i_x,i_z+\frac{1}{2})-{}_{n+\frac{1}{2}}E_y(i_x,i_z-\frac{1}{2})}{\delta z} \tag{2.74}$$

$$\begin{aligned}&\varepsilon_r\varepsilon_0\frac{{}^{n+1}E_y(i_x,i_z)-{}_nE_y(i_x,i_z)}{\delta t}\\&\quad=\frac{{}^{n+\frac{1}{2}}H_x(i_x,i_z+\frac{1}{2})-{}_{n+\frac{1}{2}}H_x(i_x,i_z-\frac{1}{2})}{\delta z}-\frac{{}^{n+\frac{1}{2}}H_z(i_x+\frac{1}{2},i_z)-{}_{n+\frac{1}{2}}H_z(i_x-\frac{1}{2},i_z)}{\delta x}\end{aligned} \tag{2.75}$$

Consequently, by comparing the above equations with (2.70)-(2.72), one can easily obtain the solutions for the medium of ε_r from the correspondent TLM solutions in the following way:

$$\mathbf{E}\ of\ actual\ medium = \sqrt{2}\,(\mathbf{E}\ of\ TLM\ solutions) \tag{2.76}$$

$$\mathbf{H}\ of\ actual\ medium = \mathbf{H}\ of\ TLM\ solutions \tag{2.77}$$

$$\delta t\ of\ actual\ medium = (\Delta i\ of\ TLM\ solutions)/\sqrt{2} \tag{2.78}$$

$$\sigma\ of\ actual\ medium = (\sigma\ of\ TLM\ solutions)/\sqrt{2}\ \ (if\ applicable) \tag{2.79}$$

For the 2D TLM series node, a similar conclusion can be obtained.

Three-dimensional case Still consider the 3D TLM symmetrical condensed node as shown in Fig.2.7. Usually, $L \equiv \mu_0\,\mu_r$ and $C \equiv \varepsilon_0\,\varepsilon_r$ are chosen (μ_r and ε_r are the relative permeability and permittivity of the medium to be modeled). Then, according to (2.60) to (2.66) and (2.28), one of the equivalent FD-TD formulations associated of μ_r and ε_r would be:

$$2\varepsilon_0\varepsilon_r \frac{{}^{n+1}E_x(i_x,i_y,i_z) - {}_nE_x(i_x,i_y,i_z)}{\delta t} = \frac{{}^{n+\frac{1}{2}}H_z(i_x,i_y+\frac{1}{2},i_z) - {}_{n+\frac{1}{2}}H_z(i_x,i_y-\frac{1}{2},i_z)}{\delta y} - \frac{{}^{n+\frac{1}{2}}H_y(i_x,i_y,i_z+\frac{1}{2}) - {}_{n+\frac{1}{2}}H_y(i_x,i_y,i_z-\frac{1}{2})}{\delta z} \tag{2.80}$$

with $\delta x = \delta y = \delta z = \Delta l$. Note (2.29) to (2.30) are independent of μ_r and ε_r as indicated before.

It is not difficult to derive the other equivalent accompanying FD-TD equations as described in Section 2.3.2.

For example, one may obtain:

$$-2\mu_0\mu_r \frac{{}^{n+1}H_x(i_x,i_y,i_z) - {}_nH_x(i_x,i_y,i_z)}{\delta t} = \frac{{}^{n+\frac{1}{2}}E_z(i_x,i_y+\frac{1}{2},i_z) - {}_{n+\frac{1}{2}}E_z(i_x,i_y-\frac{1}{2},i_z)}{\delta y} - \frac{{}^{n+\frac{1}{2}}E_y(i_x,i_y,i_z+\frac{1}{2}) - {}_{n+\frac{1}{2}}E_y(i_x,i_y,i_z-\frac{1}{2})}{\delta z} \tag{2.81}$$

The above two equations can be rewritten as:

$$\varepsilon_0\varepsilon_r \frac{{}^{n+1}E_x(i_x,i_y,i_z) - {}_nE_x(i_x,i_y,i_z)}{\frac{\delta t}{2}} = \frac{{}^{n+\frac{1}{2}}H_z(i_x,i_y+\frac{1}{2},i_z) - {}_{n+\frac{1}{2}}H_z(i_x,i_y-\frac{1}{2},i_z)}{\delta y} - \frac{{}^{n+\frac{1}{2}}H_y(i_x,i_y,i_z+\frac{1}{2}) - {}_{n+\frac{1}{2}}H_y(i_x,i_y,i_z-\frac{1}{2})}{\delta z} \tag{2.82}$$

and

$$-\mu_0\mu_r \frac{{}_{n+1}H_x(i_x,i_y,i_z) - {}_nH_x(i_x,i_y,i_z)}{\frac{\delta t}{2}} =$$
$$\frac{{}_{n+\frac{1}{2}}E_z(i_x,i_y+\frac{1}{2},i_z) - {}_{n+\frac{1}{2}}E_z(i_x,i_y-\frac{1}{2},i_z)}{\delta y}$$
$$- \frac{{}_{n+\frac{1}{2}}E_y(i_x,i_y,i_z+\frac{1}{2}) - {}_{n+\frac{1}{2}}E_y(i_x,i_y,i_z-\frac{1}{2})}{\delta z} \tag{2.83}$$

By comparing these two equations with Maxwell's equations in difference form for the actual medium of μ_r and ε_r, one can obtain the solutions for the actual medium of ε_r and μ_r from the corresponding TLM solutions as follows:

$$\mathbf{E}\ of\ actual\ medium = \mathbf{E}\ of\ TLM\ solutions \tag{2.84}$$
$$\mathbf{H}\ of\ actual\ medium = \mathbf{H}\ of\ TLM\ solutions \tag{2.85}$$
$$\delta t\ of\ actual\ medium = (\Delta t\ of\ TLM\ solutions)/2 \tag{2.86}$$
$$\sigma\ of\ actual\ medium = \sigma\ of\ TLM\ solutions \quad (if\ applicable) \tag{2.87}$$

For the 3D TLM expanded node and 3D TLM asymmetrical condensed node, the same conclusions can be drawn.

2.5.2 Conversion of the TLM solutions for dual modes

Sometimes it is necessary to make an H-field equivalent to the voltage in the 2D TLM shunt node model to simulate TE waves (TE-to-y). In this case, the variable capacitance is equivalent to a variable permeability instead of a variable permittivity as indicated in [39]. Therefore, for a dielectric-loaded structure, conversion of the simulation solutions is indispensable.

Still consider a 2D TLM shunt node model shown in Fig.2.6. The corresponding FD-TD formulations for the voltages and currents are (2.35) to (2.45).

On the other hand, TE waves can be expressed by the following equations:

$$H_x = H_z = 0, \quad E_y = 0, \tag{2.88}$$

$$\frac{\partial H_y}{\partial x} = \varepsilon_0 \varepsilon_r \frac{\partial E_z}{\partial t}, \tag{2.89}$$

$$\frac{\partial H_y}{\partial z} = -\varepsilon_0 \varepsilon_r \frac{\partial E_x}{\partial t}, \tag{2.90}$$

$$\frac{\partial E_x}{\partial z} - \frac{\partial E_z}{\partial x} = -\mu_r \mu_0 \frac{\partial H_y}{\partial t} \tag{2.91}$$

or,

$$H_x = H_z = 0, \quad E_y = 0, \tag{2.92}$$

$$\frac{\partial(-B_y)}{\partial x} = -\mu_0 \frac{\partial D_z}{\partial t}, \tag{2.93}$$

$$\frac{\partial(-B_y)}{\partial z} = +\mu_0 \frac{\partial D_x}{\partial t}, \tag{2.94}$$

$$\frac{\partial D_x}{\partial z} - \frac{\partial D_z}{\partial x} = \mu_r \varepsilon_r \varepsilon_0 \frac{\partial(-B_y)}{\partial t} \tag{2.95}$$

where $D_x = \varepsilon_r \, \varepsilon_0 \, E_x$, $D_z = \varepsilon_r \, \varepsilon_0 \, E_z$ and $B_y = \mu_0 \, H_y$.

By finite-differencing the above equations and doing the similar averaging process as in Section 2.3, one can easily derive the FD-TD formulations for the TE waves which are exactly the same as (2.35) to (2.45) under the following correspondence:

$$B_y \; of \; actual \; medium \equiv -\sqrt{2}\, V_y, \tag{2.96}$$

$$D_z \; of \; actual \; medium \equiv I_x, \tag{2.97}$$

$$D_x \; of \; actual \; medium \equiv -I_z, \tag{2.98}$$

$$\delta x = \delta z = \delta \; of \; actual \; medium = \Delta l \tag{2.99}$$

$$\mu_0 \equiv L \tag{2.100}$$

$$\mu_r \, \varepsilon_r \, \varepsilon_0 \equiv C \tag{2.101}$$

$$\delta t \; actual \; medium = \Delta t/\sqrt{2}. \tag{2.102}$$

That is, the above equations have to be applied to compute the field components when the 2D TLM shunt node is used for TE waves with a H-field equivalent to the voltage in the TLM mesh. Note that C in the TLM model is now corresponding to the product of ε_r and μ_r. This implies that adding stubs to increase C in the TLM dual mode simulations corresponds to changing either permittivity or permeability of the medium to be modeled.

2.6 Numerical Results

The new FD-TD formulation (or TLM method) and Yee's FD-TD method have been compared for the 2D case by computing the normalized cutoff frequency of the finned waveguide shown in Fig.2.8. Normal Impulse excitations are chosen for the new FD-TD (or TLM) simulations while the Yee's FD-TD simulations are excited by updating the field quantities at source points as described in [56].

Table 2.1 shows that both numerical solutions converge to the result given by transverse resonance method [46] as the number of mesh points is increased while the number of iterations remains the same for both methods. It can be seen that the new formulation has slightly better accuracy than Yee's finite-difference method. The reason is believed to be that in the new model, more field components, including both tangential electric and magnetic field components at points between nodes, are computed or taken into account. Furthermore, the field components are not separated in space, and they are all defined at a single location in the new formulation. As a consequence, the TLM method renders more accurate modelling than Yee's FD-TD scheme, especially at source points and boundaries.

Fig.2.9 shows the convergence of the numerical solutions with increasing number of iterations for $b/\Delta l = 4$. It can be seen that the new FD-TD formulation converges more rapidly than Yee's FD-TD method in term of number of iterations. This is achieved at the expense of increased computational expenditure since each iteration with the new FD-TD formulation takes slightly more time due to the fact that more field components of each cell are calculated. It was found that the total CPU time required for both methods was almost the same for the similar accuracy . Even in this case, the new formulation provides better field resolution due to the fact that the field components are evaluated in a larger number of positions in space. In addition, as the number of iterations increases, the new algorithm converges smoothly to its stable solution while Yee's scheme displays

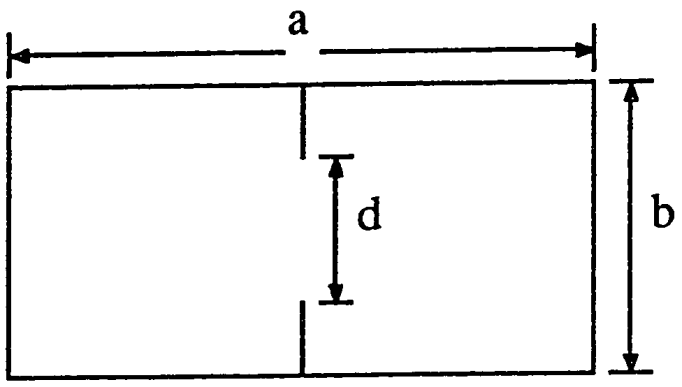

(a) Cross-section of a finned rectangular waveguide

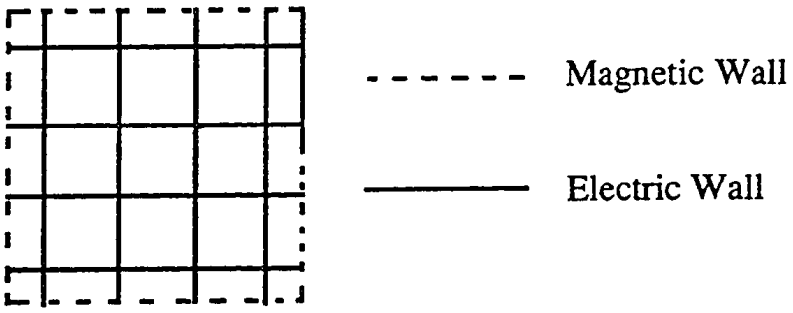

(b) Two-dimensional mesh arrangement for the waveguide shown in (a). Through Introduction of symmetry conditions, only one half of the cross section is required for the analysis of the TE_{10} mode. Note that the boundaries are dual to thoses in the real structure.

Figure 2.8: Geometry of the Finned Waveguide

TABLE I

The normalized cutoff frequency of the finned waveguide obtained with the new FD-TD or TLM method and the TD-FD on Yee's scheme

$b/\Delta\ell$	Results of New FD-TD or TLM b/λ_c	Results of the FD-TD of Yee's scheme b/λ_c	Result of the Transverse Resonance b/λ_c	Errors compared with the Transverse Resonance (%)	
				The New FD-TD method or TLM	The FD-TD on Yee's scheme
4	0.2051	0.2050	0.2249	8.80	8.85
8	0.2155	0.2155		4.18	4.18
12	0.2189	0.2174		2.67	3.33
16	0.2206	0.2196		1.91	2.36
20	0.2217	0.2184		1.42	2.13
24	0.2224	0.2221		1.11	1.24

Table 2.1: Numerical Results for the Normalized Cutoff Frequencies of the Finned Waveguide

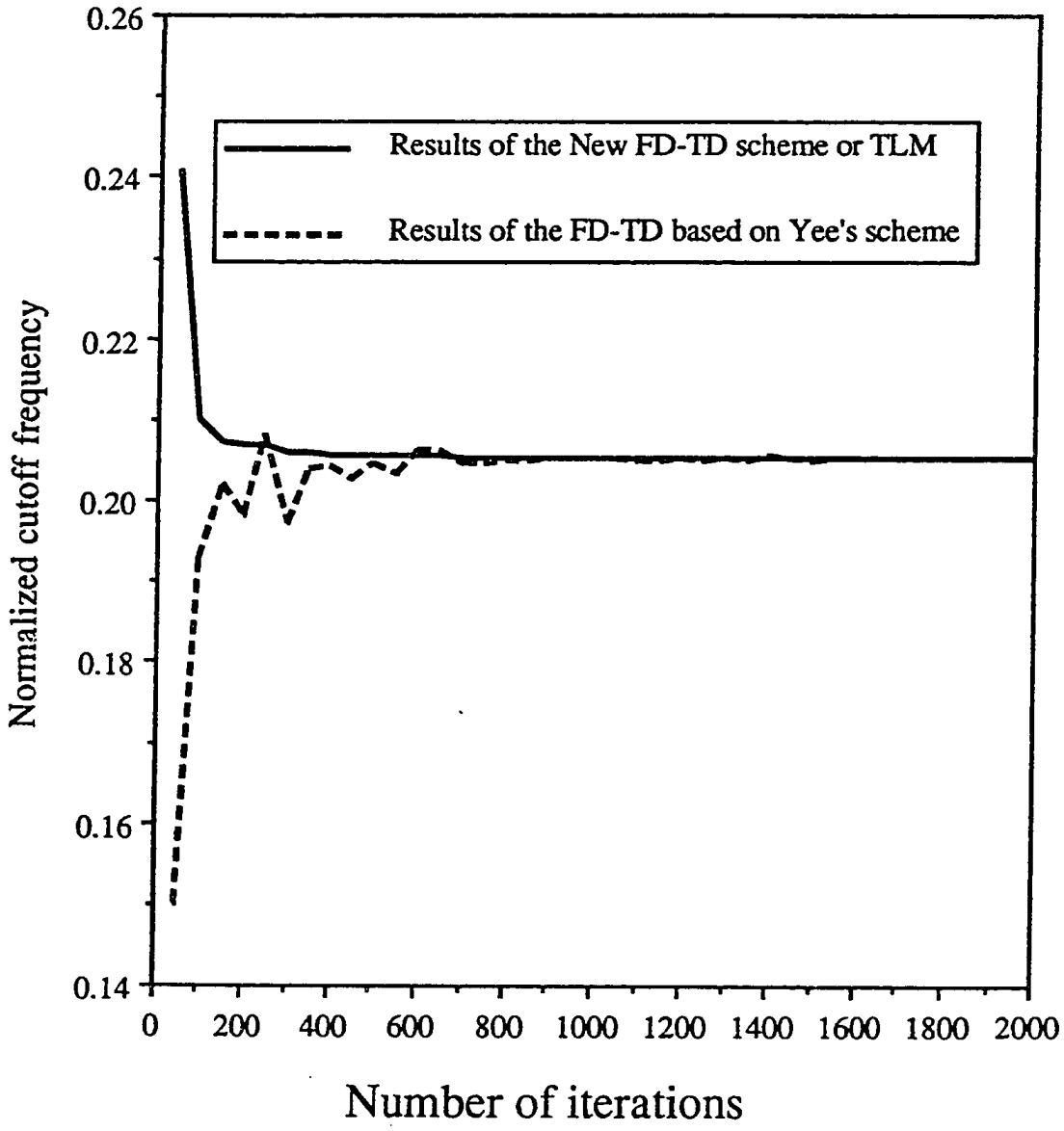

Figure 2.9: The Convergence of the Numerical Solutions with Increasing Number of Iterations

some oscillatory convergence in this case. This can be explained again by the fact already mentioned that in the new FD-TD formulation (or the TLM model), more field components are computed. It would lead to different ways of excitations and boundary treatments from the Yee's FD-TD scheme, generating different solution path for convergence.

2.7 Conclusion

In this chapter, a new FD-TD formulation for Maxwell's equation, which is different from that of Yee's scheme presently used, has been proposed. The new finite-difference scheme, formulated by the finite-difference Maxwell's equations and an averaging process, forms a kind of 'condensed' model in which both electric and magnetic field components are defined at nodes and between nodes. As a result, more accurate modeling than Yee's scheme for solving electromagnetic problems are obtained. This has been verified by comparing the two finite-difference formulations for the 2D cases in computing the normalized cutoff frequency of a finned waveguide. For 3D case, the 3D TLM symmetrical condensed node has been proven to have less numerical dispersion than the 3D FD-TD method of Yee's scheme [66].

While the origins of the FD-TD method and the TLM Symmetrical Condensed Node (SCN) algorithm are different, their equivalence has been demonstrated. In other words, the TLM (SCN) algorithm can be exactly rewritten in finite difference recursive forms, and vice versa. Generally speaking, any TLM scheme, for instance, the Hexagonal TLM node [36], could or can find their equivalent FD-TD formulation since both schemes resemble the same kind of time-stepping approach. The equivalence between the FD-TD and TLM method actually implies a mapping between field quantities and circuit parameters. For the TLM method, the field quantities in Maxwell's equations are mapped to the correspondent circuit parameters such as voltages, currents, capacitance, inductance and so on.

On the other hand, in spite of the equivalence, both the TLM algorithm and FD-TD scheme are believed to be the two parallel numerical techniques for solving transient electromagnetic problems. Both methods retain their respective advantages when implementing boundaries, dispersive constitutive parameters, and nonlinear devices. The finite-difference formulation has a simpler algorithm in the sense that constitutive parameters are directly introduced while the TLM model has certain advantages in the modeling of boundaries

and the partitioning of the computational domain using Johns Matrix techniques. The choice between TLM or FD-TD is based more on personal preferences and familiarity with one or the other method rather than on objective criteria.

Chapter 3

Boundary Treatments Of The TLM Method Based On Its FD-TD Formulations

3.1 Introduction

Boundary treatments play a very important role in both the 2D and 3D TLM simulations. The conventional boundary conditions deal with electric wall, magnetic wall, non-reflecting wall for plane waves and interface between two dielectric media. They have been applied for many years without explicit theoretical verifications. By employing the equivalence between the FD-TD scheme and the TLM method, this problem has been resolved as shown in the following sections. Consequently, a much more systematic way to derive the boundary conditions for the TLM method has been developed. As a by-product, a new boundary description for the TLM method has been proposed where boundaries are placed at nodes rather than halfway between nodes. This renders the TLM scheme more flexibility in positioning its boundaries.

3.2 Theoretical Verification of the Conventional TLM Boundary Conditions

Various types of boundary conditions have been proposed and applied for many problems. These boundary conditions can be verified theoretically as shown in the following sections.

3.2.1 Boundary conditions for perfect reflecting walls

Denote E_t and H_t as the tangential electric and magnetic field components at the boundary, respectively. Then, for the perfect reflecting wall (Fig.3.1a), one has:

$$E_t = 0 \quad if\ C\ is\ an\ electric\ wall \tag{3.1}$$

$$H_t = 0 \quad if\ C\ is\ a\ magnetic\ wall \tag{3.2}$$

As mentioned in Section 2.4, the total voltages and currents halfway between nodes are the sum and difference of incident and reflected impulses; hence, the voltage and current at the boundary (Fig.3.1b) are $V = V^i + V^r$ and $I = (V^i - V^r)/Z_o$. According to the equivalence equations, (2.46) to (2.48) and (2.60) to (2.63), $E_t \equiv V = V^i + V^r$ and $H_t \equiv \pm I = \pm(V^i - V^r)/Z_o$. Consequently, the boundary conditions in TLM models corresponding to (3.1) and (3.2) are:

$$V^r = -V^i \quad if\ C\ is\ an\ electric\ wall \tag{3.3}$$

$$V^r = V^i \quad if\ C\ is\ a\ magnetic\ wall \tag{3.4}$$

which are indeed the conventional boundary conditions [3] already used for many applications. V^i is the impulse incident on the boundary while V^r is the impulse reflected by the boundary and determined by the boundary condition.

3.2.2 Non-reflecting boundary conditions for plane waves

For a uniform plane wave shown in Fig.3.2, non-global reflection condition requires that

$$\frac{E_t}{H_t} = \pm\frac{Z}{cos(\theta)} \tag{3.5}$$

where θ is the incident angle of the plane wave (angle between the wave propagation direction and the inward normal vector of the boundary) and Z is the intrinsic wave impedance of the medium virtually being modeled by the TLM mesh. Again, since $E_t \equiv V = V^i + V^r$ and $H_t \equiv \pm I = \pm(V^i - V^r)/Z_o$ (Z_o is the characteristic impedance of link lines of the TLM network),

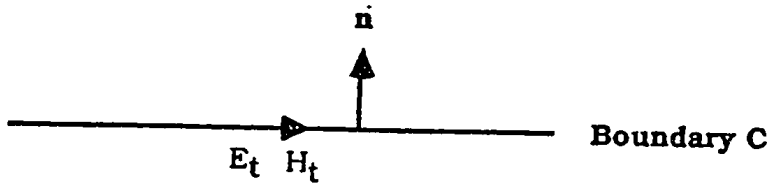

(a) A Perfect Reflecting Wall

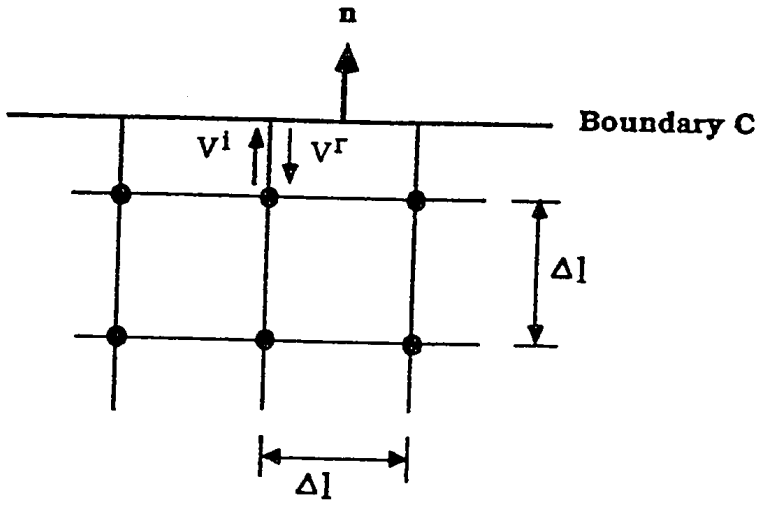

(b) TLM Simulation with the Perfect Reflecting Wall

Figure 3.1: A Boundary Wall

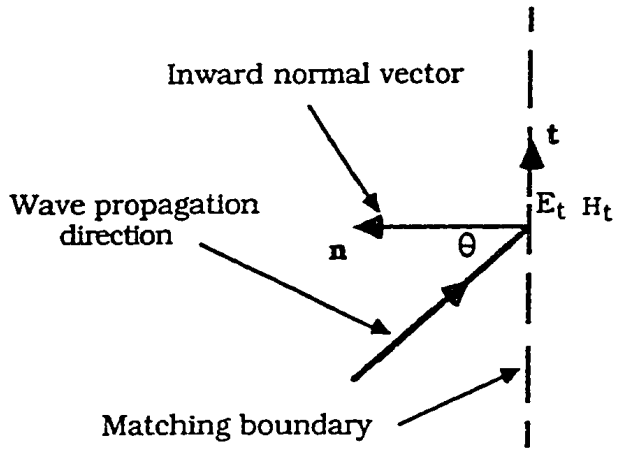

(a) Wave propagating at θ to the matching boundary

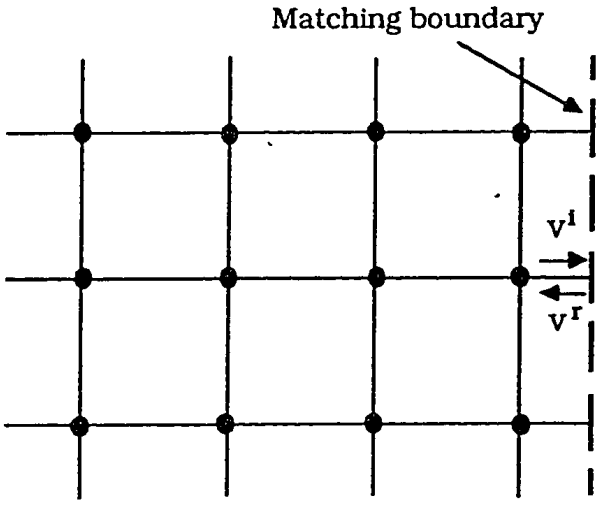

(b) The TLM Simulation with the matching boundary

Figure 3.2: The TLM Simulation of a Uniform Plane Wave with a Matching Boundary

$$\frac{V}{I} = \frac{V^i + V^r}{\pm(V^i - V^i)/Z_o} = \pm\frac{Z}{cos(\theta)} \tag{3.6}$$

Then

$$V^r = \frac{1 - cos(\theta)(Z/Z_0)}{1 + cos(\theta)(Z/Z_0)}\, V^i \tag{3.7}$$

which is exactly the conventional boundary condition for the uniform plane wave. For example, consider a 2D TLM shunt node simulating a plane wave normally incident on the boundary ($\theta = 0$). Then, $Z = Z_o/\sqrt{2}$ for free space. Consequently, $V^r = \frac{1-\sqrt{2}}{1+\sqrt{2}} V^i$. Numerical simulations have shown the good absorption of this condition.

3.2.3 Interfacing conditions between two different media

For the interface of two media modeled by two TLM networks with link line characteristic impedances Z_{01} and Z_{02} (Fig.3.3), respectively, the continuity conditions require that

$$E_{1t} = E_{2t} \tag{3.8}$$

$$H_{1t} = H_{2t} \tag{3.9}$$

Once again,

$$E_{1t} \equiv V_1 = V_1^i + V_1^r \tag{3.10}$$

$$H_{1t} \equiv \pm I_1 = \pm(V_1^i - V_1^r)/Z_{01} \tag{3.11}$$

$$E_{2t} \equiv V_2 = V_2^i + V_2^r \tag{3.12}$$

$$H_{2t} \equiv \pm I_2 = \mp(V_2^i - V_2^r)/Z_{02} \tag{3.13}$$

Then

$$V_1^i + V_1^r = V_2^i + V_2^r \tag{3.14}$$

$$(V_1^i - V_1^r)/Z_{01} = -(V_2^i - V_2^r)/Z_{02} \tag{3.15}$$

where V_k^i is the impulse incident on the interface from region k and V_k^r is the impulse scattered into region k from the interface, $k = 1, 2$.

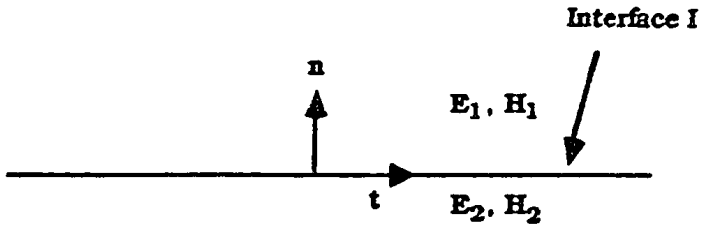

(a) An Interface between two media with different permittivities and permeabilities

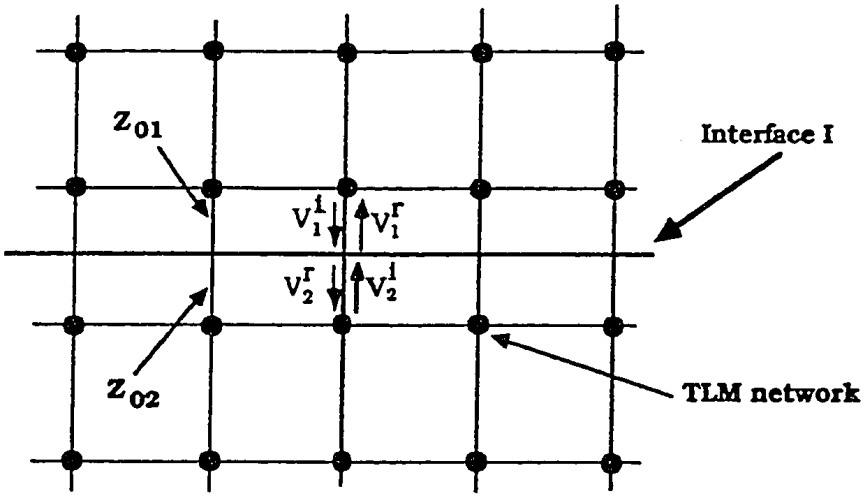

(b) TLM simulation for (a)

Figure 3.3: An Interface of Two Media with Different Intrinsic Impedances

As a result, one can have the following TLM interface conditions:

$$V_1^r = \Gamma_{11} V_1^i + T_{12} V_2^i \tag{3.16}$$

$$V_2^r = T_{21} V_1^i + \Gamma_{22} V_2^i \tag{3.17}$$

With

$$\Gamma_{11} = \frac{1-r}{1+r} \tag{3.18}$$

$$T_{21} = \frac{2}{1+r} \tag{3.19}$$

$$\Gamma_{22} = \frac{r-1}{r+1} \tag{3.20}$$

$$T_{12} = \frac{2r}{1+r} \tag{3.21}$$

where $r = Z_{01}/Z_{02}$, Γ_{ji} and T_{ji} are the voltage reflection and transmission coefficients of a pulse incident on medium j from medium i, and $i, j = 1, 2,$.

If $Z_{01} = Z_{02}$, $r = 1$, $\Gamma_{11} = 0$, $T_{21} = 1$, $\Gamma_{22} = 0$, and $T_{12} = 1$. This means that the impulses are simply transmitted through the interface without any reflections and losses. Note that the TLM networks mentioned above are either the 3D TLM node models or 2D TLM node models for non-dual mode simulations.

In the case of dual modes for the 2D TLM simulations, the situation is different since the H-field is made equivalent to the voltage as discussed in Section 2.5.2. Suppose that there exist two media with different permittivities and permeabilities $(\varepsilon_0\varepsilon_{r1},\ \mu\mu_{r1})$, $(\varepsilon_0\varepsilon_{r2},\ \mu\mu_{r2})$, respectively.

Still, the boundary conditions at the interface require:

$$E_{1t} = E_{2t} \tag{3.22}$$

$$H_{1t} = H_{2t} \tag{3.23}$$

However, according to the equivalence equations, (2.96) to (2.98),

$$E_{1t} = \frac{D_{1t}}{\varepsilon_{r1}\varepsilon_0} \equiv \pm\frac{I}{\varepsilon_{r1}\varepsilon_0} = \pm\frac{V_1^i - V_1^r}{Z_{01}\ \varepsilon_{r1}\varepsilon_0} \tag{3.24}$$

$$H_{1t} = \frac{B_{1t}}{\mu_0} \equiv \frac{V}{\mu_0} = \frac{V_1^i + V_1^r}{\mu_0} \tag{3.25}$$

$$E_{2t} = \frac{D_{2t}}{\varepsilon_{r2}\varepsilon_0} \equiv \pm\frac{I}{\varepsilon_{r2}\varepsilon_0} = \mp\frac{V_2^i - V_2^r}{Z_{02}\,\varepsilon_{r2}\varepsilon_0} \tag{3.26}$$

$$H_{2t} = \frac{B_{2t}}{\mu_0} \equiv \frac{V}{\mu_0} = \frac{V_2^i + V_2^r}{\mu_0} \tag{3.27}$$

Therefore, one has:

$$\Gamma_{11} = \frac{1-r}{1+r} \tag{3.28}$$

$$T_{21} = \frac{2}{1+r} \tag{3.29}$$

$$\Gamma_{22} = \frac{r-1}{r+1} \tag{3.30}$$

$$T_{12} = \frac{2r}{1+r} \tag{3.31}$$

with $r = \frac{\varepsilon_{r1} Z_{01}}{\varepsilon_{r2} Z_{02}}$. For instance, assume that $Z_{01} = Z_{02}$, $\mu_{r1} = 1$, $\varepsilon_{r1} = 1$, $\mu_{r2} = 1$ and $\varepsilon_{r2} = 2.45$. Then $r = 1/2.45$. If $\mu_{r1} = 1$, $\varepsilon_{r1} = 1$ and $\mu_{r2} = \sqrt{2.45}$, $\varepsilon_{r2} = \sqrt{2.45}$. Then $r = 1/\sqrt{2.45}$. These results are exactly the same as in [39]

At this point, the most often used conventional boundary conditions for the TLM method has been verified theoretically. It should be pointed out that any boundary conditions, which are expressed in terms of field quantities, can be transformed into the corresponding conditions for the TLM simulations by following a similar procedure of derivations as shown above. Therefore, a systematic way to construct boundary conditions for TLM simulations has been developed.

3.3 The New Boundary Description for the TLM Models

Unlike the conventional TLM treatments where the boundaries are placed halfway between nodes, the new boundary conditions are formulated by enforcing the boundary conditions across nodes. In a TLM model, the voltages and currents at nodes are equivalent to the electric and magnetic fields in the real structures. Therefore, by imposing the field boundary conditions upon voltages and currents on the boundary or interface nodes of the TLM model, the new boundary representation can be easily obtained. In the followings,

this procedure will be discussed for the case of a 2D TLM shunt-connected network for simplicity although it can be expanded to the 3D TLM simulations in a similar way.

3.3.1 Representation of perfect electric walls

Consider the empty half-space bounded by a perfect electric wall to the y-z plane, as shown in Fig.3.4a . Assuming that $\partial/\partial y = 0$, one can model this half-space by a shunt-connected 2D TLM mesh in which the node voltage V_y simulates the y-component of the electric field E_y (See Fig.3.4b). Unlike the conventional arrangement, the mesh position is such that a row of nodes coincides with the electric wall. The boundary condition, $E_y = 0$, is now simulated by numerically forcing V_y to vanish at each iteration at all boundary nodes. Referring to Fig.3.4c, the value of V_y at the kth iteration is [67]

$$ {}_kE_y \equiv {}_kV_y = \frac{1}{2}({}_kV_1^i + {}_kV_2^i + {}_kV_3^i + {}_kV_4^i) = 0 \quad (\textit{at the boundary nodes}) \tag{3.32} $$

where ${}_kV_j^i$ is the incident voltage on the jth branch of the node on the boundary at the kth iteration. Since in this case, ${}_kV_1^i$, ${}_kV_2^i$, and ${}_kV_4^i$ have been computed at the previous iteration, the impulse ${}_kV_3^i$ to be injected via the 'outside branch' is

$$ {}_kV_3^i = -({}_kV_1^i + {}_kV_2^i + {}_kV_4^i) \tag{3.33} $$

Once ${}_kV_3^i$ is determined, the impulse voltage scattered from the node on the four branches are obtained in the same way as at all the other nodes of the mesh. The impulse ${}_{k+1}V_3^r$ leaving the boundary node via 'outside branch' is simply absorbed by a matched load. Note that this boundary description is a purely numerical procedure, performed only at discrete node locations along the boundary. The TLM mesh lines that lie in the boundary plane (boundary branches) are not physically short-circuited by the wall (except at the nodes). To the contrary, they form an integral part of the TLM network and carry the tangential fractions of the discretized Huygens waves emanating from the boundary nodes.

It can be easily shown that this boundary algorithm conserves the energy in the system. The reflected impulse voltage ${}_{k+1}V_3^r$ absorbed in the outside branch at each iteration is

$$ {}_{k+1}V_3^r = \frac{1}{2}({}_kV_1^i + {}_kV_2^i + {}_kV_3^i + {}_kV_4^i) - {}_kV_3^i \tag{3.34} $$

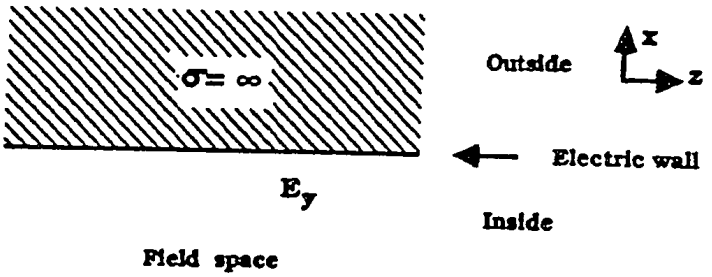

(a) An Electric Wall

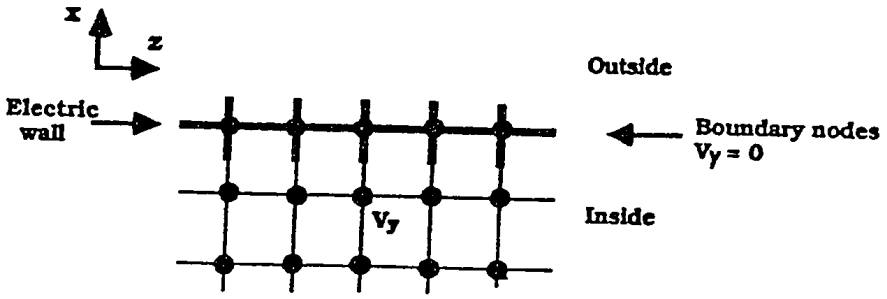

(b) The TLM Simulation With Electric Wall Placed Across the Nodes

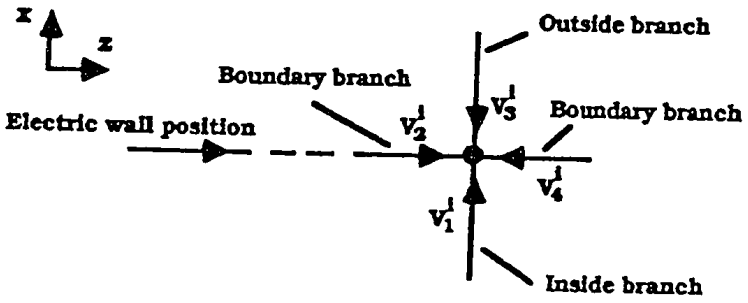

(c) The Electric Wall Placed Across a Node

Figure 3.4: A Perfect Electric Wall

Replacing ${}_kV_3^i$ in the bracket by (3.33), one obtains

$$ {}_{k+1}V_3^r = -{}_kV_3^i \tag{3.35}$$

Since the energy content of each impulse is proportional to the square of the voltage, the energy lost at each iteration at a boundary node is equal to the energy injected, thus ensuring conservation. The boundary treatment can be generalized for a 2D TLM mesh which is equipped with permittivity and lossy stubs. A boundary node in such a mesh is shown in Fig.3.5. Again, the node voltage ${}_kV_y$ must vanish at each iteration:

$$ {}_kV_y = \frac{2}{y}({}_kV_1^i + {}_kV_2^i + {}_kV_3^i + {}_kV_4^i + y_o\ {}_kV_5^i) \tag{3.36}$$

which yields the impulse voltage to be injected via the 'outside' branch as

$$ {}_kV_3^i = -({}_kV_1^i + {}_kV_2^i + {}_kV_4^i + y_o\ {}_kV_5^i) \tag{3.37}$$

where ${}_kV_j^i$ is the incident voltage on the jth branch of the node on the boundary at the kth iteration ($j = 1, ...5$), $y = 4 + y_o + g_o$, y_o is the normalized characteristic admittance of the permittivity stub, and g_o is the normalized characteristic admittance of loss stub. In both case, the normalizing admittance is the characteristic admittance of the link lines.

Since there exists a dual two-dimensional TLM model in which the currents correspond to the electric fields, we have [67]:

$$ {}_kE_z \equiv {}_kI_x = {}_kV_3^i - {}_kV_1^i = 0 \tag{3.38}$$

which leads to

$$ {}_kV_3^i = {}_kV_1^i \tag{3.39}$$

(3.37) and (3.39) are the new boundary descriptions for a perfect electric wall in which the unknown incident voltage ${}_kV_3^i$ injected via an 'outside' branch is determined in terms of the incident voltages on the other branches, rather than in terms of reflection coefficients.

3.3.2 Representation of perfect magnetic walls

A similar arrangement can be made for perfect magnetic walls where the normal component of the electric field or the tangential component of the magnetic field must vanish. If the

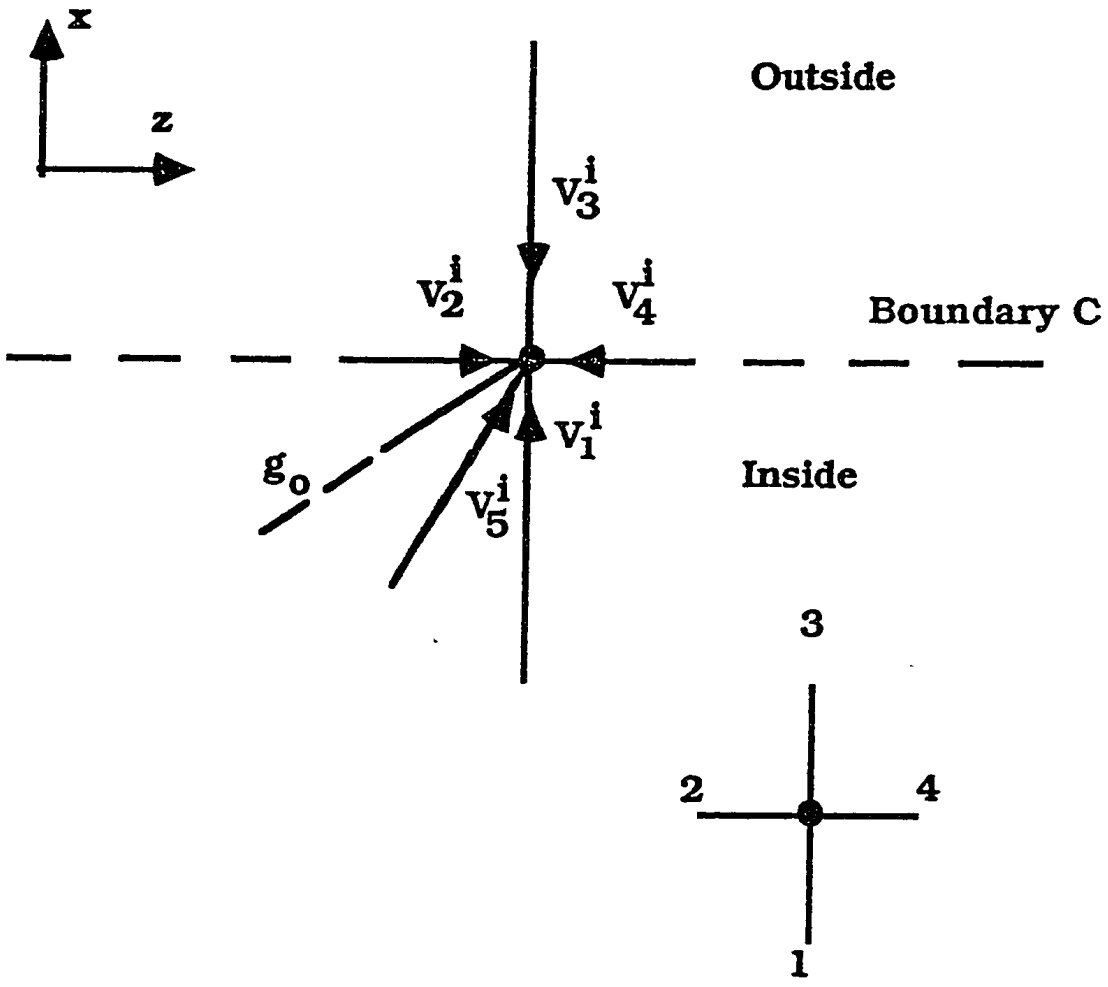

Figure 3.5: A TLM Boundary Node with Stubs

boundary C in Fig.3.4a is a perfect magnetic wall, one can set:

$$ {}_kV_3^i = {}_kV_1^i \tag{3.40} $$

where the currents in the TLM mesh correspond to magnetic fields, and

$$ {}_kV_3^i = -({}_kV_1^i + {}_kV_2^i + {}_kV_4^i + y_o\,{}_kV_5^i) \tag{3.41} $$

where the voltages in the TLM mesh correspond to the magnetic fields. It is obvious that (3.40) and (3.41) are similar in the form to(3.39) and (3.37), given the dual properties of electric and magnetic walls. Thus, only two formulas are needed in the new boundary representation to describe both electric and magnetic walls.

3.3.3 Representation of interfaces between dielectric regions

In the case of two dielectric regions Fig.3.6, two separate TLM networks for modeling region 1 and region 2 are needed. The connection of the two TLM networks on the interface should be done in consistency with the field boundary conditions. Also, one must account for the dual TLM models. When the electric fields are equivalent to the voltages in the TLM mesh [67], one has

$$ {}_kE_{1t} \equiv {}_kV_{1y} = \frac{2}{y_1}({}^1_kV_1^i + {}^1_kV_2^i + {}^1_kV_3^i + {}^1_kV_4^i + {}_1y_o\,{}^1_kV_5^i) \tag{3.42} $$

$$ {}_kH_{1t} \equiv {}_kI_{1x} = {}^1_kV_3^i - {}^1_kV_1^i \tag{3.43} $$

$$ {}_kE_{2t} \equiv {}_kV_{2y} = \frac{2}{y_2}({}^2_kV_1^i + {}^2_kV_2^i + {}^2_kV_3^i + {}^2_kV_4^i + {}_2y_o\,{}^2_kV_5^i) \tag{3.44} $$

$$ {}_kH_{2t} \equiv {}_kI_{2x} = {}^2_kV_3^i - {}^2_kV_1^i \tag{3.45} $$

where ${}^n_kV_j^i$ is the incident voltage on branch j in the TLM network for region n ($n = 1, 2$, and $j = 1, ...5$) at the kth iteration. $y_n = 4 + {}_ny_o + {}_ng_o$, ${}_ny_o$ is the normalized characteristic admittance of the permittivity stub for region n, and ${}_ng_o$ is the normalized characteristic admittance of the lossy stub of the TLM network for region n. In order to satisfy the continuity conditions for the tangential electric and magnetic fields on the interface,

$$ {}_kV_{1y} = {}_kV_{2y} \tag{3.46} $$

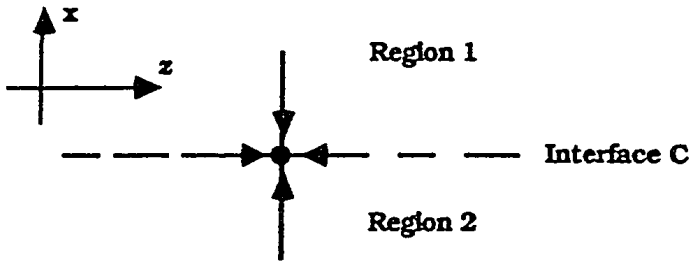

(a) Two regions with different dielectrics

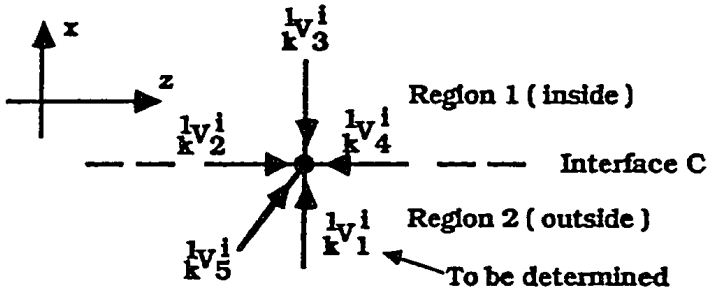

(b) TLM network for region 1

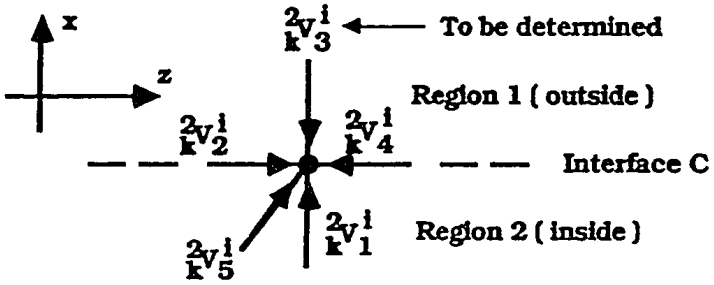

(c) TLM network for region2

Figure 3.6: Two Regions with Different Dielectrics

$$ {}_kI_{1x} = {}_kI_{2x} \tag{3.47} $$

which leads to the following boundary representations:

$$ {}^1_kV^i_1 = (p+q)/(s+1) \tag{3.48} $$

$$ {}^2_kV^i_3 = (sq-p)/(s+1) \tag{3.49} $$

where $s = y_2/y_1$

$p = ({}^2_kV^i_1 + {}^2_kV^i_2 + {}^2_kV^i_4 + {}_2y_o\,{}^2_kV^i_5) - s\,({}^1_kV^i_2 + {}^2_kV^i_3 + {}^2_kV^i_4 + {}_1y_o\,{}^1_kV^i_5)$ and $q = {}^1_kV^i_3 + {}^2_kV^i_1$.

When the magnetic fields are equivalent to the voltage on the TLM mesh as shown in (2.96) to (2.98). Then,

$$ {}_kH_{1t} \equiv -\sqrt{2}\,\frac{{}_kV_{1y}}{\mu_0} = \frac{-2\sqrt{2}}{y_1\,\mu_0}({}^1_kV^i_1 + {}^1_kV^i_2 + {}^1_kV^i_3 + {}^1_kV^i_4 + {}_1y_o\,{}^1_kV^i_5) \tag{3.50} $$

$$ {}_kE_{1t} \equiv \frac{{}_kI_{1x}}{\varepsilon_0\varepsilon_{r1}} = \frac{1}{\varepsilon_{r1}\,\varepsilon_0}({}^1_kV^i_3 - {}^1_kV^i_1) \tag{3.51} $$

$$ {}_kH_{2t} \equiv -\sqrt{2}\,\frac{{}_kV_{2y}}{\mu_0} = \frac{-2\sqrt{2}}{y_2\,\mu_0}({}^2_kV^i_2 + {}^2_kV^i_2 + {}^2_kV^i_3 + {}^2_kV^i_4 + {}_2y_o\,{}^2_kV^i_5) \tag{3.52} $$

$$ {}_kE_{2t} \equiv \frac{{}_kI_{2x}}{\varepsilon_0\varepsilon_{r2}} = \frac{1}{\varepsilon_{r2}\,\varepsilon_0}({}^2_kV^i_3 - {}^2_kV^i_2) \tag{3.53} $$

Then, the field boundary conditions of the interface require that

$$ {}_kV_{1y} = {}_kV_{2y} \tag{3.54} $$

$$ {}_kI_{1x}/\varepsilon_{r1} = {}_k\,I_{2x}/\varepsilon_{r2} \tag{3.55} $$

which leads to the following:

$$ {}^1_kV^i_1 = \frac{p+q}{s_1+s_2} \tag{3.56} $$

$$ {}^2_kV^i_3 = \frac{s_1\,q - s_2\,p}{s_1+s_2} \tag{3.57} $$

where $s_1 = y_2/y_1$, $s_2 = \epsilon_{r2}/\epsilon_{r1}$,
$p = ({}^{2}_{k}V^i_1 + {}^{2}_{k}V^i_2 + {}^{2}_{k}V^i_4 + {}_2y_o\, {}^{2}_{k}V^i_5) - s_1({}^{1}_{k}V^i_2 + {}^{1}_{k}V^i_3 + {}^{1}_{k}V^i_4 + {}_1y_o\, {}_{1k}V^i_5)$,
and $q = s_2\, {}^{1}_{k}V^i_3 + {}^{1}_{k}V^i_1$.

Equations (3.48),(3.49),(3.56) and (3.57) are the new interface conditions formulated for two adjacent dielectric regions. (3.48) and (3.49) is the special case of (3.56) and (3.57) with $s_2 = 1$. Therefore, only two formulas are needed to describe the interface conditions between two dielectric regions.

So far, the new TLM boundary representations have been derived for dielectric interfaces and for ideal electric and magnetic walls. By following the similar procedure, it is not difficult to obtain the new boundary formulas for the series node network and for other kinds of boundary conditions, for example the interface conditions between two regions with two different permeabilities. In addition, the new boundary conditions can be applied to lossy boundaries, 3D TLM analysis and to TLM models used in other areas such as thermodynamics, optics, and acoustics.

3.3.4 Numerical results

The new boundary description has been verified by applying it to three typical 2D problems and comparing the results with values obtained from the conventional TLM method using the same mesh size and number of iterations.

Fig.3.7(b) gives the normalized cutoff frequencies for TM modes in a square waveguide with sizes $10\Delta l$, shown in Fig.3.7a.

The slow-wave properties of the transmission-line matrix gives automatically the solutions for a medium of relative permittivity of 2 within the guide. The calculations have been performed for 500 iterations.

Fig.3.8(b) shows the normalized cutoff frequencies of the dominant mode of the simple inhomogeneously filled waveguide in 3.8(a) computed with 100 iterations. The results are compared with the reference values used by Johns [39]. The width of the guide ranges from $5\Delta l$ to $20\Delta l$, with a dielectric permittivity of 2.45. The interface conditions described in section 2.3 above have been applied.

Fig.3.9(b) shows the normalized dominant mode cutoff frequency of the finned waveg-

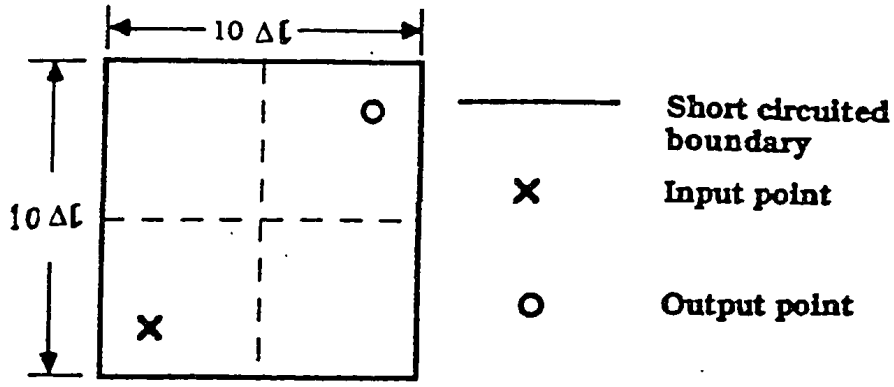

(a) Configuration of the Rectangualar Waveguige

NORMALIZED CUTOFF FREQUENCY OF HIGH ORDER MODES IN SQUARE WAVEGUIDE

Mode	Result from this method $\Delta\ell/\lambda_c$	Result from conventional TLM $\Delta\ell/\lambda_c$	Analytical result $\Delta\ell/\lambda_c$	Error of this method %	Error of conventional TLM %
TM12	0.0788	0.0788	0.0791	0.38	0.38
TM22	0.0999	0.0999	0.1000	0.10	0.10
TM13	0.1103	0.1104	0.1118	1.34	1.25
TM23	0.1270	0.1269	0.1275	0.39	0.47
TM14	0.1418	0.1414	0.1458	2.74	3.02
TM33	0.1499	0.1498	0.1550	0.07	0.13
TM24	0.1558	0.1558	0.1581	1.45	1.45
TM34	0.1760	0.1760	0.1768	0.45	0.45
TM25	0.1840	0.1841	0.1904	3.36	3.31
TM44	0.1997	0.1996	0.2000	0.15	0.20

Maximum truncation error not greater than 0.2 %

Dimensions 10 $\Delta\ell$

(b) Normalized Cutoff Frequency of Higher Order Modes in the Square Rectangular Waveguide

Figure 3.7: Normalized Cutoff Frequencies in the Square Rectangular Waveguide

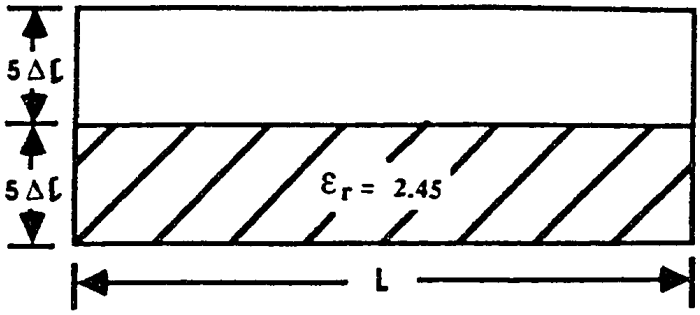

(a) Sross Section of A Simple Inhomogeneously filled waveguide

NORMALIZED CUTOFF FREQUENCIES OF QUASI - H_{10} MODE IN INHOMOGENEOUSLY FILLED RECTANGULAR CAVITY

Guide width L	Result from this method	Result from conventional	Analytical result	Maximum truncation error	Maximum velocity error
$\Delta\ell$	$\Delta\ell/\lambda_c$	$\Delta\ell/\lambda_c$	$\Delta\ell/\lambda_c$	%	%
5	0.0784	0.0781	0.0791	0.4	0.4
6	0.0690	0.0692	0.0693	0.6	1.6
7	0.0621	0.0625	0.0630	0.8	1.2
10	0.0518	0.0518	0.0518	1.2	0.9
20	0.0411	0.0413	0.0415	1.8	0.5

ε_r = 2.45

(b) Numerical Results for the Inhomogeneously Filled Waveguide

Figure 3.8: Numerical Results for the Inhomogeneously Filled Waveguide

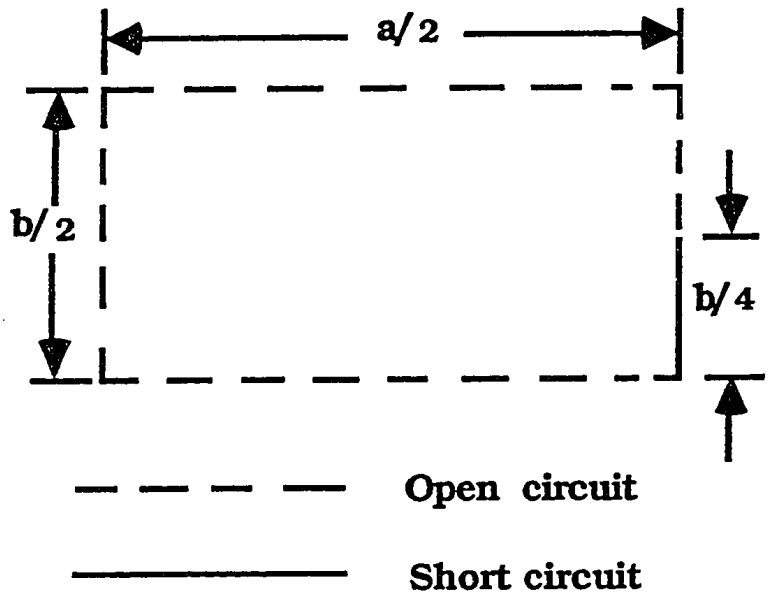

(a) A Simplified Geometry of a Finned Waveguide

NORMALIZED CUTOFF FREQUENCY OF THE FINNED WAVEGUIDE

Result of this method	Result of conventional TLM	Analytical result
b/λ_c	b/λ_c	b/λ_c
0.224	0.206	0.225

$a/b=2,\ a/\Delta l = 8$

(b) Comparison of Different Results for the Finned Waveguide

Figure 3.9: Comparison of Different Results for the Finned Waveguide

uide in Fig.3.9(a) obtained with three different methods: the analytical approach using the transverse resonance technique, the TLM method with the conventional boundary conditions and with the new boundary descriptions. It can be seen that the TLM with the new boundary representation gives a more accurate solution than the conventional TLM. This may be explained by the fact that one node placed on the conductor edge produces large (but not infinite) field values. This certainly contributes to a better field description around the fin, hence yielding a better accuracy for parameter evaluations.

The above results show that TLM with the new and traditional boundary representations give results of similar accuracy in general. Furthermore, it has been verified by calculations that the solutions with the new boundary representation converge to the exact solutions when the number of iteration is increased. This indicates that the new boundary description does not introduce convergence problems, instability or spurious solutions and thus is not inferior to the traditional boundary formulation.

3.4 Conclusion

The equivalent field components in the TLM model are defined not only at the nodes (cell centers) but also between the nodes (boundaries of the cells). As a result, the conventional boundary conditions for the TLM simulations has been verified theoretically for the first time, and a systematic way for constructing boundary conditions has been developed. Moreover, a new boundary condition has been described, where the boundaries can be placed just across the nodes. Hence, the TLM schemes become more flexible in positioning its boundaries and all the values of field components at the boundaries would be available directly from the simulations. For this reason, solutions with better accuracy could be obtained for some cases (for example, computation of cutoff frequencies of a finned waveguide). Recently, a moving boundary algorithm, where the boundaries are moved along any points between two neighboring nodes [68], has been achieved. The conventional boundary treatment with boundaries half-way between nodes and the new boundary description with boundaries across nodes are simply the two limit cases of this moving boundary scheme.

Finally, it should be pointed that the results and conclusions from this chapter for developing the TLM boundary conditions can be extended to 3D cases although numerical simulations were done only for the 2D cases.

Chapter 4

Absorbing And Connecting Boundary Conditions In The TLM Simulations

4.1 Introduction

In this chapter, another development for the TLM method, the implementation of absorbing and connecting boundary conditions, is presented. Connecting boundaries are the boundaries which separate scattered field from total fields (of incident and scattered fields) while absorbing boundaries are the boundaries which can simulate the truncated infinite region and allow the waves to propagate through it with minimum reflections. These two conditions are badly needed to limit the computational domain in computer simulation of scattering and radiation problems involving open structures.

To the best of the author's knowledge, not very much has been reported on the implementation of absorbing and connecting boundary conditions in the TLM simulations, except for the work of Eswarappa et. al [30] and Simons [69, 70]. Eswarappa et. al have developed a wideband absorbing boundary scheme by using a dissipation region to gradually damp the wave striking the boundary. However, to get substantial absorption over a wide range of incident angles and wavelengths of striking waves, the dissipation must occupy a region which is several of the largest wavelengths in width. Therefore, it would take much of memory and is not practical for solving the general problems. Simon has employed two other techniques to have absorbing conditions for 2D problems: one is to change the reflection coefficients, at each simulation time step, with the wave incident angles which are predicted by a special field extrapolation routine. The quality of absorption depends

very much on the extrapolation algorithm used. Also, it may not work very well if several plane waves with different incident angles strike the boundary simultaneously; another is to directly apply Higdon's absorbing conditions for the FD-TD method into the 2D TLM simulations. However, this approach doesn't work with 3D TLM symmetrical condensed node due to quickly generated unstable solutions.

On the other hand, various approaches have been developed to implement absorbing boundaries in the FD-TD method in many publications [71]-[88]. Some claimed good absorptions. Among them are Engquist and Majda's [76], Liao's [79], Higdon's [82] and Lindman's [73] absorbing boundary conditions where extrapolation techniques over space and time are employed by approximating the so-called one-way equation. The performance of these conditions in the FD-TD simulation has been studied thoroughly by Blaschak, Kriegsmann [83] and Fang [87], where Lindman's and Higdon's conditions have been shown to have smaller reflections than the others. Recently, a much more simpler absorbing boundary condition has been proposed by Saguet [88], where Taylor's expansion technique is used.

Since each TLM scheme is equivalent to a FD-TD formulation as studied in Chapter II, the absorbing conditions for the FD-TD method can be trans-implemented in the TLM simulations. In this chapter, Higdon's conditions and Taylor's expansion approach are modified and implemented into the 2D and 3D TLM simulations due to their good absorption and simplicity. Validation has been shown with structures of waveguides and two and three dimensional scattering problems.

4.2 One-Way Equation and Its FD-TD Formulations

Numerical modeling and simulations need so called absorbing boundaries, either in the time-domain or frequency-domain, to truncate the volumetric computational domain while keeping the electromagnetic properties of the corresponding original unbounded problems unchanged. They are essential in computer simulations of unbounded problems. One of the efficient techniques used so far is by extrapolation, where filed quantities at boundaries are predicted by a function of field quantities inside the boundaries. A very useful paper for reviewing the developments in this area was presented in the paper by Moore [89]. As described in the paper, two types of absorbing boundary operators exist basically: mode

annihilating and one-way equation technique. Each of these operators possesses different characteristics and forms. Because its easy implementation in Cartesian coordinates (which is more suitable for TLM rectangular mesh models), one-way equation technique is henceforth employed.

One-way equation is a partial differential equation which permits wave propagation only in certain directions. It can be derived analytically. The basic principle is the following: The wave equation in three dimensions can be compactly written as

$$L\,U = 0 \tag{4.1}$$

where L is the wave operator and $U = U(x, y, z, t)$ is the wave function.

The wave operator L can be factored in the following manner:

$$L\,U = L^{+}\;L^{-}\;U = 0 \tag{4.2}$$

While $L^{+}U = 0$ at the boundary allows the wave traveling inward, the application of one-wave operator L^{-} to the wave function U on the boundary, $L^{-}U = 0$ at the boundary, exactly absorbs the wave traveling outward the boundary surface. Generally speaking, the one-wave operator L^{-} is nonlocal in both the space and time variables and requires a lot of memory and computation time. To overcome this, localized and simplified approximating formulations for L^{-}, were proposed. Different ways of constructing the approximation have lead to different absorbing boundary formulations and quality of absorption. As mentioned in the introduction of this chapter, the absorbing condition by Taylor's expansion and Higdon's absorbing boundary conditions are chosen to be implemented into the TLM simulations.

Consider the wave equation

$$\frac{\partial^2 U}{\partial x^2} + \frac{\partial^2 U}{\partial y^2} + \frac{\partial^2 U}{\partial z^2} - \frac{1}{c^2}\frac{\partial^2 U}{\partial t^2} = 0 \tag{4.3}$$

for $t > 0$ on the spatial domain $\Omega = (x, y, z), x < 0$, where $c = 1/\sqrt{\mu\varepsilon}$ with that μ and ε are the permeability and permittivity of the medium being modeled. The goal is to find boundary conditions that cause wave motions from the interior of Ω to pass through the boundary at $x = 0$ with zero or at least minimum reflection (as shown in Fig.4.1). Mathematically, it means to update (or predict) the values of the wave function at the boundary in such a way that the reflections would be minimum.

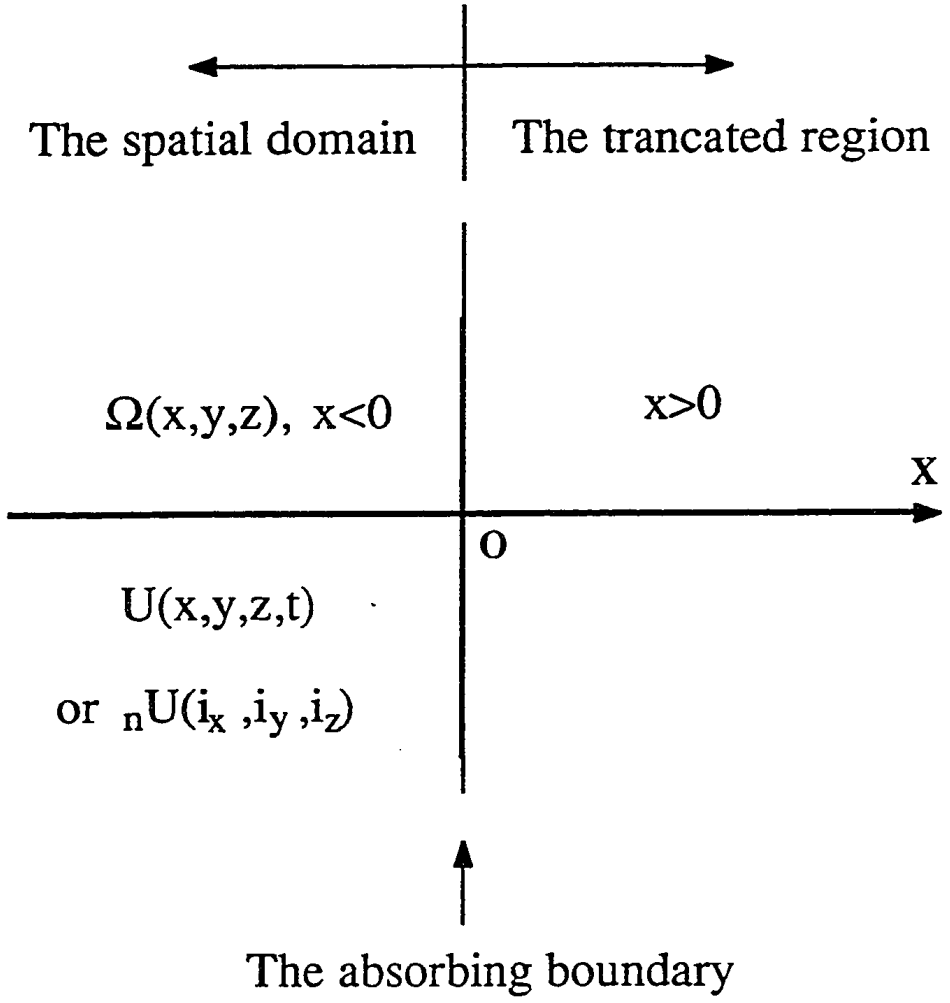

Figure 4.1: **A Spatial Domain with an Absorbing Boundary**

Taylor's expansions Assuming that the wave propagates along the positive X direction, one can have $x - ct = constant$, or $\Delta x/\Delta t = c$ (Δx and Δt are the space and time increments, respectively) for the wave function $U = U(x, y, z, t)$. Then, $U = U(x, y, z, t)$ can be expanded by Taylor's series (Taylor's expansion) along the plane of $x - ct = constant$. As a result, one has:

$$U(0, y, z, t) \approx U(0 - \Delta x, y, z, t - \Delta t) + \sum_{i=1}^{P} \frac{1}{i!} \frac{\partial^i U(0 - \Delta x, y, z, t - \Delta t)}{\partial x^i} (\Delta x)^i \qquad (4.4)$$

where integer P is the order of expansion.

By replacing $U(x, y, z, t)$ with ${}_nU(i_x, i_y, i_z)$ $(= U(i_x \Delta x, i_y \Delta y, i_z \Delta z, n \Delta t))$ and the differential with backward difference, one can easily have the updated value of the wave function at the boundary:

$${}_nU(0, i_y, i_z) \approx_{n-1} U(0 - 1, i_y, i_z) + \sum_{i=1}^{P} \frac{1}{i!} \frac{\nabla^i \, {}_{n-1}U(0 - 1, i_y, i_z)}{(\Delta x)^i} (\Delta x)^i \qquad (4.5)$$

The backward differences are computable since they are evaluated inside the spatial domain Ω. Therefore, the above condition is feasible as the absorbing boundary and can be rewritten as:

$${}_nU(0, i_y, i_z) \approx \sum_{i=1}^{P} a_{i,i} \, {}_{n-i}U(0 - i, i_y, i_z) \qquad (4.6)$$

or,

$$(\sum_{i=0}^{P} a_{i,i} \, D_x^{-i} K^{-i}) \, {}_nU(0, i_y, i_z) = 0 \qquad a_{0,0} = -1 \qquad (4.7)$$

where $a_{i,i}$, $_{i=0,..,P}$, is the constant, $(\sum_{i=0}^{P} a_{i,i} \, D_x^{-i} K^{-i})$ can be considered as the approximation of the one-way operator L^-, and D_x^{-i} and K^{-i} are the space and time shifting operator defined as follow:

$$D_x^{-i} \, {}_nU(i_x, i_y, i_z) =_n U(i_x - i, i_y, i_z) \qquad (4.8)$$

$$K^{-i} \, {}_nU(i_x, i_y, i_z) =_{n-i} U(i_x, i_y, i_z) \qquad (4.9)$$

Table 4.1 shows the different set of $a_{i,i}$ with different orders of the boundaries.

The quality of the above absorbing boundary can be evaluated by examining the reflection coefficients of the boundary. Since the general propagating waves can usually be

Order of the Absorbing Boundary P	Coefficients
1	$a_{11} = 1.0000$
2	$a_{11} = 2.0000$ $a_{22} = -1.0000$
3	$a_{11} = 2.5000$ $a_{22} = -2.0000$ $a_{33} = 0.5000$
4	$a_{11} = 2.6667$ $a_{22} = -2.5000$ $a_{33} = 1.0000$ $a_{44} = -0.1667$
5	$a_{11} = 2.7083$ $a_{22} = -2.6667$ $a_{33} = 1.2500$ $a_{44} = -0.3333$ $a_{55} = 0.0417$

Table 4.1: Coefficients for Different Orders of Taylor's Expansions

expanded as sum of plane waves with different propagation constants, an arbitrary plane wave striking on the boundary can be chosen for this evaluation.

Without loss of generality, suppose that a plane wave U near the boundary at $x = 0$ consists of the wave incident on the boundary with unity amplitude and the wave reflected by the boundary with amplitude of R. That is,

$$ {}_nU(i_x, i_y, i_z) = e^{j(\omega\, n\, \Delta t - k_x\, i_x\, \Delta x + k_y\, i_y\, \Delta y + k_z\, i_z\, \Delta z)} + R\, e^{j(\omega\, n\, \Delta t + k_x\, i_x\, \Delta x + k_y\, i_y\, \Delta y + k_z\, i_z\, \Delta z)} \quad (4.10) $$

where $k_x = k\, cos(\theta)$ (θ is the incident angle and k is the wave number). By substituting (4.10) into (4.7), one can easily obtain the reflection coefficients R of the Taylor's expansion boundary conditions. Fig.4.2 shows the reflection coefficients of Taylor's expansions at $\Delta x/\lambda = \Delta l/\lambda = 0.025$) for a medium of $\mu_r = 1$ and $\varepsilon_r = 2$. As one can see, a zero reflection is achieved at 45° incident angle while only a small amount of reflection is generated for incident angles below 55°. Besides, the reflection coefficients do not improve for the boundaries with order beyond three. For this reason, the second or third order boundary condition are recommended and applied for the applications henceforth.

Higdon's absorbing boundary conditions R. L. Higdon [S2] and R. G. Keys [S0] proposed the following form of absorbing conditions:

$$ \prod_{i=1}^{P} \left(\frac{\partial}{\partial x} + \frac{cos(\theta_i)}{c}\, \frac{\partial}{\partial t}\right) U(x, y, z, t) = 0 \quad (4.11) $$

where θ_i, $_{i=1,\ldots,P}$ is the incident angle at which the wave is supposed to be exactly absorbed. The above condition has been claimed to provide a general and optimal representation among those absorbing boundary conditions based on a systematic rational approximation to the portion of the dispersion relation corresponding to outgoing waves [S2]. In other words, (4.11) is the optimized boundary conditions for wide-angle absorptions. In this sense, θ_i can be chosen the same as those obtained in [S4] with the different optimization criteria for wide-angle absorption. However, in general, the choice of θ_i depends on the configuration of the problem in order to have best absorption. For example, θ_i may be chosen to take advantage of a *prior* information about the directions from which the particular wave motions approach the boundary.

Now, take difference approximations to both $\frac{\partial}{\partial x}$ and $\frac{\partial}{\partial t}$; the difference equation of (4.11)

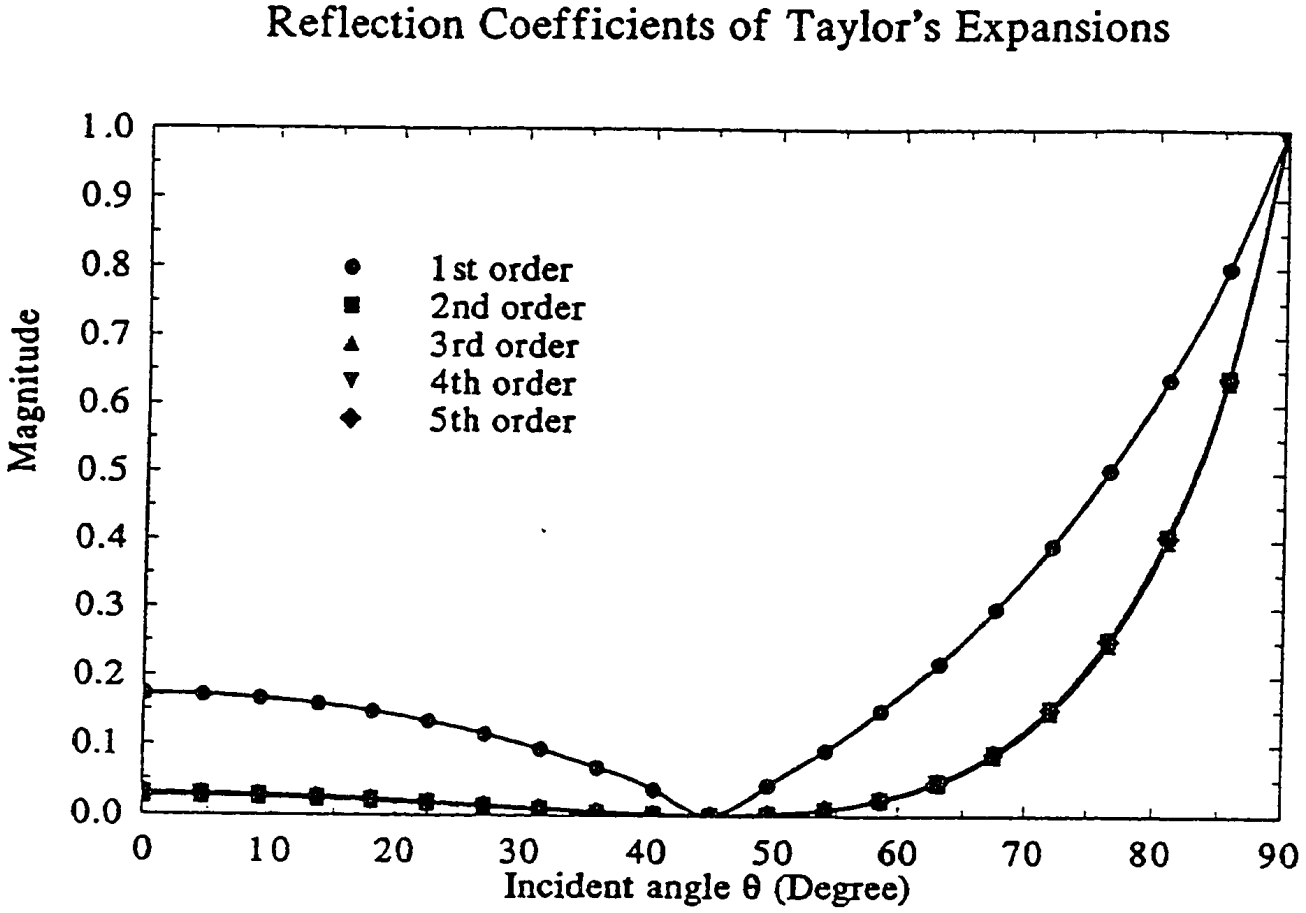

Figure 4.2: **Reflection Coefficients of Taylor's Expansions**

is:

$$\prod_{i=1}^{P}[(\frac{1-D_x^{-1}}{\Delta x})\frac{(1+K^{-1})}{2}+\frac{cos(\theta_i)}{c}(\frac{1-K^{-1}}{\Delta t})(\frac{1+D_x^{-1}}{2})]\ {}_nU(0,i_y,i_z)=0 \qquad (4.12)$$

The above equation can also expressed in another way:

$${}_nU(0,i_y,i_z)=\sum_{i1=0}^{P}\sum_{i2=0}^{P}a_{i1,i2}\ {}_{n-i2}U(0-i1,i_y,i_z) \quad a_{0,0}=0 \qquad (4.13)$$

or,

$$(\sum_{i1=0}^{P}\sum_{i2=0}^{P}a_{i1,i2}D_x^{-i1}K^{-i2})\ {}_nU(0,i_y,i_z) \quad a_{0,0}=-1 \qquad (4.14)$$

where $a_{i1,i2}$ is the constant independent of different problems, $(\sum_{i1=0}^{P}\sum_{i2=0}^{P}a_{i1,i2}D_x^{-i1}K^{-i2})$ can be considered as the approximation of the one-way operator L^-, and ${}_nU(0,i_y,i_z)$ is the updated value of the wave function.

Table 4.2 gives some values of $a_{i1,i2}$ for a medium of $\varepsilon_r=2$ and $\mu_r=1$ as references.

Similarly to the computation for Taylor's expansion, the reflection coefficients of Higdon's absorbing conditions can be evaluated. The results are shown in Fig.4.3 and Fig.4.4. It can be seen from Fig.4.4 that the Higdon's conditions has slightly smaller reflections than Taylor's expansion.

In fact, both Higdon's conditions and Taylor's expansion can be generally expressed mathematically by (4.14). That is, the wave at the boundary is predicted by a linear function of waves inside and on the boundary at the previous time steps. While the different ways of deriving constants, $a_{i1,i2}$, as a consequence of different types of approximations, have lead to different types of absorbing conditions, they are essentially the method of extrapolation. The wave function is expanded, under certain conditions, in space and time domain and the unknown is then expressed by a function of known values. Higdon's conditions and Taylor's expansion can be considered as the wave expansion along plane $x-ct=const.$ while some other approaches used the multidimensional expansion, in which tangential components are also employed to obtain the unknown, for instance, Lindman's conditions [73]. An extensive list of different absorbing boundaries and their qualities can be found in [83] and [87]. In the author's point of view, Higdon's absorbing boundary condition and Taylor's expansion pose two of the best absorbing conditions so far. The reasons are that firstly, they are easy to be implemented in the numerical time-stepping modeling and have generally good wave absorption; secondly, they do not encounter so called 'corner

Order of the Absorbing Boundary P	Coefficients $[a_{i1, i2}]$ i1, i2 = 0,1,..,P	
	$\theta_i = 0^\circ$ i = 1,..,P	$\theta_i = 45^\circ$ i = 1,..,P
1	-1.000 -0.1716 0.1716 1.000	-1 0 0 1
2	-1.000 -0.3431 -0.02944 0.3431 2.059 0.3431 -0.02944 -0.3431 -1.000	-1 0 0 0 2 0 0 0 -1
3	-1.000 -0.4902 -0.08010 -0.004363 0.4902 3.017 0.9468 0.07629 -0.08010 -0.9468 -2.874 -0.4446 0.004363 0.07629 0.4446 0.8638	-1 0 0 0 0 3 0 0 0 0 -3 0 0 0 0 -1
4	-1.000 -0.6239 -0.1460 -0.01518 -0.0005919 0.6238 3.928 1.747 0.2678 0.01380 -0.1460 -1.747 -5.493 -1.588 -0.1206 0.01518 0.2678 1.588 3.247 0.4687 -0.0005919 -0.01380 -0.1206 -0.4687 -0.6830	-1 0 0 0 0 0 4 0 0 0 0 0 -6 0 0 0 0 0 4 0 0 0 0 0 -1
5	-1.000 -0.7149 -0.2044 -0.02923 -0.002089 -0.00005975 0.7149 4.576 2.471 0.5194 0.04901 0.001741 -0.2044 -2.471 -7.979 -3.125 -0.4329 -0.02030 0.02923 0.5194 3.125 6.649 1.716 0.1183 -0.002089 -0.04901 -0.4329 -1.716 -2.648 -0.3448 0.00005975 0.001741 0.02030 0.1183 0.3448 0.4019	-1 0 0 0 0 0 0 5 0 0 0 0 0 0 -10 0 0 0 0 0 0 10 0 0 0 0 0 0 -5 0 0 0 0 0 0 1

$\varepsilon_r = 2$ and $\mu_r = 1$

Table 4.2: Coefficients for Higdon's Absorbing Boundary Conditions

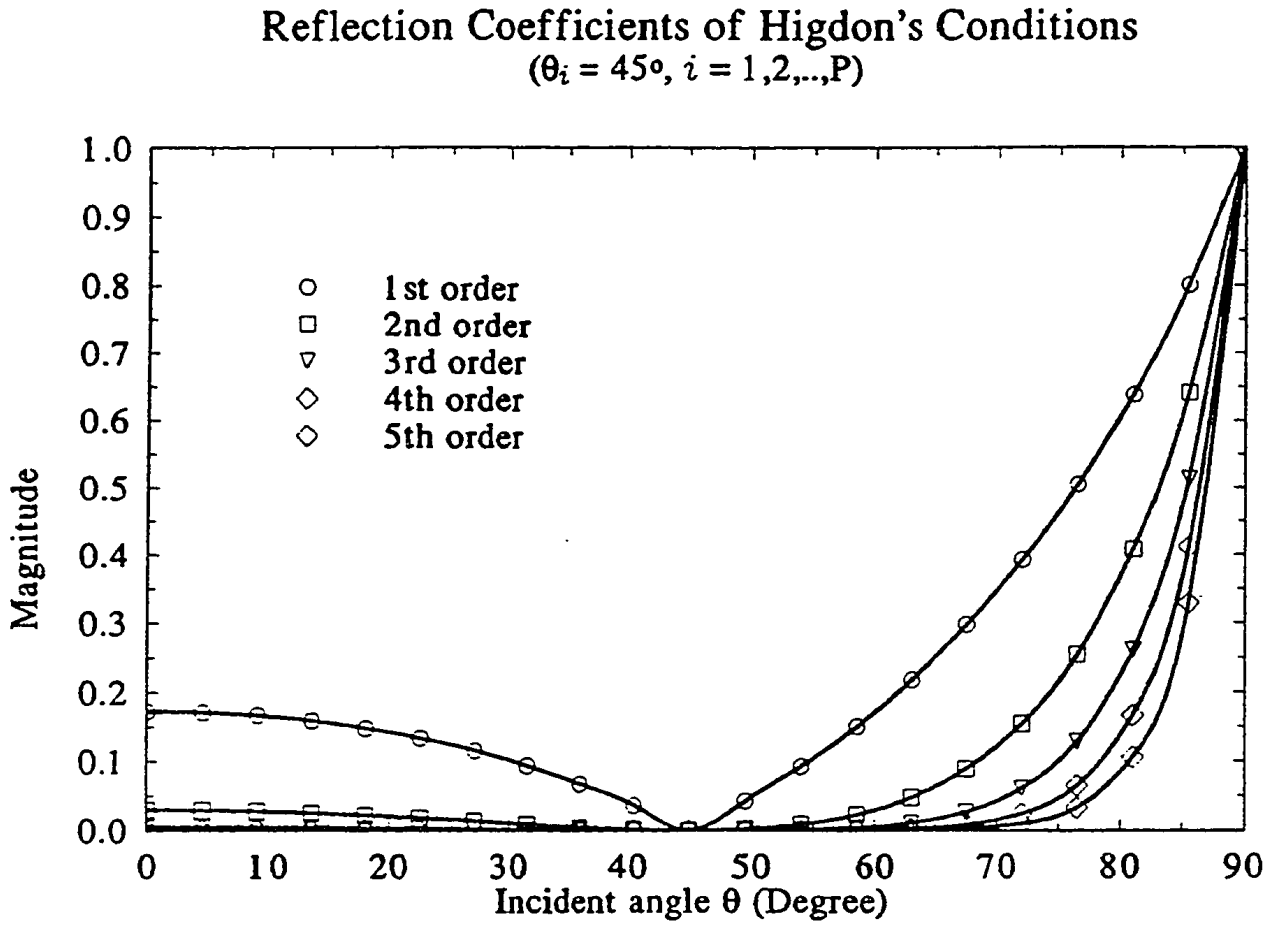

Figure 4.3: Reflection Coefficients of Higdon's Absorbing Boundaries

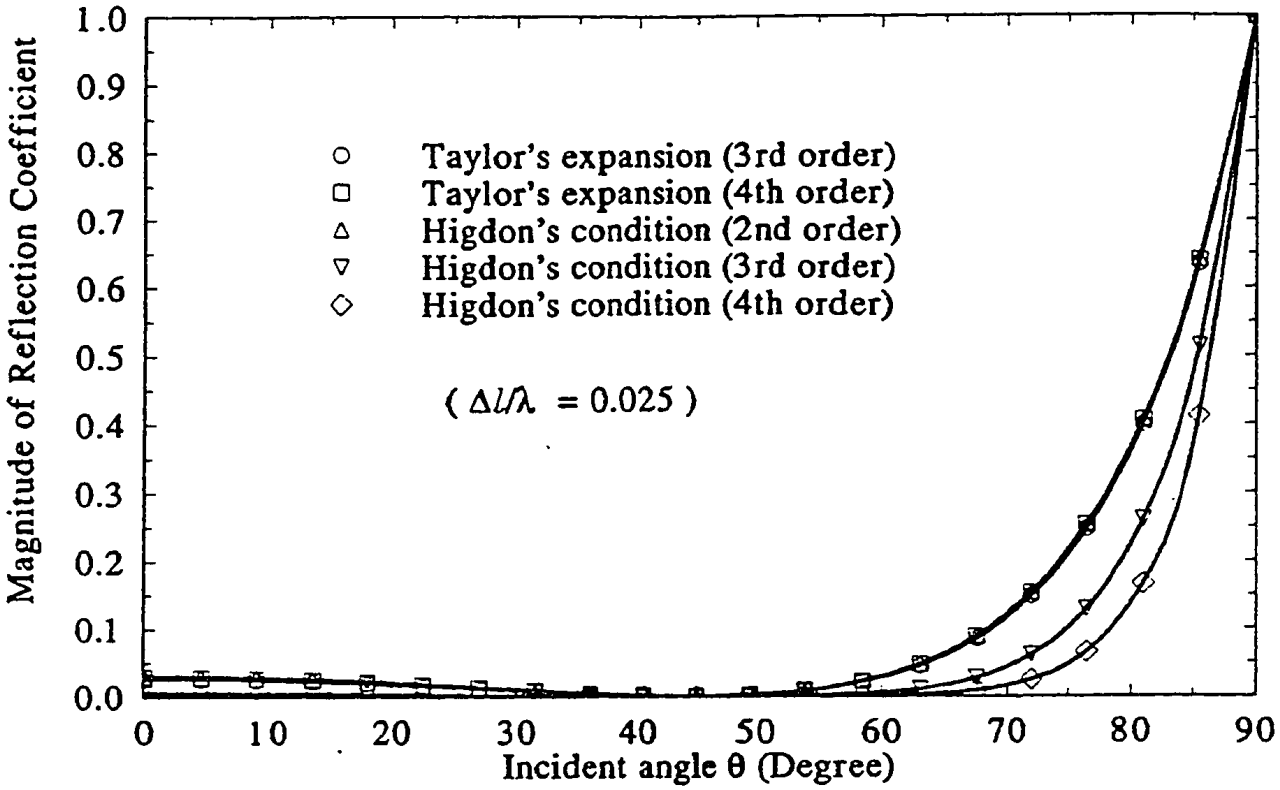

Figure 4.4: Comparisons of Reflection Coefficients of Taylor's Expansion and Higdon's Conditions

problem'—tangential components, which are needed for some absorbing conditions, are not available at edges or corners; thirdly, Higdon's conditions allow the incident angles at which the wave is exactly absorbed to be specified according to *prior* knowledge of the users. Thus, the best absorption of the boundary conditions can be achieved.

4.3 Implementation of the Absorbing Boundary Conditions in the TLM simulations

Consider a spatial domain $\Omega = (x, y, z), x \leq \frac{1}{2}\Delta l$ (Fig.4.5), in which a TLM mesh is positioned and an absorbing boundary is placed at $x = \frac{1}{2}\Delta l$. The objective is to find the impulse reflected by the boundary while maintaining reflections of the wave the impulse represents minimum.

As shown in Chapter II, the impulse in the TLM mesh is actually equivalent to the linear combination of electric and magnetic field components. For example, in Fig.4.5,

$$\begin{aligned} {}_{n+\frac{1}{2}}V^r(0+\frac{1}{2}, i_y, i_z) &= {}_{n+\frac{1}{2}}V(0+\frac{1}{2}, i_y, i_z) + Z_o\, {}_{n+\frac{1}{2}}I(0+\frac{1}{2}, i_y, i_z) \\ &\equiv {}_{n+\frac{1}{2}}E_y(0+\frac{1}{2}, i_y, i_z) \pm Z_o\, {}_{n+\frac{1}{2}}H_z(0+\frac{1}{2}, i_y, i_z) \end{aligned} \tag{4.15}$$

Since E_y and H_z satisfy the wave equation (4.3), the absorbing boundary conditions can be applied to either of them and to the linear combination of them (e.g. ${}_{n+\frac{1}{2}}V^r(0+\frac{1}{2}, i_y, i_z)$ in this case) such that waves propagate through the boundary with minimum reflections. Therefore, the absorbing boundary conditions presented can be generally applied to the impulses in the TLM network directly. That is, in the formulations of the absorbing condition by Taylor's expansion and Higdon's conditions as shown in the last section, wave function U can be considered as impulses V on the link lines of the TLM meshes including to be found at the absorbing boundary in the TLM network. This results in the formulations of the absorbing boundary conditions for the TLM simulations.

4.3.1 Absorbing boundaries for the 2D TLM node

Implementation of the absorbing boundaries in the 2D TLM simulation is relatively easy since the absorbing boundary conditions mentioned above can be directly applied to evaluate the unknown impulses reflected by the boundaries. For instance, consider the 2D TLM

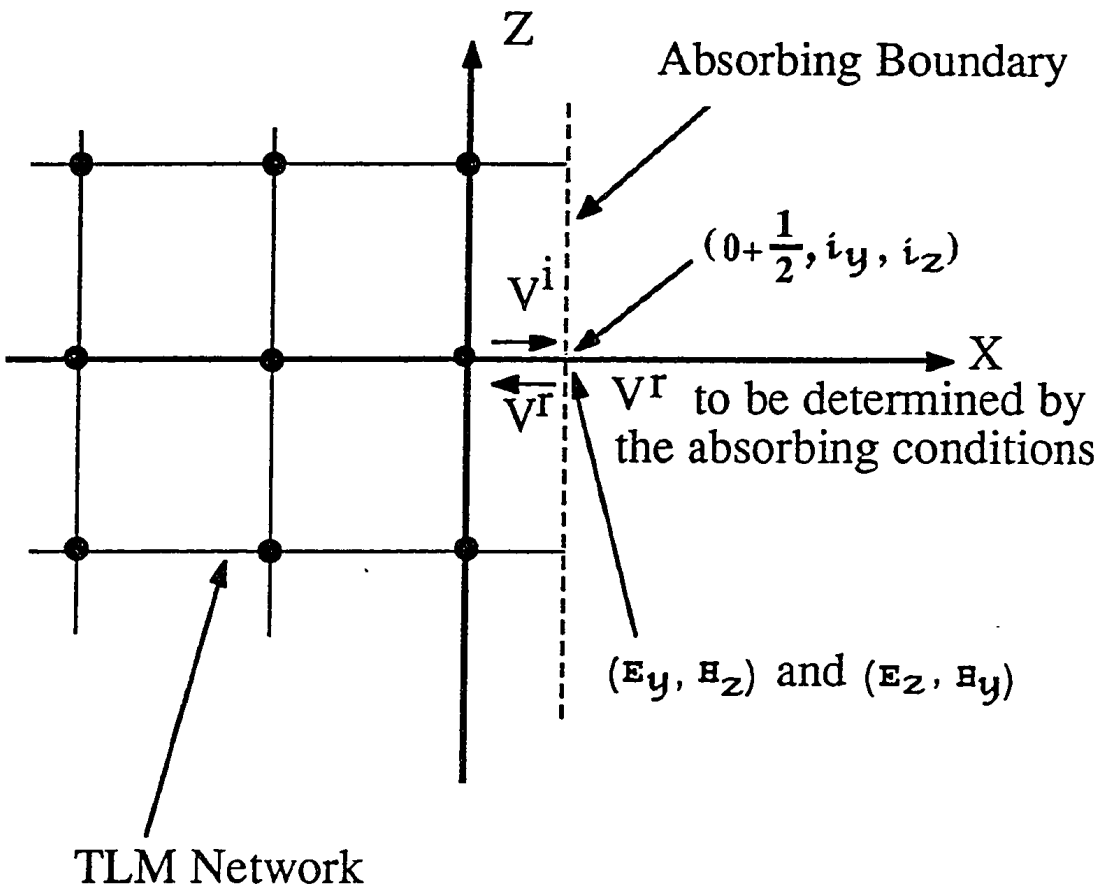

Figure 4.5: An Absorbing Boundary in a TLM mesh

shunt node model as shown in Fig.4.6, an absorbing boundary is placed at $x = 0 + \frac{1}{2}\Delta x$ (halfway between nodes). The impulse ${}_{n+\frac{1}{2}}V_3^r(0+\frac{1}{2}, i_z)$, reflected by the absorbing boundary and to be injected back to the TLM network, can be easily found according to (4.14):

$$ {}_{n+\frac{1}{2}}V_3^r(0+\frac{1}{2}, i_z) = \sum_{i1=0}^{P}\sum_{i2=0}^{P} a_{i1,i2}\ {}_{n+\frac{1}{2}-i2}V_3^r(0+\frac{1}{2}-i1, i_z) = 0 \quad a_{0,0} = 0 \tag{4.16} $$

or,

$$ \sum_{i1=0}^{P}\sum_{i2=0}^{P} a_{i1,i2}\, D_x^{-i1} K^{-i2}\ \ {}_{n+\frac{1}{2}}V_3^r(0+\frac{1}{2}, i_z) = 0 \quad a_{0,0} = -1 \tag{4.17} $$

where $a_{i1,i2}$ are pertinent to different types of absorbing boundaries used.

For the 2D TLM series node, a similar condition can be developed.

4.3.2 Absorbing boundaries for the 3D TLM expanded node and asymmetrical condensed node

Since the 3D expanded node model and the 3D asymmetrical condensed model are evolved from the 2D TLM shunt and series node models, the absorbing boundary conditions for them can be constructed in a similar way to that in the 2D TLM simulation. That is, the impulse, reflected by the boundaries and to be injected back into the TLM network, can be found by the same equation as (4.17) with the only difference of superscripts and subscripts for V. The superscripts and subscripts depend on which link lines are connected to the boundaries.

4.3.3 Absorbing boundaries for the 3D TLM symmetrical condensed node (SCN)

For the 3D TLM SCN, the absorbing boundaries are still valid except that K^{-i1} must be replaced by $K^{-2\,i1}$. The replacement or modification is due to the slow-wave property of the 3D TLM SCN model (the scattered impulse on the link line of a node, resulting from an incident impulse with the same polarization on the link line at the other side of the node , only appears after two time steps $2\,\Delta t$). Consequently, the modified condition can be expressed as the following (referring to Fig.4.7):

$$ \sum_{i1=0}^{P}\sum_{i2=0}^{P} a_{i1,i2}\, D_x^{-i1} K^{-2\,i2}\ \ {}_{n+\frac{1}{2}}V^r_{10\ or\ 11}(0+\frac{1}{2}, i_z) = 0 \quad a_{0,0} = -1 \tag{4.18} $$

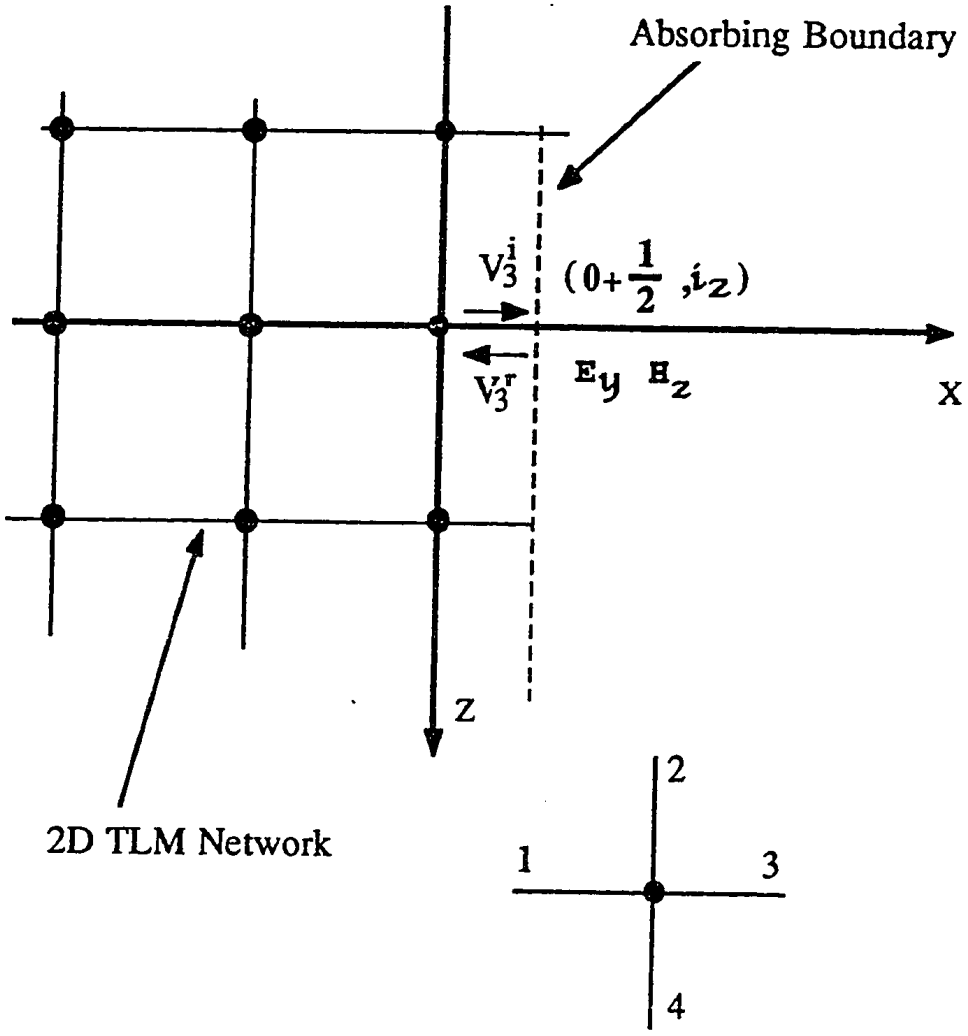

Figure 4.6: A 2D TLM Network with an Absorbing Boundary

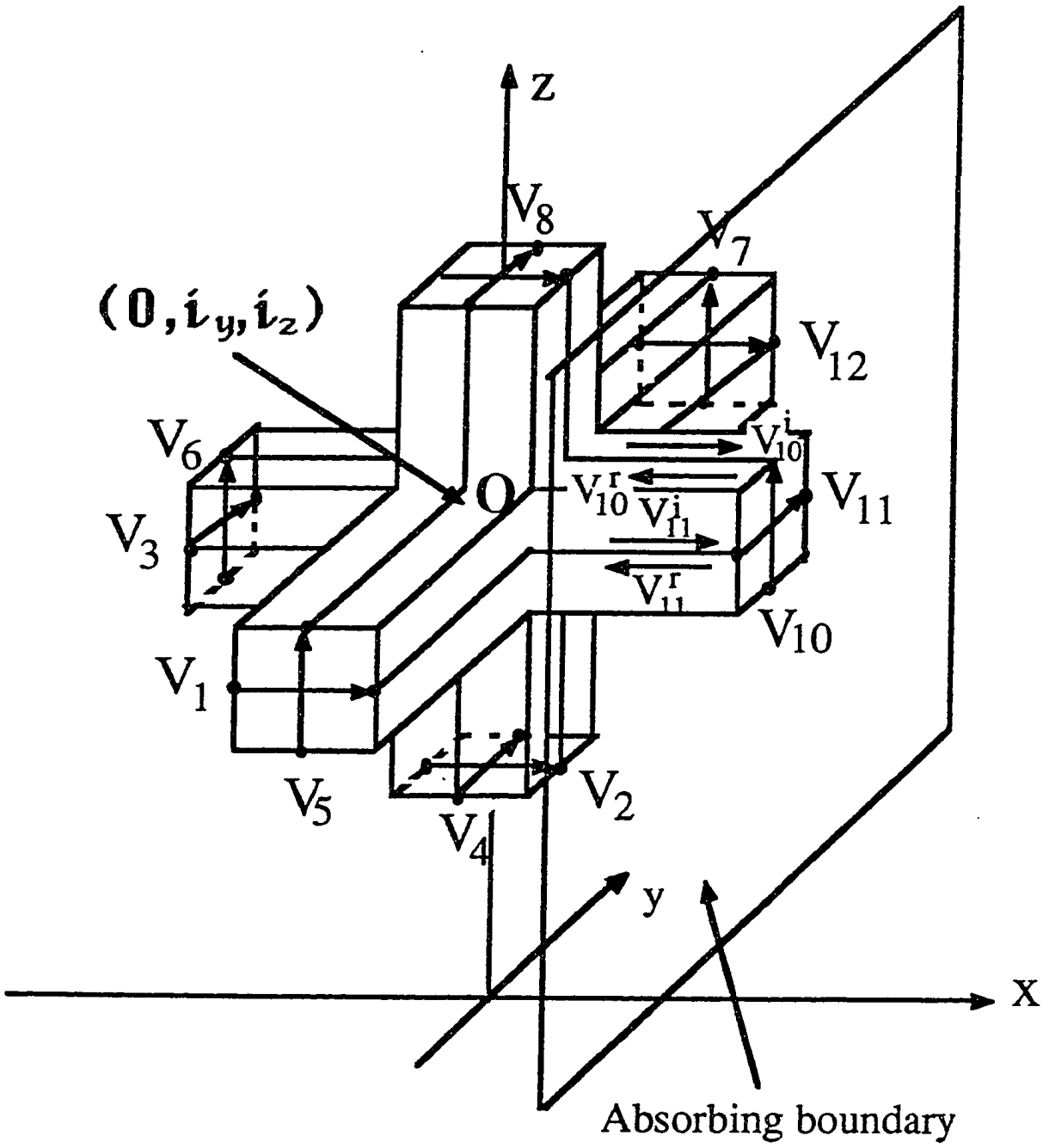

Figure 4.7: A 3D TLM Symmetrical Condensed Node with an Absorbing Boundary

The reflection coefficients of the above absorbing boundaries are very small (Fig.4.8) when the incident angle is around the specified angles θ_i at which the perfect absorption is supposed to occur.

In spite of the above modifications, numerical experience has shown the uncontrollable instability may occur in the simulations as the absorbing conditions are merely directly implemented into the 3D SCN model. The main reason is that spurious modes exist in the 3D TLM SCN model.

Spurious modes and their effects at absorbing boundaries In his paper, Nielsen has shown that due to periodic spatial sampling and symmetry, spurious modes exist in the 3D TLM symmetrical condensed node model [90]. The physical cause behind is that the TLM models can not correctly simulate high spatial-frequency components due to the finite discretization in space. Therefore, the spurious modes will be produced to substitute the high spatial-frequency physical components wherever required.

The existence of the spurious modes can be described quantitively as follows; suppose a physical mode, which is expressed by (4.19) and presented by a sphere centered at origin in the dispersion diagram (Fig.4.9). propagating in the 3D TLM SCN network:

$$ {}_nU(i_x, i_y, i_z) = e^{j(\omega\, n\, \Delta t - k_x\, i_x\, \Delta x + k_y\, i_y\, \Delta y + k_z\, i_z\, \Delta z)} \tag{4.19} $$

with propagation constants k_x, k_y and k_z and temporal frequency ω.

Then, the forward-propagating spurious mode, expressed by (4.20), backward-propagating spurious mode, expressed by (4.21), can propagate, both with the same temporal frequency ω and propagation constants $\overline{k}_x = \frac{\pi}{\Delta x} + k_x$, $\overline{k}_y = \frac{\pi}{\Delta y} + k_y$ and $\overline{k}_z = \frac{\pi}{\Delta z} + k_z$.

$$ {}_nU(i_x, i_y, i_z) = e^{j(\omega\, n\, \Delta t - \overline{k}_x\, i_x\, \Delta x + \overline{k}_y\, i_y\, \Delta y + \overline{k}_z\, i_z\, \Delta z)} \tag{4.20} $$

$$ {}_nU(i_x, i_y, i_z) = e^{j(\omega\, n\, \Delta t + \overline{k}_x\, i_x\, \Delta x + \overline{k}_y\, i_y\, \Delta y + \overline{k}_z\, i_z\, \Delta z)} \tag{4.21} $$

These spurious waves are represented by the spheres centered at (π, π, π) in the dispersion diagram (Fig.4.9) and their propagation constants $\overline{k}_x$, $\overline{k}_y$ and $\overline{k}_z$ are large values because Δx, Δy and Δz are small. Thus, the spurious modes are nonphysical and with high

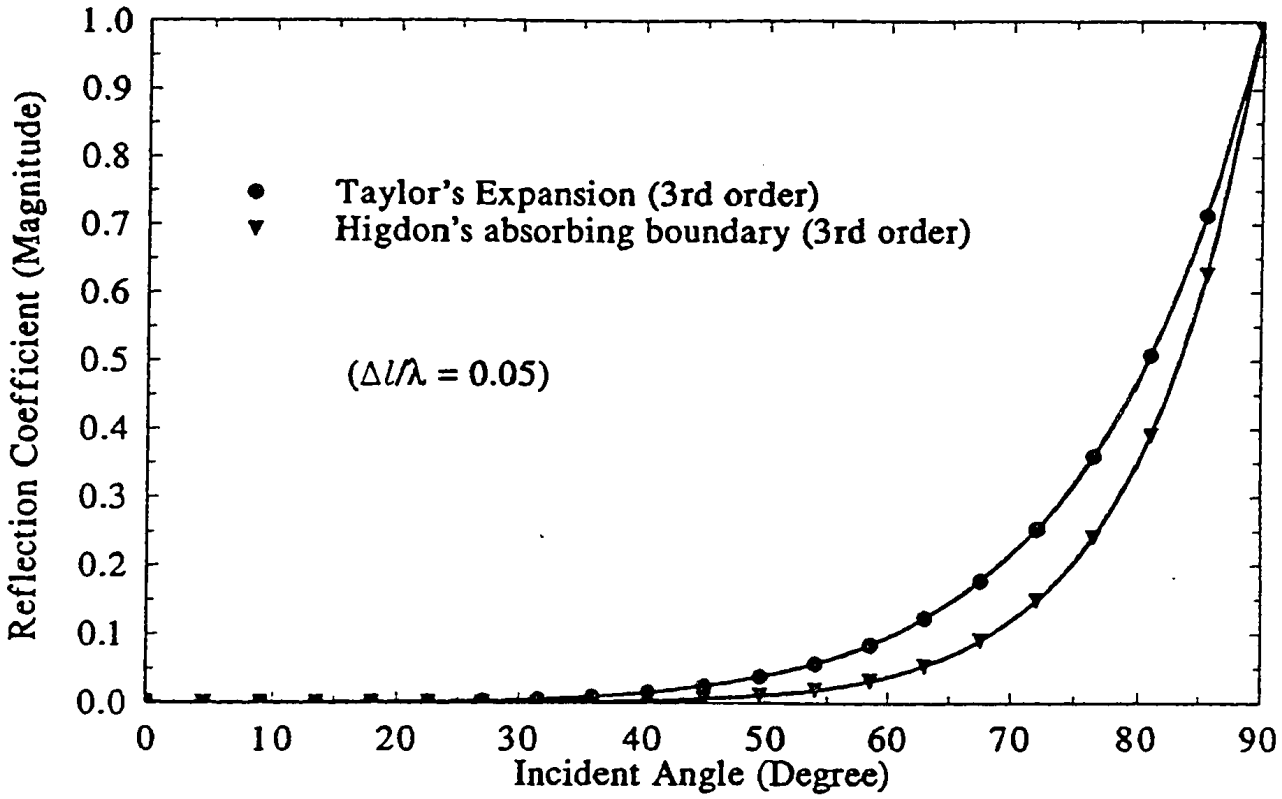

Figure 4.8: The Reflection Coefficients of the Absorbing Boundaries for Physical Modes

spatial frequency contents. They are generated with the spurious excitations and geometry with discontinuities. They can propagate even with low temporal frequency contents.

When the absorbing boundary conditions are applied, the spurious modes can be amplified at the boundary and then reflected back into the computational domain. One can follow the similar procedure for evaluating the reflection coefficients of the absorbing boundaries as described before and obtain reflection coefficients for the spurious modes as shown in Fig.4.10. As can be seen, the reflection coefficients are larger than one. That is, the spurious modes reflected by the absorbing boundaries and to be injected back into the computational domain, contain more energy than the incident spurious modes, leading to instability.

Form the dispersion diagram(Fig.4.9), if any of following equations is satisfied with wave functions, the spurious modes will not be present.

$$k_x \Delta x < \frac{\pi}{2} \tag{4.22}$$

$$k_y \Delta y < \frac{\pi}{2} \tag{4.23}$$

$$k_z \Delta z < \frac{\pi}{2} \tag{4.24}$$

A numerical experiment has proven the above and the instability related to the spurious modes. A section of WR28 rectangular waveguide was chosen with both ends terminated with the absorbing boundaries of either Taylor's expansion or Higdon's conditions described by (4.18). When the lower order modes of TE_{n0}, which satisfy (4.22) to (4.24), were excited, very stable solutions has been obtained since the spurious modes do not exist. However, when the high order modes of TE_{n0}, which do not satisfy (4.22) to (4.24) at all, were excited, very unstable solutions has been observed shortly after the numerical wave reached the boundary.

The modified absorbing boundary conditions for the 3D TLM symmetrical condensed node In order to reduce the effects of spurious modes at the absorbing boundaries, additional conditions may be introduced in the absorbing conditions. Suppose that there exist a physical mode, expressed by (4.19), and its spurious mode, expressed by (4.20). It is not difficult to see the difference between the physical mode and the forward-propagating spurious mode is in the phase shift with position. The phase shift between two

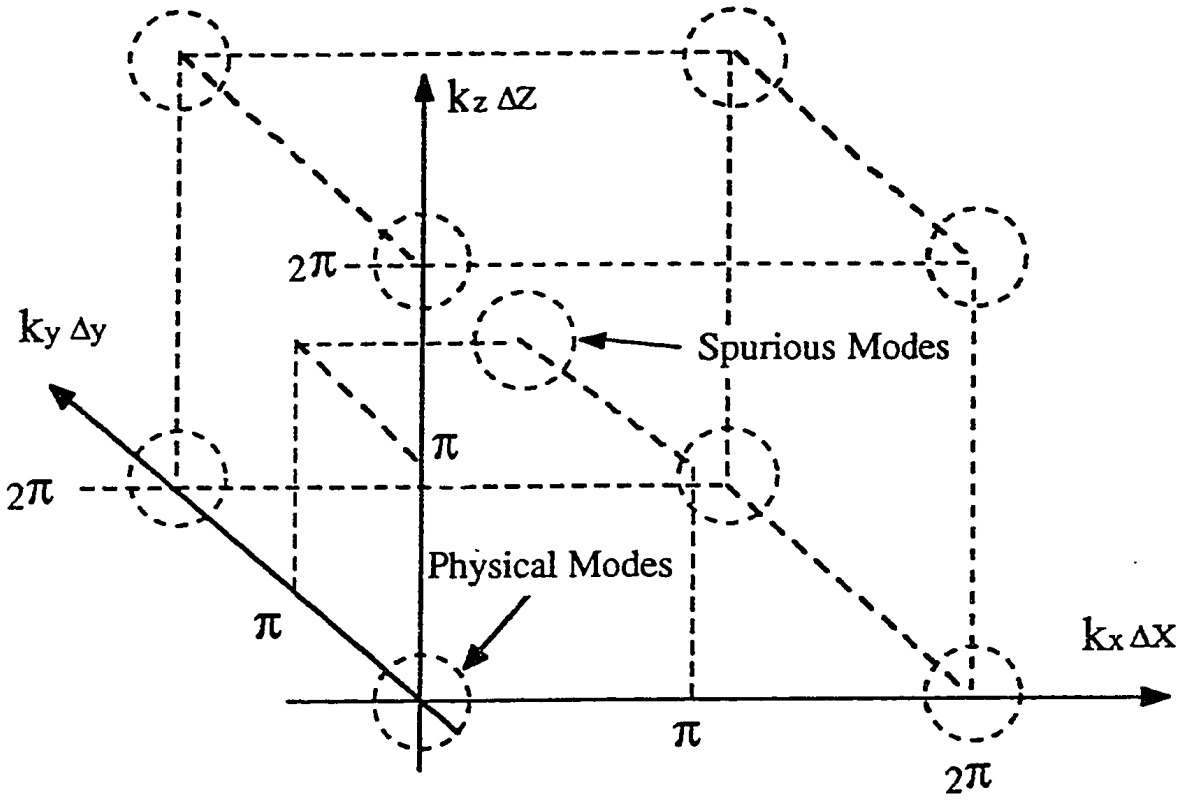

Figure 4.9: Numerical Dispersion Diagram of the 3D TLM SCN

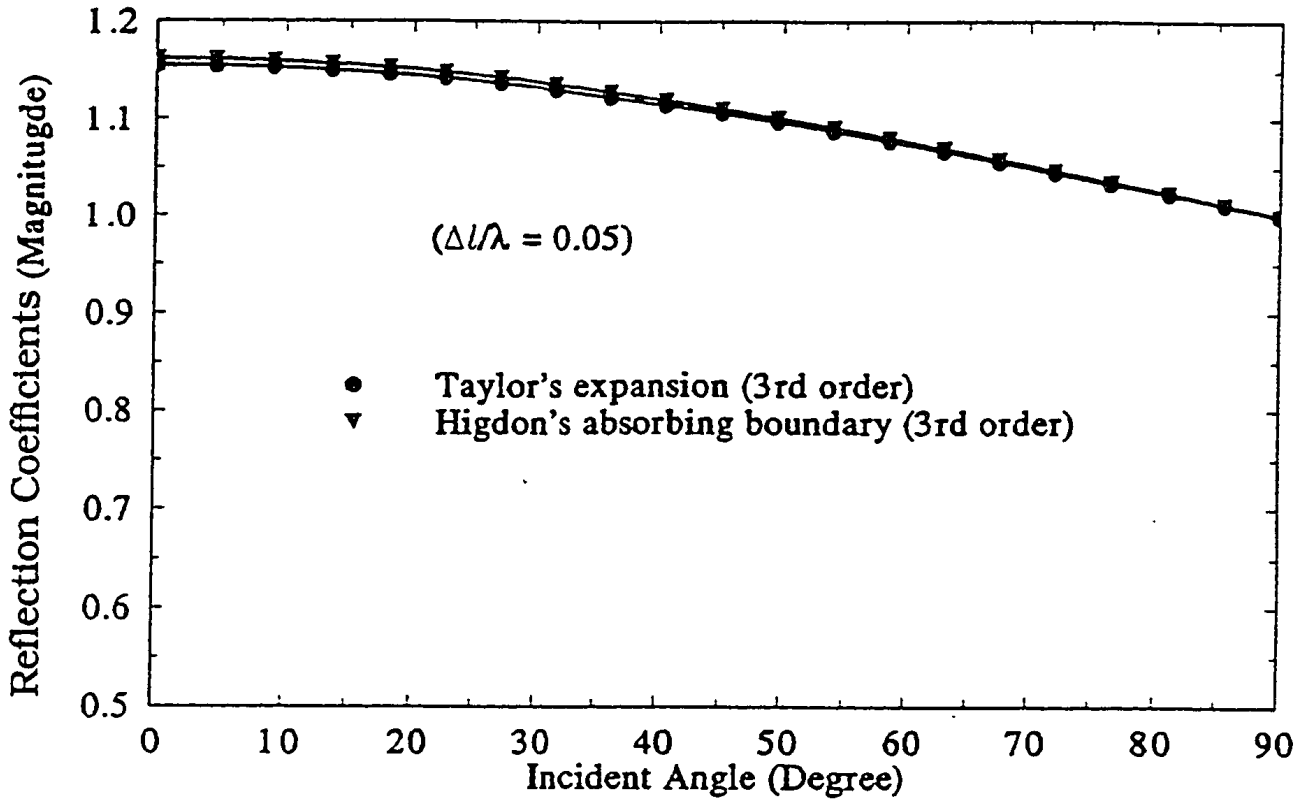

Figure 4.10: Reflection Coefficients of the Absorbing Boundaries for Spurious Modes

neighboring node along $x = const.$ for the physical mode is $k_x \Delta x$, while for the spurious mode is $\overline{k}_x \Delta x = \pi + k_x \Delta x$ which corresponds change of polarity plus the phase shift of the physical mode. Therefore, if an absorbing boundary condition exists for the physical modes as indicated by (4.18):

$$\sum_{i1=0}^{P} \sum_{i2=0}^{P} a_{i1,i2} D_x^{-i1} K^{-2\,i2} \;\; {}_{n+\frac{1}{2}}U^r(0+\frac{1}{2}, i_y, i_z) = 0 \quad a_{0,0} = -1 \tag{4.25}$$

then, the condition:

$$\sum_{i1=0}^{P} \sum_{i2=0}^{P} (-1)^{i1} a_{i1,i2} D_x^{-i1} K^{-2\,i2} \;\; {}_{n+\frac{1}{2}}U^r(0+\frac{1}{2}, i_y, i_z) = 0 \quad a_{0,0} = -1 \tag{4.26}$$

would absorb the forward-propagating spurious mode (${}_{n+\frac{1}{2}}U^r(0+\frac{1}{2}, i_y, i_z)$ is the impulse needed to be injected back into the TLM network form the boundary).

By combining the above two conditions, one can easily obtain the absorbing boundary conditions which can absorb both the physical modes and the spurious modes:

$$(\sum_{i1=0}^{P} \sum_{i2=0}^{P} a_{i1,i2} D_x^{-i1} K^{-2\,i2})(\sum_{i1=0}^{P} \sum_{i2=0}^{P} (-1)^{i1} a_{i1,i2} D_x^{-i1} K^{-2\,i2})_{n+\frac{1}{2}}U^r(0+\frac{1}{2}, i_y, i_z) = 0 \tag{4.27}$$

Fig.4.11, Fig.4.12 and Fig.4.13 show the reflection coefficients and their comparisons of the above absorbing condition for the physical and spurious modes under the assumption that $k_x = k\,cos\theta$ where θ is the incident angle to the absorbing boundaries. A quite good absorption of the absorbing boundaries can be expected for the TLM simulations.

4.4 The Connecting Boundary Conditions for the TLM Simulations

Since the absorbing boundary conditions are valid only for the scattered fields, a connecting boundary, which separates the scattered fields from the total fields, needs to be used, as shown in Fig.4.14 (Note that although there are other ways to deal with the scattering problems [87], this technique can avoid the numerical noises in some situations [91, 92, 93]).

Consider the electromagnetic scattering by an object in Fig.4.14a. For linear problems, the total field can be decomposed into incident and scattered fields. That is,

$$\mathbf{E}^{tot} = \mathbf{E}^{inc} + \mathbf{E}^{sca} \tag{4.28}$$

$$\mathbf{H}^{tot} = \mathbf{H}^{inc} + \mathbf{H}^{sca} \tag{4.29}$$

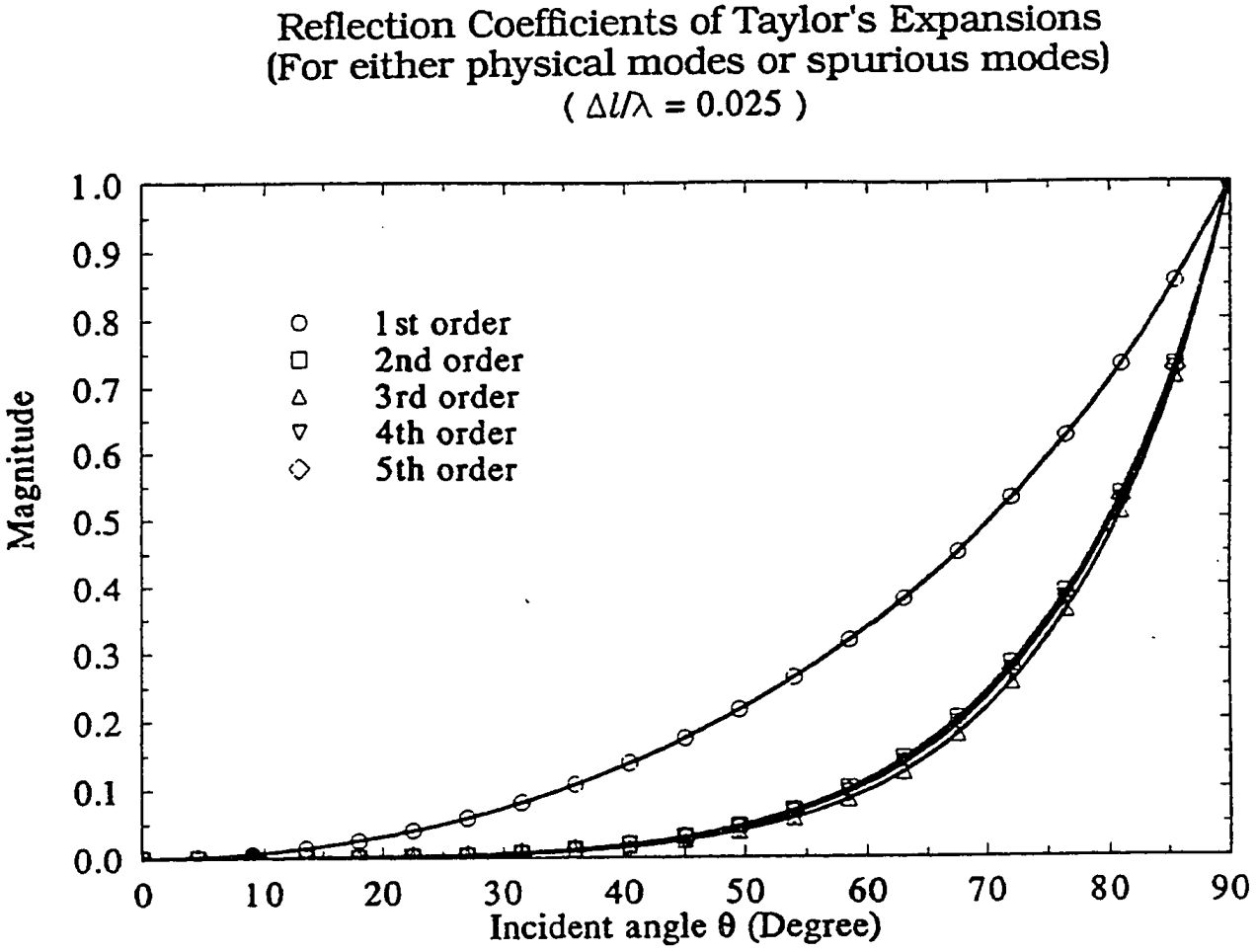

Figure 4.11: Reflection Coefficients of the Modified Taylor's Expansions

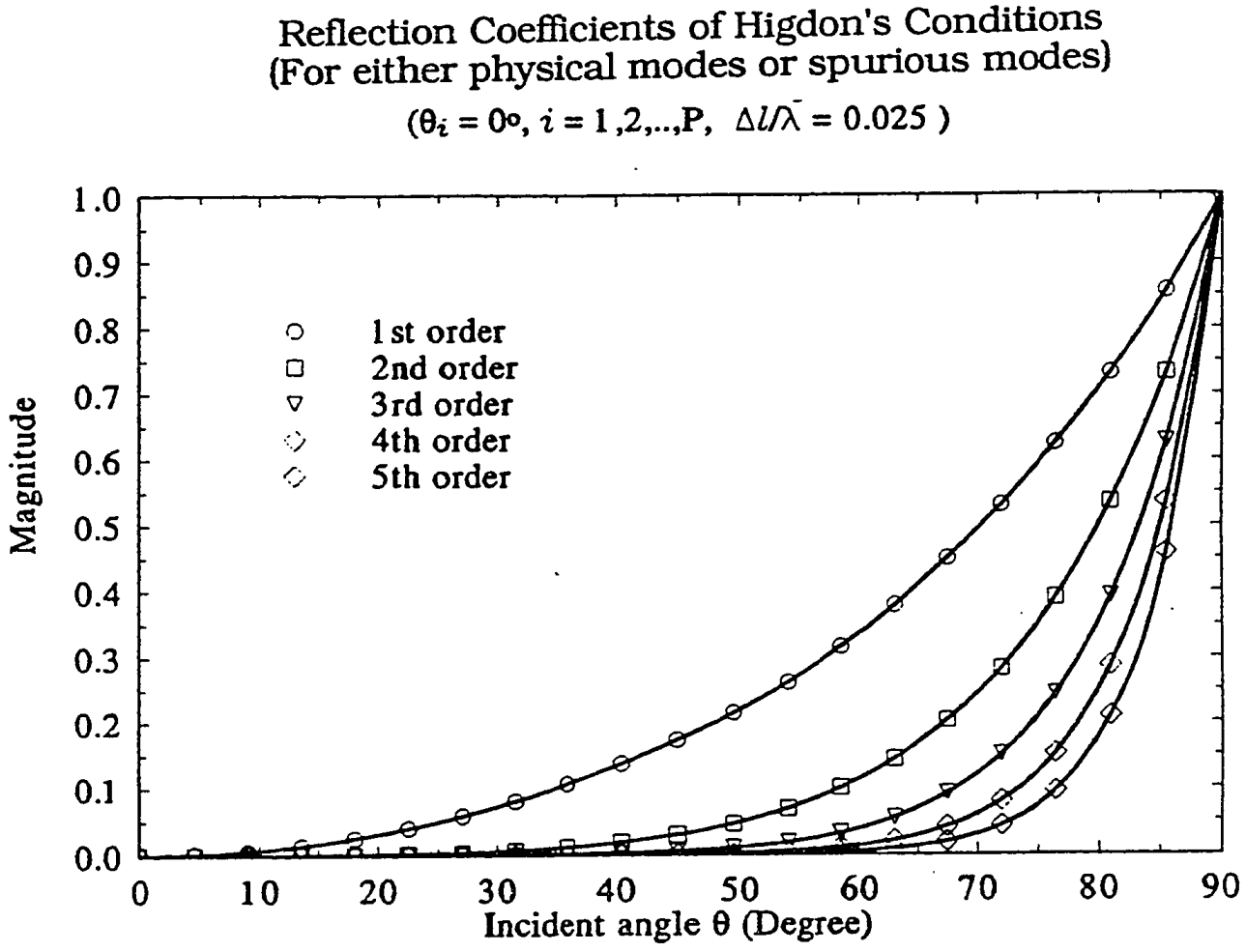

Figure 4.12: Reflection Coefficients of the Modified Higdon's Absorbing Boundaries

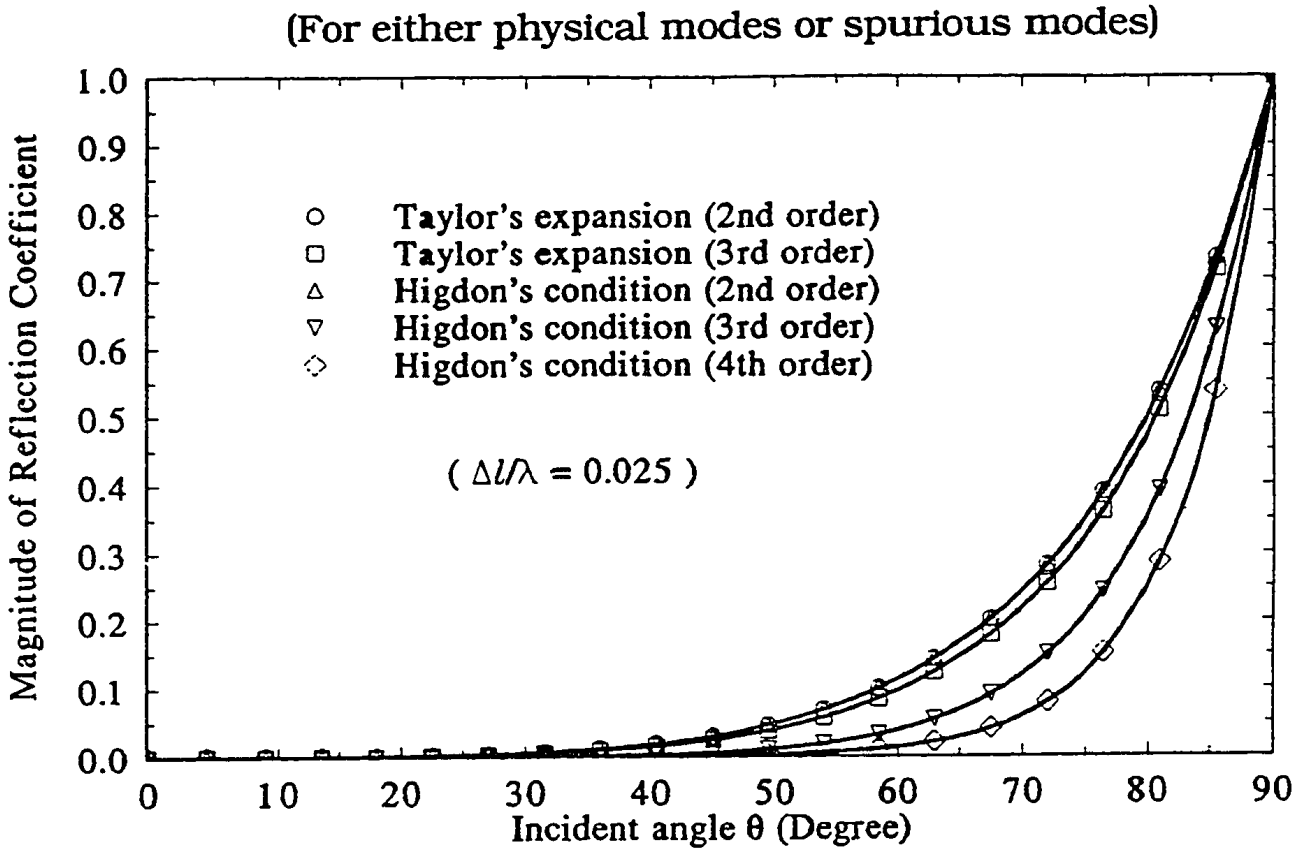

Figure 4.13: Comparisons of Reflection Coefficients of the Modified Absorbing Boundaries

where the incident field $\mathbf{E}^{inc}$ and $\mathbf{H}^{inc}$ are defined to be the fields which exist in the absence of the scatters.

Based on the equivalence principle [95], solving the problem in Fig.4.14a can be switched to solving the problem of Fig.4.14b or Fig.4.14c under the condition that a magnetic current source

$$\mathbf{M_s} = \mathbf{E}^{inc} \times \mathbf{n} \tag{4.30}$$

and an electric current source

$$\mathbf{J_s} = \mathbf{n} \times \mathbf{H}^{inc} \tag{4.31}$$

are applied on the connecting surface (where $\mathbf{n}$ is the inward unit vector of the connecting surface). As a result, an incident field will be produced only inside the connecting surface. When scatterers are present, the field inside the connecting boundary is then the total field and outside the connecting boundary is the scattered field. Note that in this way, absorbing boundary conditions can be applied to the region outside the connecting boundary.

Now, suppose that a connecting boundary is placed between two regions filled with the TLM networks as shown in Fig.4.15.

Assume that

$$\mathbf{M_s} = M_y \mathbf{a_y} + M_z \mathbf{a_z} \tag{4.32}$$

$$\mathbf{J_s} = J_y \mathbf{a_y} + J_z \mathbf{a_z} \tag{4.33}$$

which are usually known analytically via (4.30) and (4.31).

Then, according to the equivalence shown in Chapter 2,

$$-M_y = E_{z1} - E_{z2} \equiv ({}^1V_{10}^r + {}^1V_{10}^i) - ({}^2V_6^r + {}^2V_6^i) \tag{4.34}$$

$$-J_z = H_{y1} - H_{y2} \equiv ({}^1V_{10}^r - {}^1V_{10}^i)/Z_0 - ({}^2V_6^i - {}^2V_6^r)/Z_0 \tag{4.35}$$

and

$$M_z = E_{y1} - E_{y2} \equiv ({}^1V_{11}^r + {}^1V_{11}^i) - ({}^2V_3^r + {}^2V_3^i) \tag{4.36}$$

$$J_y = H_{z1} - H_{z2} \equiv ({}^1V_{11}^i - {}^1V_{11}^r)/Z_0 - ({}^2V_3^r - {}^2V_3^i)/Z_0 \tag{4.37}$$

which lead to the connecting boundary conditions:

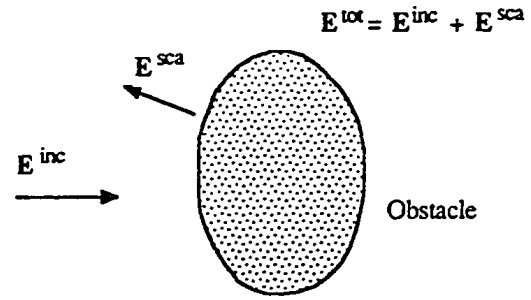

(a) The original problem

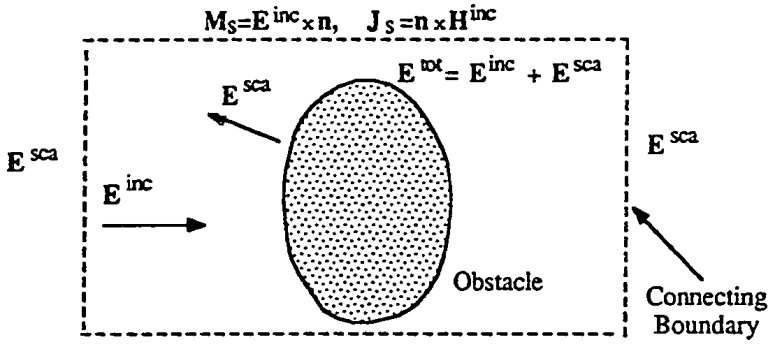

(b) The equivalent problem

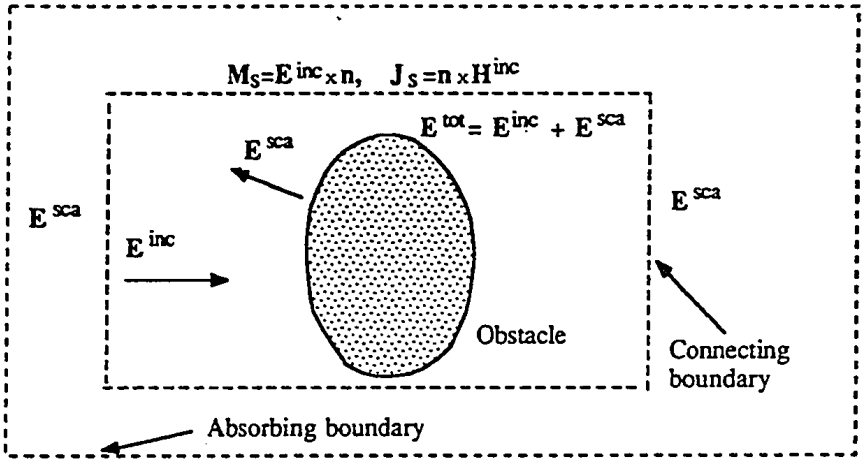

(c) The equivalent problem with absorbing boundaries

Figure 4.14: **An Obstacle Illuminated by an Electromagnetic Wave**

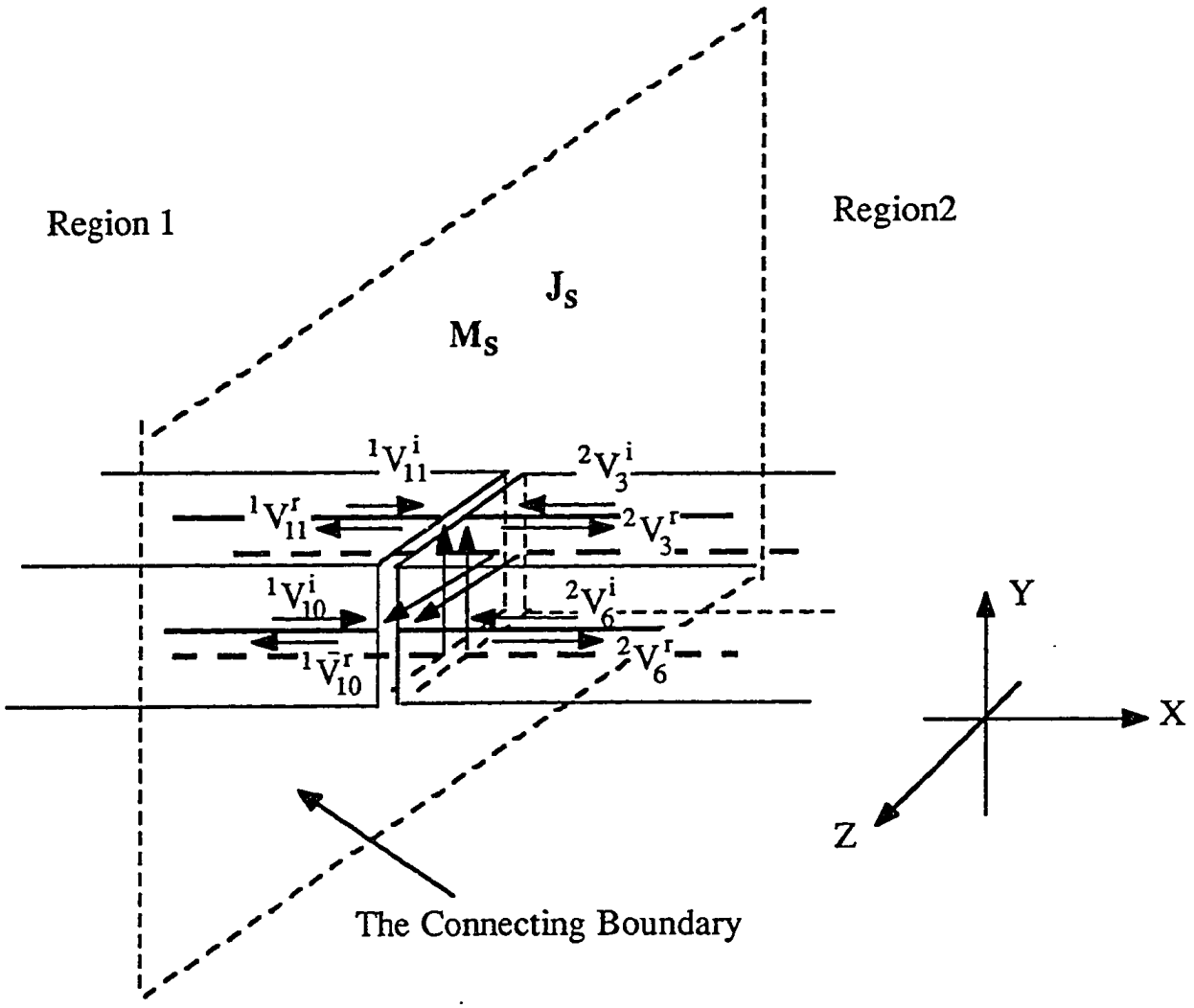

Figure 4.15: **A Connecting Boundary Placed in Between two TLM regions**

$$
\begin{aligned}
{}^1V_{10}^r &= -\frac{1}{2}\left(M_y + Z_0\, J_z\right) + {}^2V_6^i && (4.38)\\
{}^2V_6^r &= \frac{1}{2}\left(M_y - Z_0\, J_z\right) + {}^1V_{10}^i && (4.39)\\
{}^1V_{11}^r &= \frac{1}{2}\left(M_z - Z_0\, J_y\right) + {}^2V_3^i && (4.40)\\
{}^2V_3^r &= -\frac{1}{2}\left(M_z + Z_0\, J_y\right) + {}^1V_{11}^i && (4.41)
\end{aligned}
$$

where ${}^1V_{10}^i$, ${}^1V_{10}^r$, ${}^1V_{11}^i$, ${}^1V_{11}^r$, ${}^2V_6^i$, ${}^2V_6^r$, ${}^2V_3^i$, and ${}^2V_3^r$ are the impulses incident and reflected at the interface from Region 1 and 2 as shown in Fig.4.15.

The above equations accomplish arbitrary excitations (which are usually expressed analytically) for TLM simulations of scattering problems while allowing absorbing boundaries to be applied outside the connecting boundary. In practical numerical simulations, in order to reduce numerical noises generated in the TLM model, it is necessary to use the low-frequency band limited signals or excitations as the incident fields. The reason is that the incident fields are usually computed and are imposed on the connecting boundary as equivalent currents in an analytical way. In consequence, they always travel at the constant speed (speed of light) no matter what frequencies they carry with. However, the scattered fields, which are generated with the TLM simulations, travel at lower speeds with higher frequencies due to the numerical dispersion of the TLM model. Thus, if high frequency incident wave is excited, the slower traveling speeds of scattered waves may cause time delay for the scattered waves to reach some points; as a result, the numerical noises are generated. For example, in the shadow regions, the scattered fields are supposed to reach the regions at the same time as the incident waves. In this way, the scattered fields can almost cancel the incident field, resulting in the almost zero field regions. However, this may not happen in the practical numerical simulations due to the late arrivals of the scattered wave, leading to nonzero fields in the shadow regions with quite amount of numerical noises.

4.5 Validations of the Absorbing and Connecting - Boundary Conditions for the TLM Simulations

Validations of the absorbing and connecting boundary conditions have been done with the 2D TLM shunt node and the 3D TLM symmetrical condensed node.

To the author's point of view, The best way to validate a numerical time-domain technique is in frequency-domain rather than in time-time. The reason is that any numerical model is not valid at high frequencies because of its finite discretization in space and time. In addition, different numerical models exhibit different dispersions in high-frequency range. Therefore, they may display different results for high-frequency components, which are reflected by different solutions in time-domain. On the other hand, all the models are constructed to be correct for low-frequency modeling. Therefore, validations of these models had better be carried out in frequency-domain for low-frequency components rather than in time-domain. The principle also applies to validations of interfacing of different models which are all correct for low-frequency modeling. In this sense, the validations of the absorbing boundary conditions, which are developed on the different bases from that for the TLM models, should be done in frequency domain.

4.5.1 Numerical measurement of reflections of the absorbing boundaries in rectangular waveguides

The best way to examine the quality of the absorbing boundaries is to numerically calculate the reflection coefficients in the TLM simulations. A section of WR28 rectangular waveguide was chosen for this purpose since the waves in a rectangular waveguide can be considered as a superposition of many plane waves with different incident angles. Therefore, behavior of the wide angle absorption of the absorbing boundaries can be observed. The simulation was performed with a TLM network of the 2D shunt node network and a TLM network of the 3D symmetrical condensed nodes (Fig.4.16), respectively. Both ends of the waveguide were terminated with the absorbing boundaries. The VSWR in the waveguide is computed directly and numerically with the ratio of V_{max} over V_{min} (where V is the amplitude of the dominant mode in the waveguide). Fig.4.17 and Fig.4.18 show the return losses in the simulations.

It can be seen that both Higdon's conditions and Taylor's expansion posses very good absorption over operating frequency range of WR28, with return loss better than -35dB for both 2D and 3D cases.

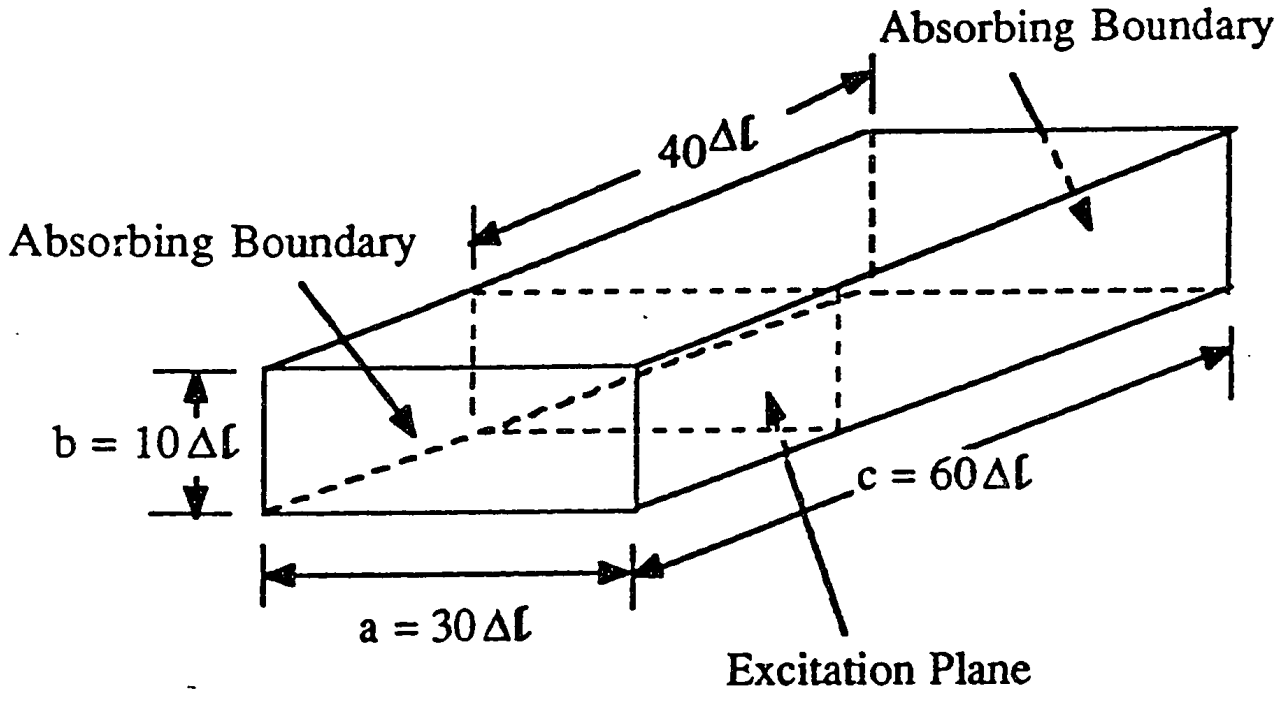

Figure 4.16: A Section of WR28 Rectangular Waveguide with Both Ends Terminated with the Absorbing Boundaries

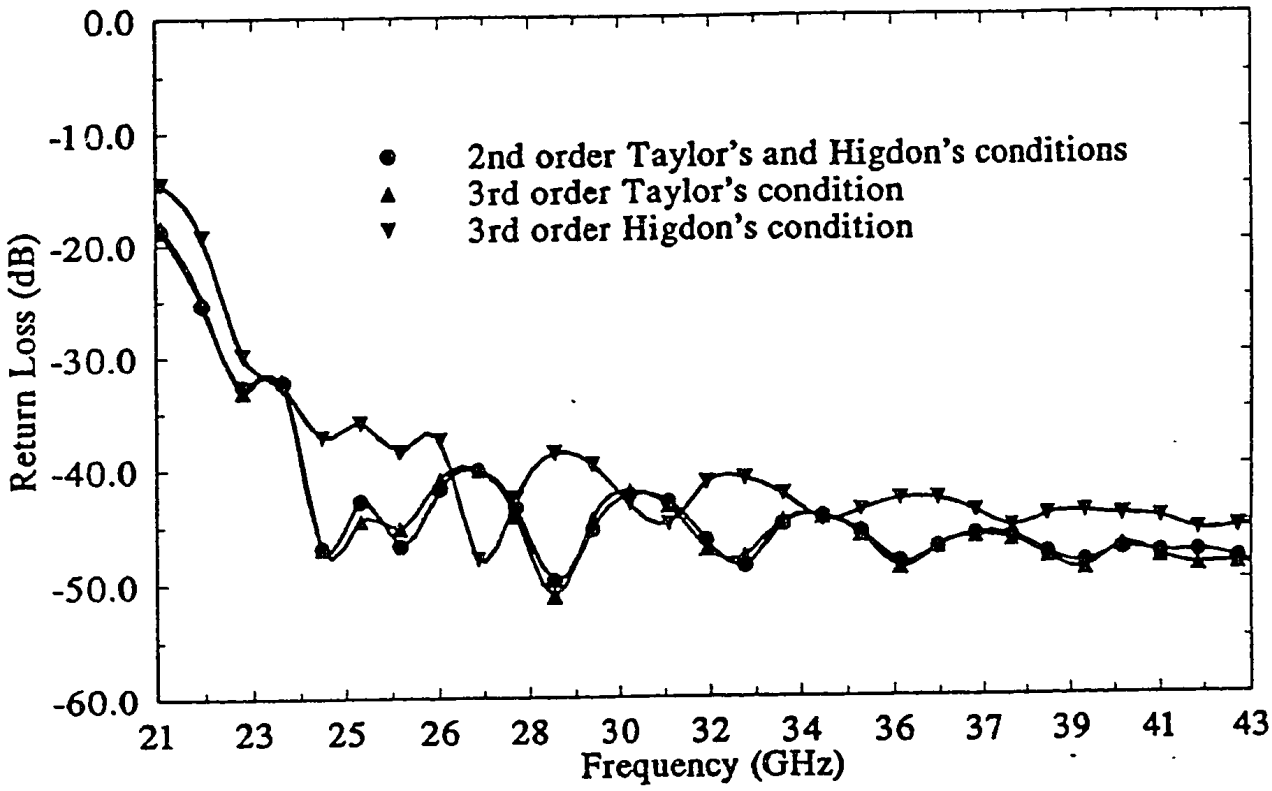

Figure 4.17: Return Loss in the Rectangular Waveguide with the 2D Simulations

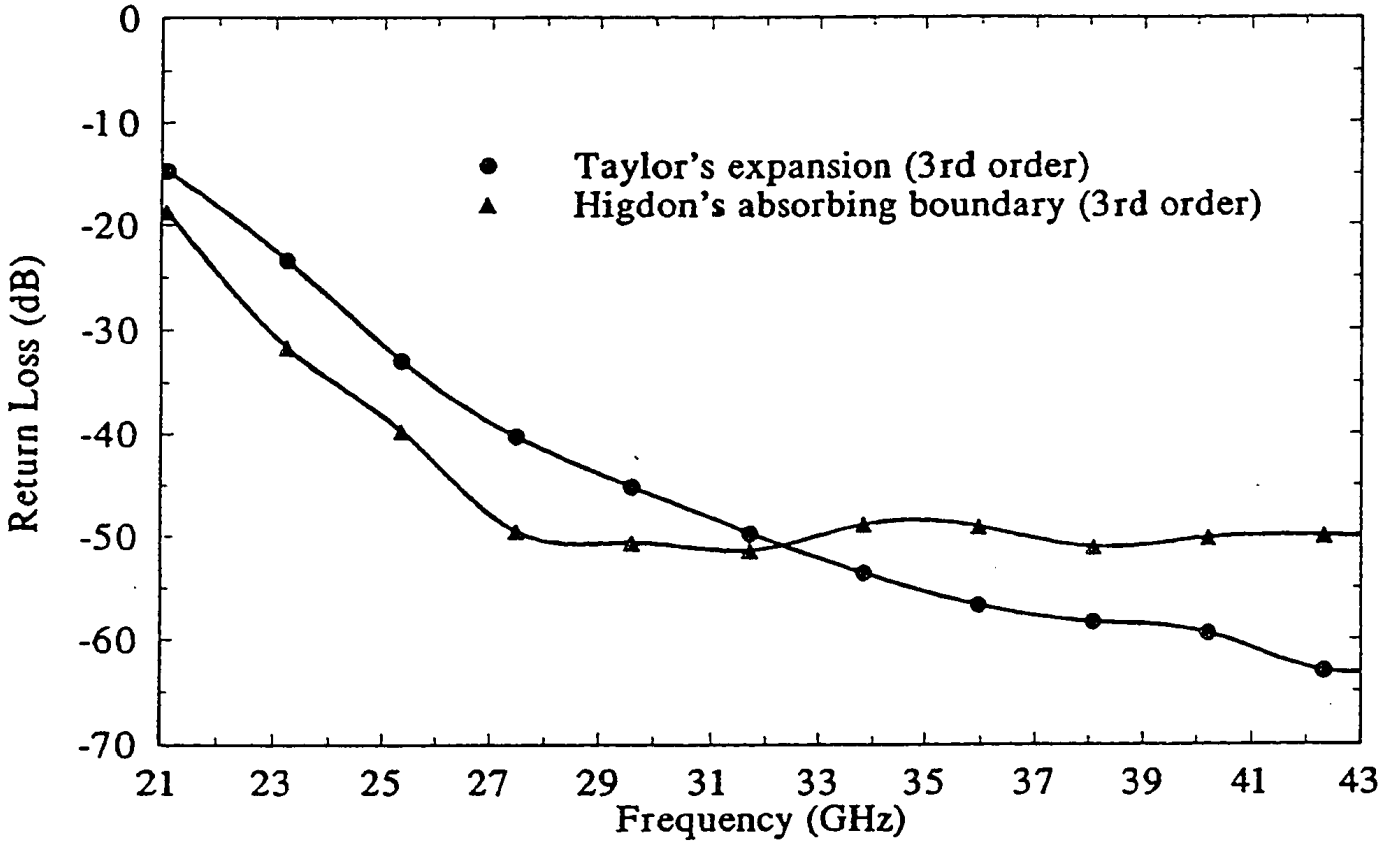

Figure 4.18: **Return Loss in the Rectangular Waveguide with the 3D Simulations**

4.5.2 Validations of the absorbing and connecting boundary conditions with scattering problems

Two-dimensions Fig.4.19 models a 0.1 wavelength thick conducting screen which extends 0.5 wavelength to each side of a straight slot having a gap of 0.025 wavelength. Broadside TE illumination is assumed. Two types of predictive data are compared: (1) the high-resolution (0.025 λ_o) TLM model treating the slot as a 1-cell gap; the absorbing boundaries are placed uniformly 15 cell away from the conducting sheet; (2) a very-high resolution frequency-domain EFIE model, solved via MOM (having 0.0025 λ_o sampling in the slot), which treats the slotted screen as a pure scattering geometry [94]. From Fig.4.20 one can see that there is good agreement between the two sets of results in both magnitude and phase. It shows that the absorbing and connecting boundary conditions work well for the two-dimensional TLM simulations.

three-dimensions Consider a metal cube (Fig.4.21), with electrical size $k_o s = 2$, subject to plane-wave illumination at broadside incidence. s is the side width of the cube. Results shown in Fig.4.22 are for the TLM (SCN) simulation and a frequency-domain surface EFIE using a standard triangular surface-patching MOM code [93]. For the TLM model, each face of the cube is spanned by 144 square cells (12x12), and the absorbing boundary is again located at a uniform distance of 15 cells from the cube surface. For the MOM model, each face of the cube is spanned by 32 triangular patches. Comparative results for the surface current are graphed along a straight line loci along the cube: $\overline{abcd}$, which is the plane of the incident electric field. The surface currents were obtained with $\mathbf{n} \times \mathbf{H}$ on the metal surface, where $\mathbf{H}$ is equivalent to the currents in the TLM models as indicated in Chapter II and $\mathbf{n}$ is the outward normal unit vector. A very high degree of correspondence exists between the two sets of results, which again shows the good performance of the absorbing and connecting boundary conditions developed.

Instabilities of the absorbing boundaries Numerical experience has shown that the unstable solutions may still occur due to the variable reasons as described in the following:

A. The absorbing boundaries too close to the source;

Since the most of absorbing conditions are derived under the assumption that the wave are traveling or propagating, they may amplify, instead of 'absorb', the non-propagating

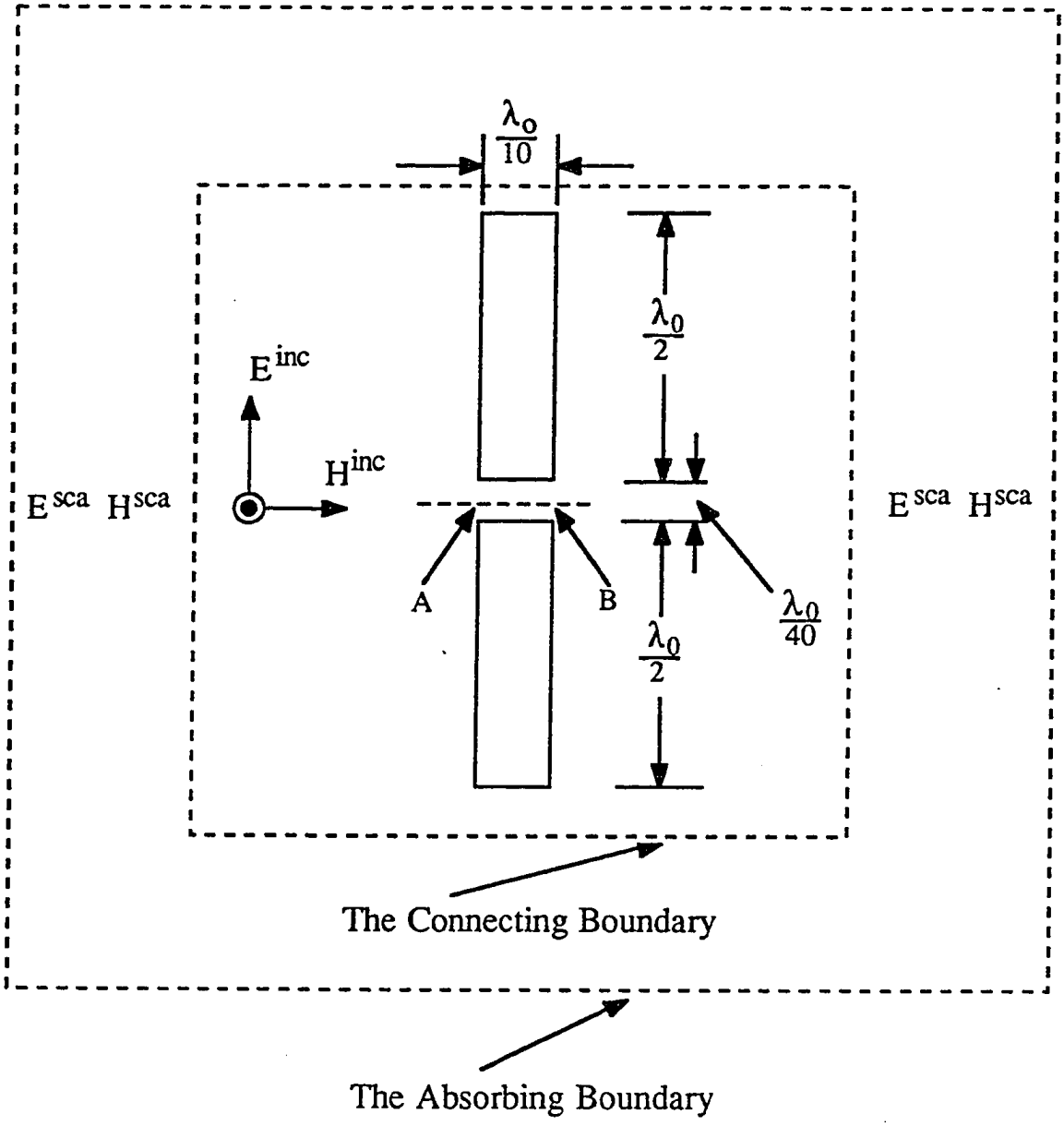

Figure 4.19: **A Straight Slotted Conducting Screen**

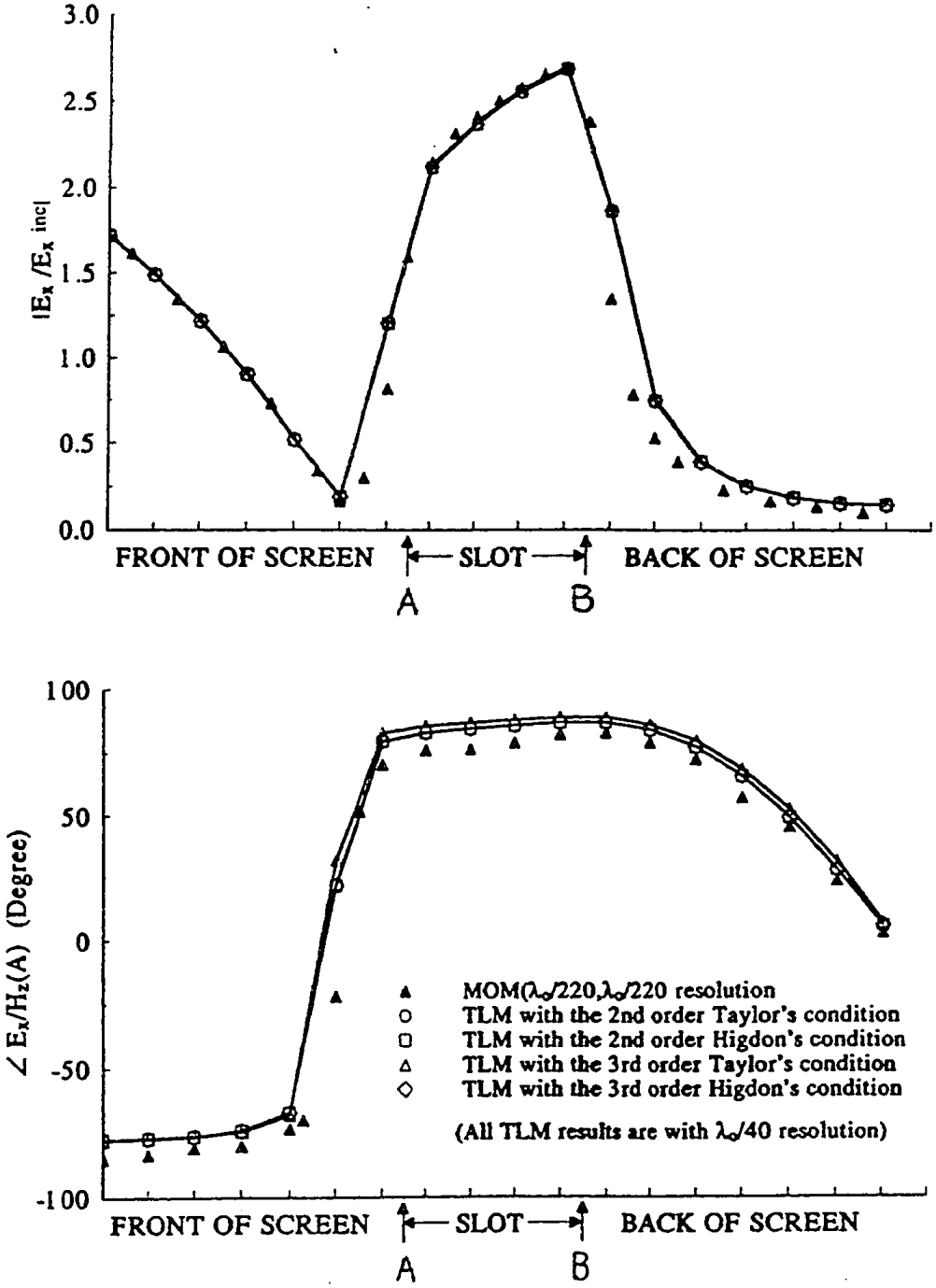

Figure 4.20: **Comparison of the TLM and Frequency-domain Surface EFIE Results for the Gap Electric Field Distribution in the Slotted Screen**

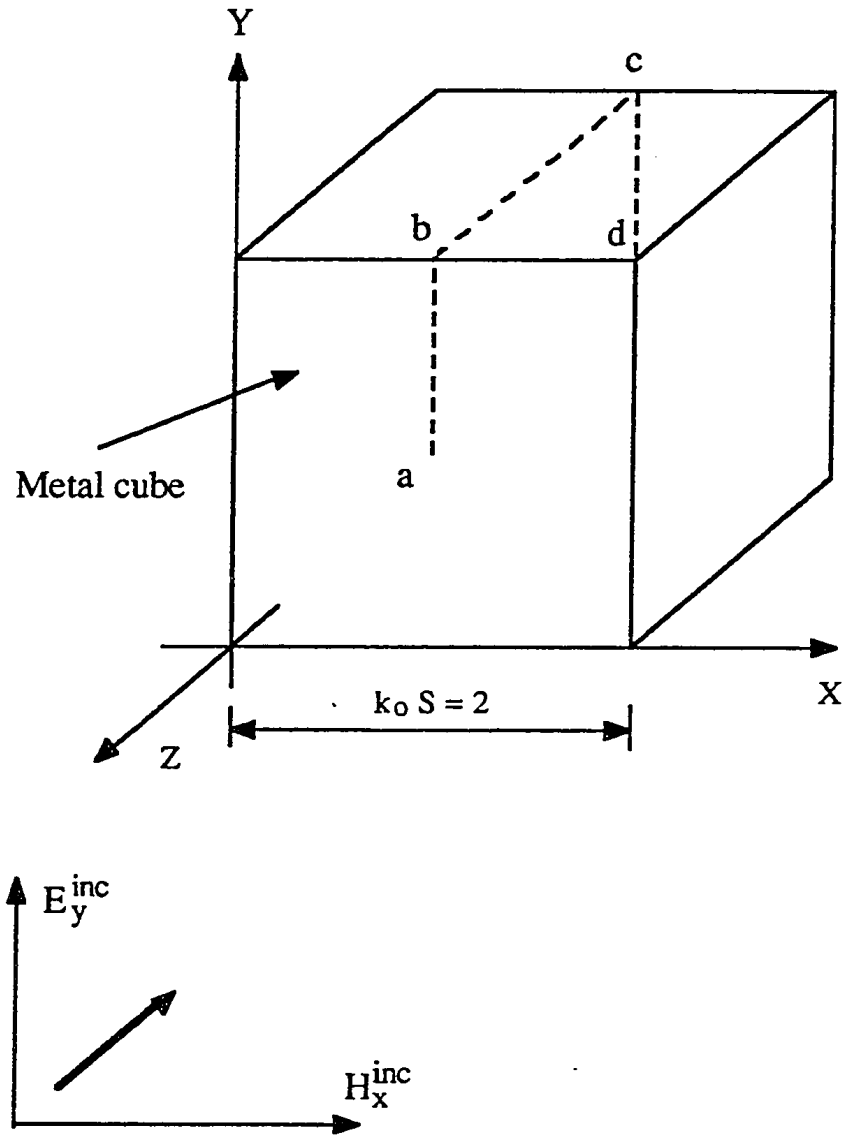

Figure 4.21: A Metal Cube illuminated by a Plane wave

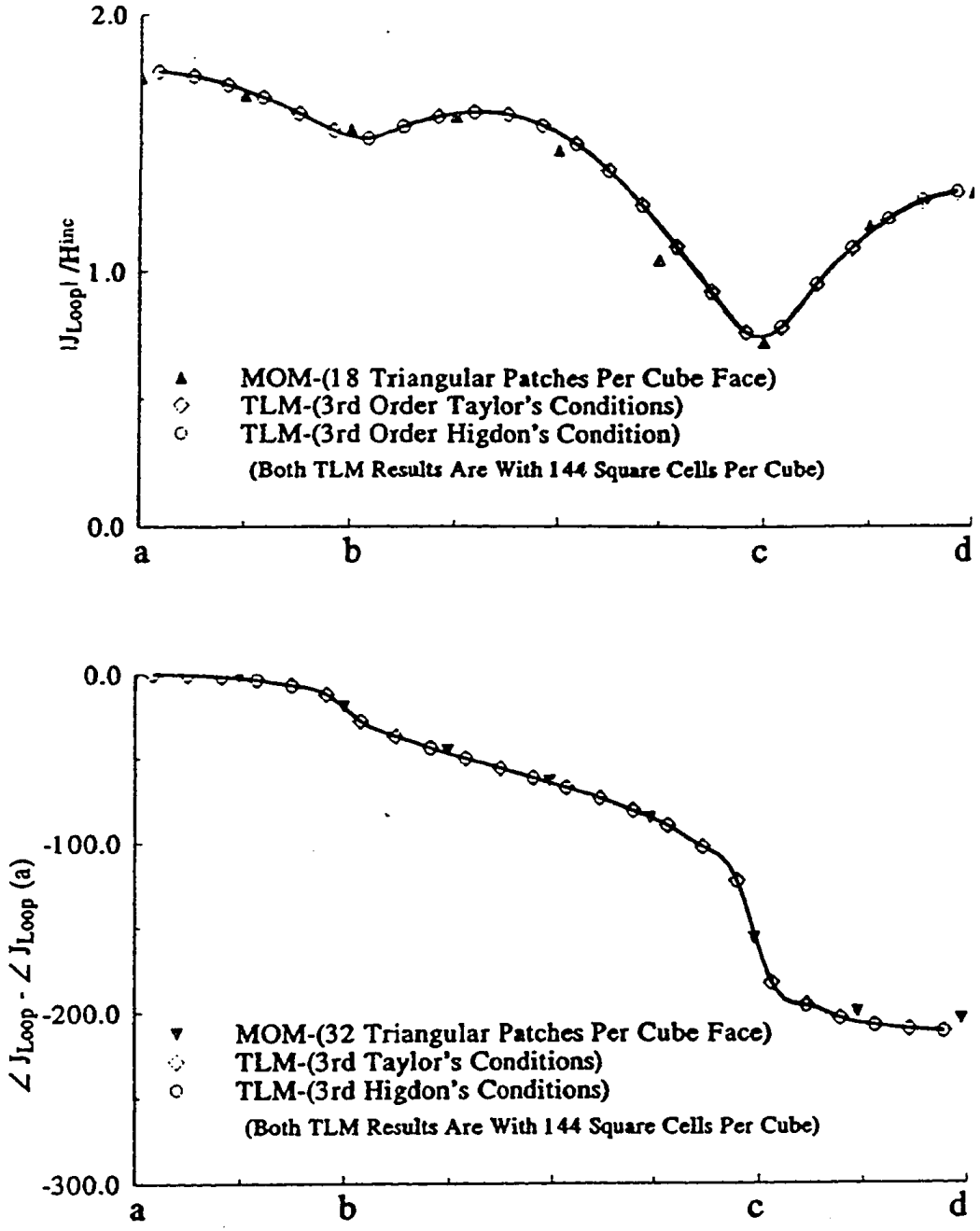

Figure 4.22: Comparison of TLM and MOM Results for the Surface Currents on the Metal Cube

waves which are usually present around the regions with sources and discontinuities. Therefore, it is suggested that the absorbing boundaries be placed at 10 to 15 cells from sources and discontinuities in both 2D and 3D TLM simulations.

B. The numerical noises;

Due to the roundoff and truncation errors of the computer simulations, the uncorrelated numerical noises will be present and become dominant components in computation domains, after the major energy of electromagnetic waves pass through the absorbing boundaries. Since most of absorbing boundary conditions are derived on the basis of physical correlated wave propagation, the instability may occur when the numerical noises become dominant and are processed at the boundaries. To overcome this problem or delay the instability, two techniques has been employed in this thesis: 1) use a frequency-band limited excitation, which reduce the high temporal frequency components in the simulations; 2) terminate the simulations or switch to other boundary conditions such as lossy boundary conditions after the main waves pass the absorbing boundaries.

C. The orders of the absorbing boundaries too high;

Since the TLM models are usually accurate with second (or a bit higher) order finite-difference, the high orders of finite-differences, which are required with the high order absorbing boundaries, may not be correctly computed in numerical simulations. Hence, inaccurate calculations result, leading to unstable solutions. From numerical experience, it is recommended that up to the fifth order of absorbing boundaries be applied for the 2D TLM simulations, and the third order for the 3D TLM simulations.

4.6 Conclusion

In this chapter, the absorbing boundary and connecting boundary conditions have been studied and developed for the 2D and 3D TLM simulations. Qualities of the absorbing boundaries has been examined and validations of both absorbing and connecting boundaries were obtained with the scattering problems of two-dimensions and three-dimensions. A high degree of agreements between the TLM simulation results and the MOM solutions was presented.

Chapter 5

A New Procedure For Interfacing The TLM Method With Frequency-Domain Solutions

5.1 Introduction

The Transmission Line Matrix method (TLM) has been extensively applied to solve electromagnetic wave propagation, diffusion and network problems in the time-domain. With its flexibility and simplicity of the basic algorithm, TLM can handle arbitrary geometries and account for realistic features that are often neglected with other methods. Most published work on the application of TLM techniques has been devoted to the computation of specific structures, modeling of various types of boundaries, material parameters, implementation of graded meshes and the development of improved nodes. Recently, two and 3D transmission line matrix microwave field simulators using new concepts and procedures were presented [29].

In order to characterize structures with large dimensions, the TLM technique requires large memory space and CPU time. More recently, a general partitioning technique based on the Johns matrix concept [21, 22, 26, 27] was developed to overcome this problem, thus considerably expanding the application range of the TLM.

In the following, a new procedure for interfacing TLM techniques with frequency-domain solutions is described: either scattering parameters or the relations between electric and magnetic fields on a boundary or interface limiting regions, computed in the frequency domain, are transformed into time-domain sequences. The sequences of impulses are equivalent to the ones that would produce a corresponding Johns Matrix, describing subregions

for TLM simulations [26]. The subsequent step is to convolve any impulse stream incident upon such a boundary with the time domain sequences or Johns Matrix hence generated. A considerable reduction in computation time has been observed in generating Johns Matrix.

5.2 Basic Theory

Let $X(f)$ be a frequency-domain solution, for example, a frequency dependent complex reflection coefficient, and $x(t)$ the corresponding time-domain solution. Then by sampling or discretizing $X(f)$, one can obtain the corresponding discrete $x(t)$ via various synthesis techniques. For the sake of simplicity, the discrete Fourier Transform (DFT) technique is employed in this paper.

The discrete and the inverse discrete Fourier transforms are [96]:

$$X_k = \sum_{i=0}^{N-1} x_i e^{jik\frac{2\pi}{N}} \qquad k = 0, 1, 2, ..., N-1 \tag{5.1}$$

$$x_k = \frac{1}{N} \sum_{i=0}^{N-1} X_i e^{-jik\frac{2\pi}{N}} \qquad k = 0, 1, 2, ..., N-1 \tag{5.2}$$

where j is the complex operator ($j = \sqrt{-1}$) , and

$$X_k = X(k\,\Delta f), \tag{5.3}$$

$$x_k = x(k\,\Delta t) = \frac{1}{N} \sum_{i=0}^{N-1} X_i e^{-jik\frac{2\pi}{N}} \tag{5.4}$$

N is the total number of iterations of the time domain solution or the total number of sampling points of the frequency domain solution, $\Delta f = \frac{1}{N\,\Delta t}$ is the sampling frequency and Δt is the time step determined by the TLM model.

TLM simulations require that any time-domain solution be real. Therefore, in order to make x_k compatible with the TLM , x_k must be real. As a result, X_k must satisfy the following conditions [96]:

$$Re\ (X_{N-k}) = Re\ (X_k) \tag{5.5}$$

$$Im\ (X_{N-k}) = -Im\ (X_k) \tag{5.6}$$

where k=1,2,...,(N/2)-1 when N is even and k=1,2,...,(N-1)/2 when N is odd.

Consequently, before computing $x(k\Delta t)$ from $X(k\Delta f)$ via (5.4), one should modify $X(f)$ or $X(k\,\Delta f)$ so that (5.5) and (5.6) are fulfilled. As shown in Fig.5.1 and Fig.5.2, the modified $X(f)$ or $X(k\,\Delta f)$ are the same as the original $X(f)$ or $X(k\,\Delta f)$ at least for $f \leq (\frac{N}{2} - 1)\,\Delta f$ when N is even, or $f \leq \frac{N-1}{2}\,\Delta f$ when N is odd. On the other hand, as indicated in [67], the dispersion due to the space and time discretization of TLM networks can be neglected only when the operating frequency f is below a certain value, say f_{max}. For example, in 2-D shunt node TLM models, it is customary to select $\Delta l/\lambda \leq 0.1$ or $f \leq f_{max} = 0.1c/\Delta l$ (c is the speed of light) as the practically dispersionless frequency range in free space. It means that the TLM solution can only be accurate for $f \leq f_{max}$. Thus, N or Δf should be chosen in such a way that

$$(\frac{N}{2} - 1)\,\Delta f \;\geq\; f_{max} \quad when\ N\ is\ even \tag{5.7}$$

$$(\frac{N-1}{2} - 1)\,\Delta f \;\geq\; f_{max} \quad when\ N\ is\ odd \tag{5.8}$$

This ensures that the frequency at which the discrete spectrum is modified to fulfill conditions (5.5) and (5.6) is beyond the frequency limit up to which the TLM solution is accurate. In addition, one can use a low-pass digital filter in order to reject the unwanted high frequency components of the time-domain sequence x_k before it can be convolved with the incident sequence. This is simply achieved by doing the convolution of the $x'_k s$ with the non-causal discrete impulse response of the appropriate low-pass filter.

5.3 Johns Matrix Generation of a Microwave Network

Consider a M-port network, as shown in Fig.5.3, with its given frequency domain scattering parameters $[S(f)]$. Then, the Johns Matrix can be obtained from (5.3) and (5.4):

$$G(n,m,k) = \frac{1}{N}\sum_{i=0}^{N-1} S_{nm}(i\,\Delta f)\mathrm{e}^{-jik\,\Delta f} \tag{5.9}$$

where $m,n = 1,2,...,M$, N is the number of iterations, and $\Delta f = \frac{1}{N\,\Delta t}$ is the sampling frequency. In addition, according to (5.5) and (5.6) , $S_{nm}(f)$ must be modified so that:

$$Re\ S_{nm}((N-i)\,\Delta f) \;=\; Re\ S_{nm}(i\,\Delta f) \tag{5.10}$$

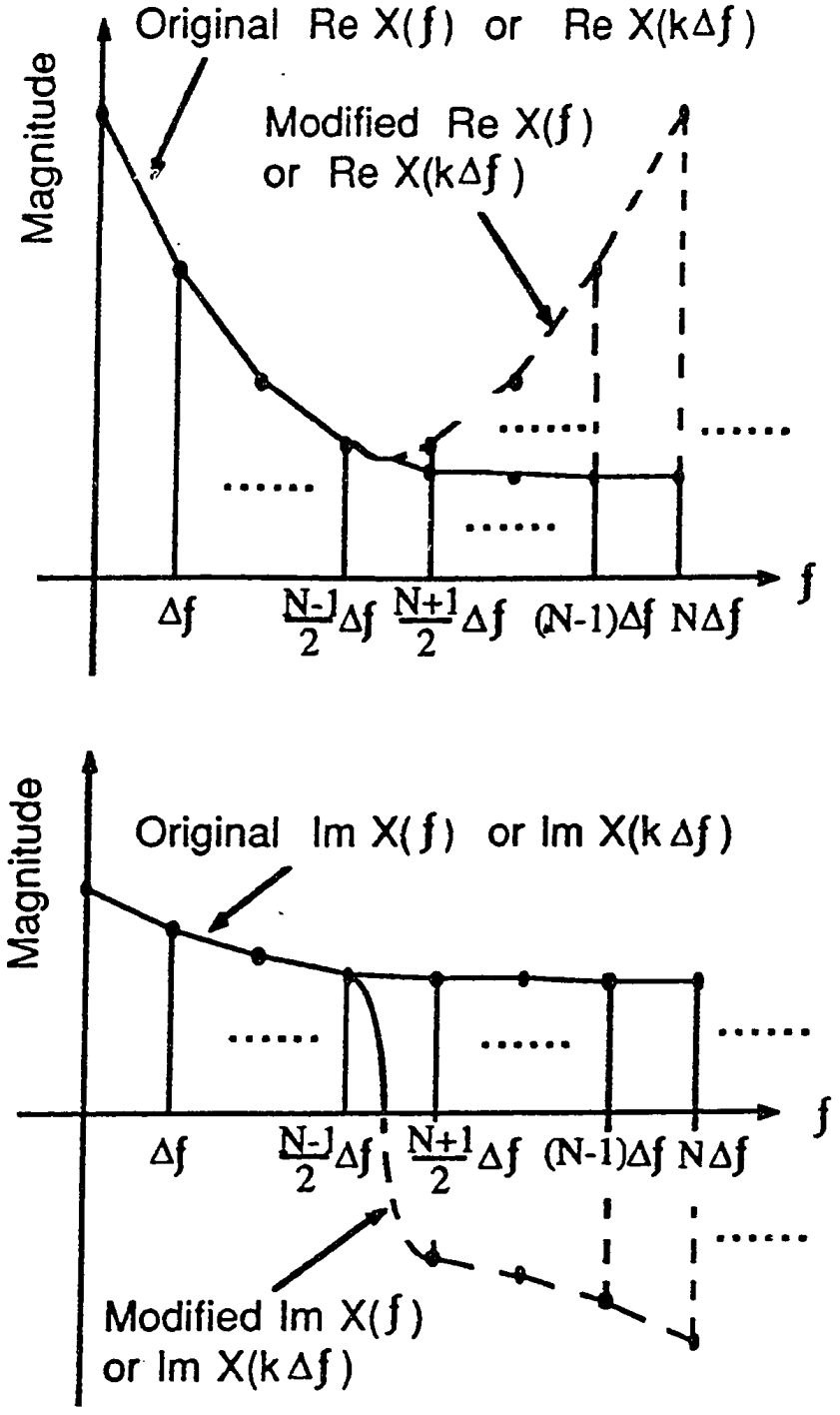

Figure 5.1: The Original and Modified $X(f)$ or $X(k\,\Delta f)$ when N is odd

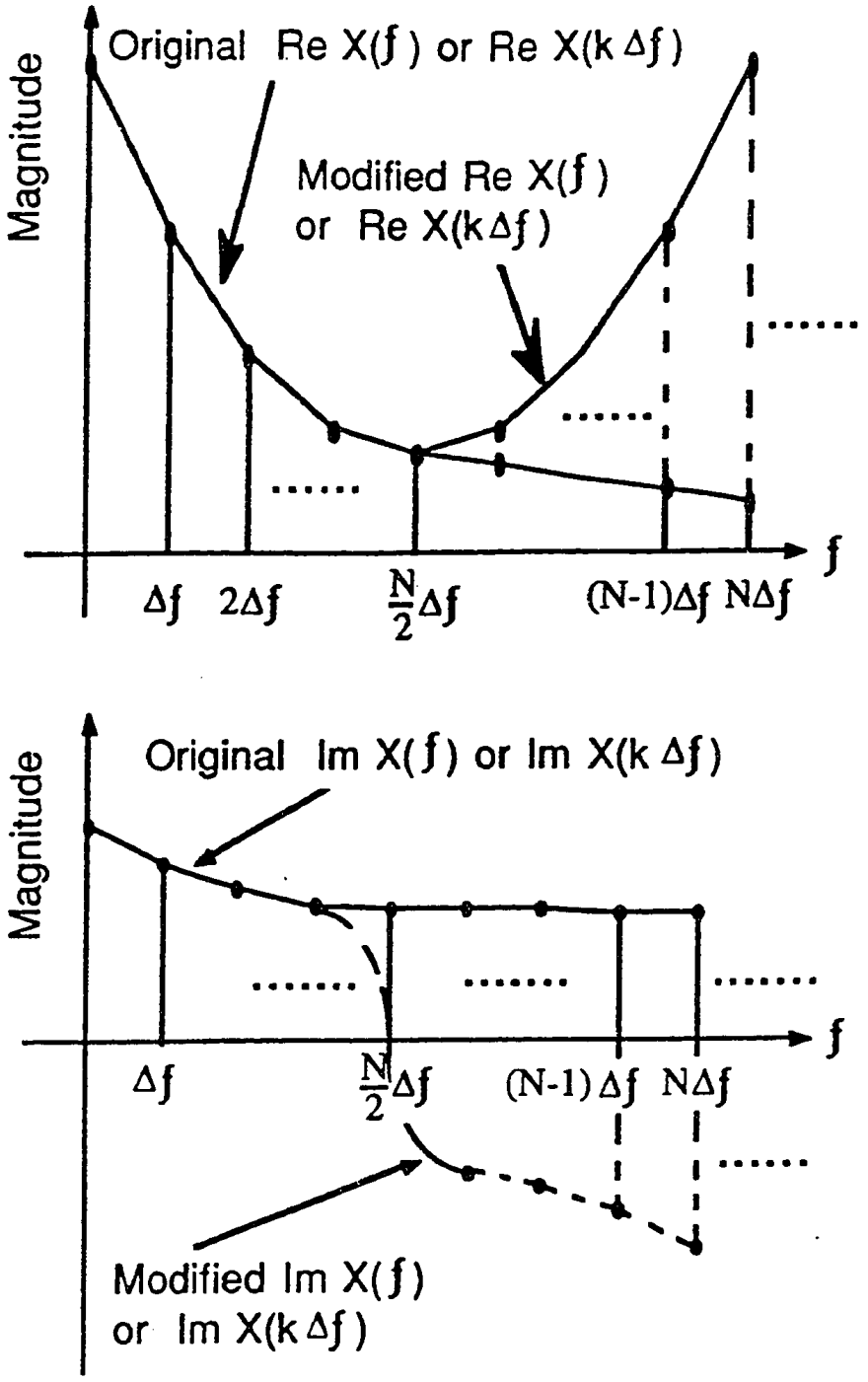

Figure 5.2: The Original and Modified $X(f)$ or $X(k\,\Delta f)$ when N is even

$$Im\ S_{nm}((N-i)\,\Delta f) \;=\; -Im\ S_{nm}(i\,\Delta f) \tag{5.11}$$

Finally, the output sequence of $V^r(n,k)$ at port n is obtained by convolution of the Johns Matrix, generated via (5.9), with the incident impulse, $V^i(m,k')$, at every port:

$$V^r(n,k) = \sum_{m=0}^{M} \sum_{k'=0}^{N} G(n,m,k-k')\, V^i(m,k') \tag{5.12}$$

Once the Johns matrices of several networks are known, the cascading of the networks in time domain can be performed using Bewley diagram which is described in detail by Hoefer [26].

The method described here saves considerable computation time and memory especially when the frequency-domain scattering parameters of the network at the sampling points can be expressed analytically or obtained by measurements. For instance, the application of TLM to describe electromagnetic field diffusion through a highly conducting sheet with a certain thickness is almost impossible, since the high conductivity requires the use of many nodes exhausting the computer resource. However, if the frequency-domain scattering parameters of highly conducting materials can be determined easily for a given geometry, then the corresponding Johns matrix can be obtained by using the above technique. Moreover, it is worth to mention that the procedure is not restricted to two-dimensional TLM problems. The principle of the method is general and can be easily extended to a variety of electromagnetic problems such as 3D inhomogeneously filled and unbounded structures.

5.4 Numerical Results

5.4.1 Application to wideband absorbing boundaries in waveguides

Due to finite computer resources, the TLM mesh must be limited at some locations where absorbing boundaries, matched loads or arbitrary boundary conditions are inserted in order to simulate the properties of the truncated region. The methods for obtaining TLM wideband absorbing boundaries in waveguides were recently described in a paper by Eswarappa et al., [29]. Two different approaches were employed:

a) modeling of a waveguide termination with gradually increasing loss sections,

b) modeling of a very long uniform waveguide section.

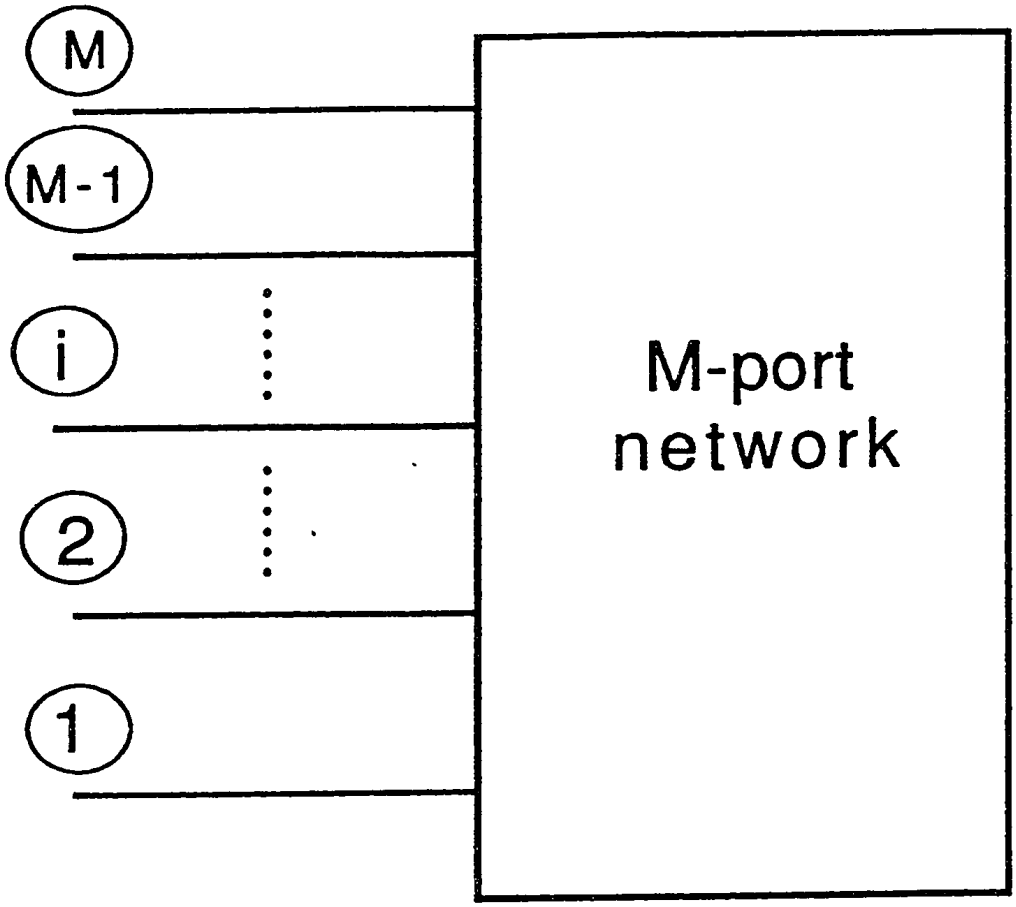

Figure 5.3: A N-Port Microwave Network

In approach a), the absorbing boundary termination is realized by cascading a number of sections of waveguide filled with homogeneous lossy material. The loss tangent is increased in the direction of the propagation such that reflection is minimized over a wide frequency range. For WR28 waveguide, a TLM network of $30\Delta l \times 180\Delta l$ was used for simulating the absorbing boundary termination, and less than -32dB return loss was obtained throughout the dominant mode operating band.

In approach b), the absorbing boundary termination is represented by a waveguide section long enough so that reflections from the far end cannot return to the input reference plane before the computation is stopped. A section of $1000\Delta l$ was used, yielding a Johns Matrix of 2000 time samples. A return loss better than -35 dB for such a single boundary was obtained over the WR28 dominant mode operating band.

By using the method presented here, the TLM absorbing boundary termination or matching load of the waveguide is modeled by a reflecting wall (one port network) with the frequency-domain reflection coefficient $\Gamma(f)$:

$$S_{11} = \Gamma(f) = \frac{Z(f)/\sqrt{2} - \eta_0}{Z(f)/\sqrt{2} + \eta_0} \tag{5.13}$$

where $Z(f) = \eta_0/\sqrt{\epsilon_r - (f/f_c)^2}$ is the wave impedance of the dominant mode in the waveguide, f is the operating frequency, f_c is the cutoff frequency, ϵ_r is the relative permittivity of the medium filling the guide, η_0 is the characteristic admittance of the link line of the TLM network, and the correction factor $\sqrt{2}$ is inherent to the slow-wave property of the 2-D TLM network [67].

Now, the procedure outlined in this paper is applied to the case of a WR28 waveguide. A section of it with $30\Delta l$ width is terminated at each side by absorbing boundaries (or matched load) for the dominant mode (see Fig.5.4). First, a time-domain sequence is generated by computing the inverse DFT of (5.13), corresponding to both limiting absorbing boundaries. The CPU time required for generating the sequences is only few seconds, which is at least three orders of magnitude below that reported in [29]. Subsequently, a TE_{10} mode field is injected in the TLM mesh with impulse time function, in order to simulate a wide-band excitation. As the TLM-impulses propagate through the TLM network and reach the absorbing boundaries, they are convolved at the boundary nodes with the stored sequences simulating the absorbing boundaries. After a sufficient number of iterations (in

this case 2000), the Fourier transform of the signal is performed at a few nodes (a minimum of two is required), from which the VSWR can be easily and rapidly determined and, therefore, the return loss calculated. Fig.5.5 shows the return loss produced by both terminations over a wide frequency range. One can see that a return loss better than -35dB is achieved over the operating range.

5.4.2 Application to highly conductive shields

The method can also be applied to the case of electromagnetic field diffusion through highly conducting materials. A typical application is the evaluation of shield effectiveness of cavities against electromagnetic interferences (EMI). The excitation is most likely a transient function for which a time-domain solution is the most appropriate. The TLM is an ideal tool for that application, except that in order to avoid network space and frequency dispersion, a very large number of nodes is necessary within highly conducting media [67], making the computational effort beyond practical limit.

In order to circumvent this problem, Johns matrix can be used. Unfortunately, for the same reasons just explained, the generation of such a matrix also requires a large amount of CPU time and memory core in most practical cases. However, with the method described here the shielding wall can be replaced by a section of lossy transmission lines inserted into the TLM network as shown in Fig.5.6. It is assumed that adjacent nodes on the conducting surface do not interact, which is a realistic hypothesis if one considers that fields are rapidly attenuated within the shield. The scattering parameters of such lossy lines can be determined easily from a harmonic field analysis or transmission line theory:

$$S_{11} = \frac{Z_1 - 1}{Z_1 + 1} \tag{5.14}$$

$$S_{12} = \frac{1 + \Gamma_2}{1 + \Gamma_2\, e^{-\gamma d}}\; e^{-2\gamma d}\; (1 + S_{11}) \tag{5.15}$$

$$S_{21} = S_{12} \tag{5.16}$$

$$S_{22} = S_{11} \tag{5.17}$$

where $\gamma = \sqrt{j\omega\mu\,(\sqrt{2}\sigma + 2j\omega c)}$, $Z_c = (2\epsilon_r + \frac{\sigma}{j\omega\epsilon_0})^{-\frac{1}{2}}$, $Z_1 = Z_c\,\frac{1+Z_c\,th(\gamma d)}{Z_c+th(\gamma d)}$, $\Gamma_2 = \frac{1-Z_c}{1+Z_c}$, $\omega =$

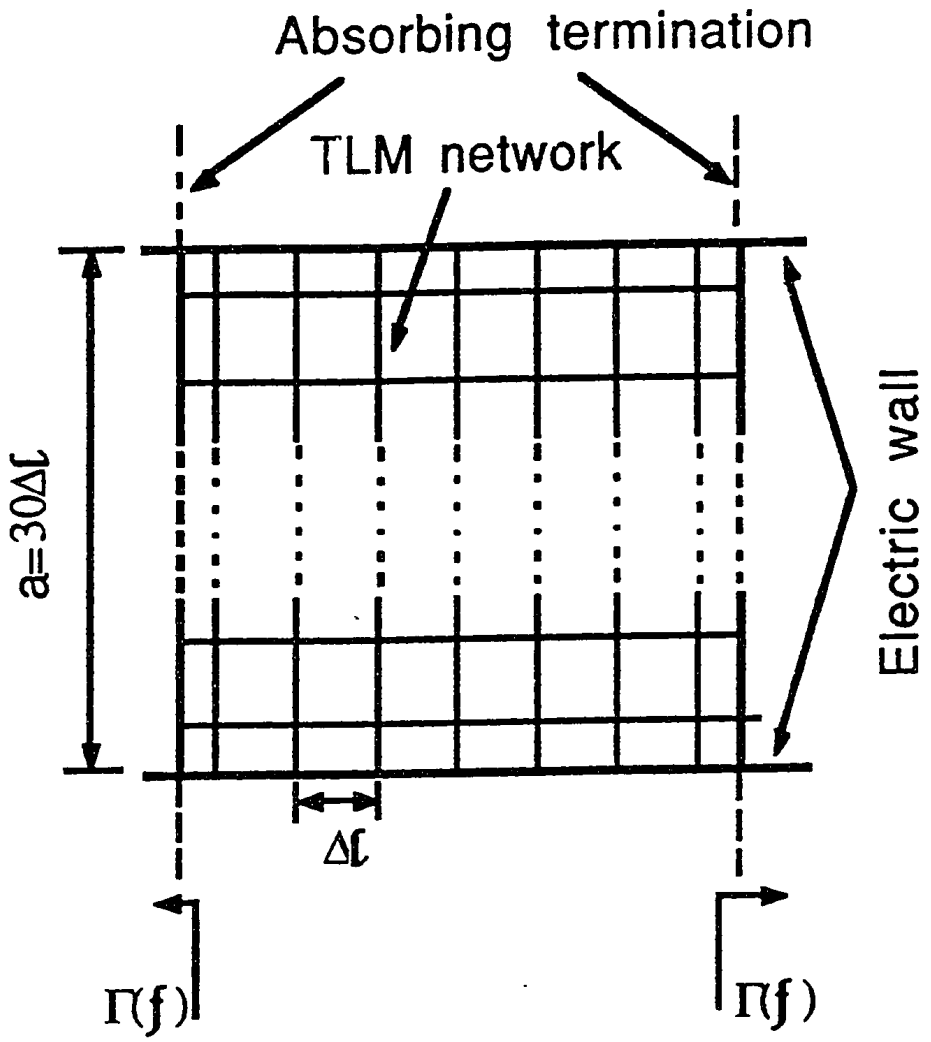

Figure 5.4: Geometry of the Rectangular Waveguide with the 2D Simulation

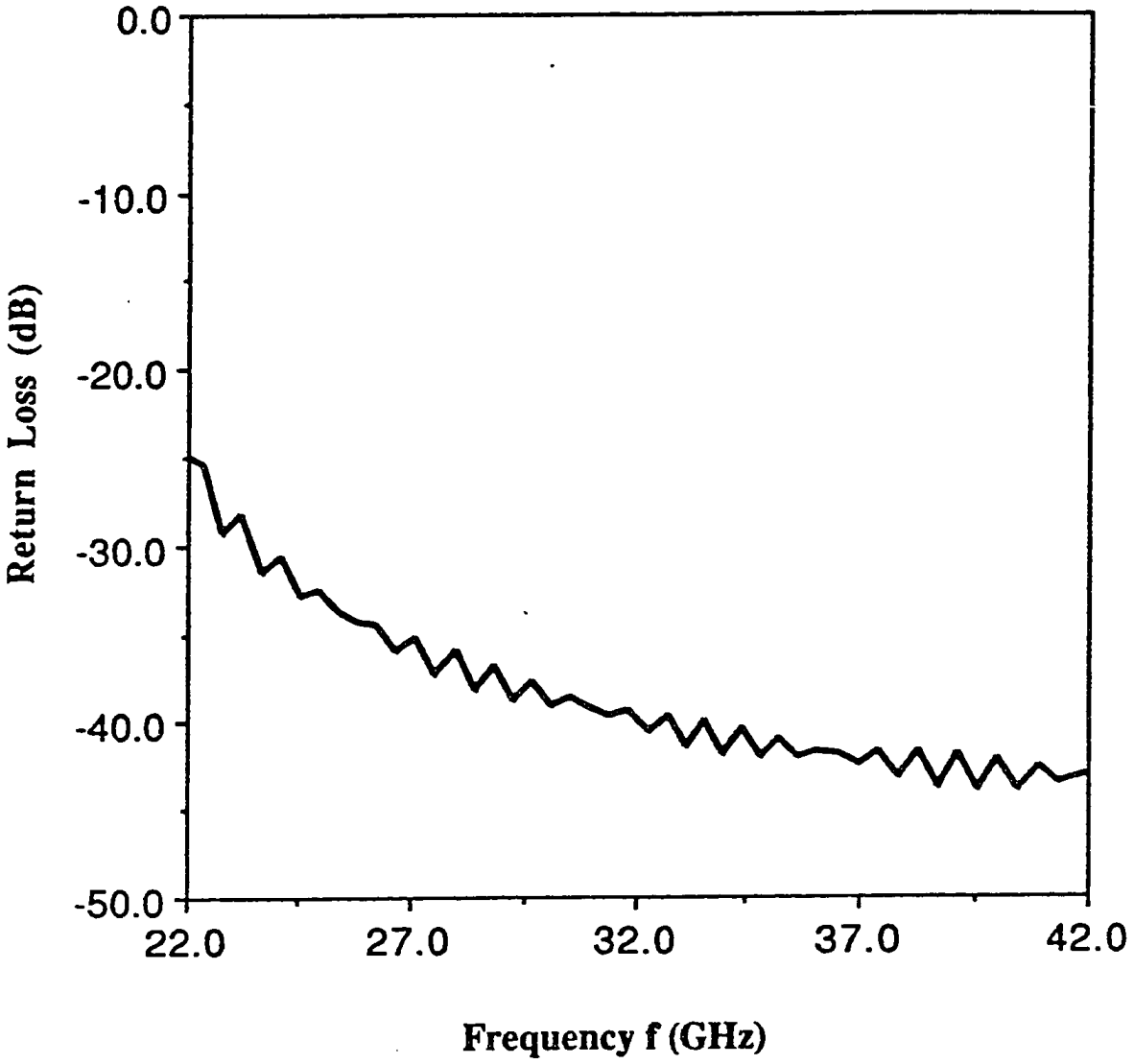

Figure 5.5: Return Loss in the Waveguide with Both Ends Terminated with Absorbing Terminations

$2\pi f$, $\epsilon = \epsilon_r \epsilon_0$, f is the frequency, ϵ_0 is the permittivity of the vacuum, ϵ_r, μ, σ and d are the relative permittivity, permeability and thickness of the conducting shield, respectively. And the correction factor 2 is inherent to the slow-wave property of the 2-D TLM network [67].

The transient field that impinges on a plane conducting wall is modeled by the following time function:

$$e^{inc}(t) = A\ e^{-t^2/2t_1^2} \tag{5.18}$$

where A is the value of $e^{inc}(0)$, t is the time and t_1 is a measure of the pulse width. A plane wave with the above time dependence was incident onto the conducting wall (see Fig.5.7). The time-function of 1000 iterations was observed at a node located behind the wall . The signal is shown in Fig.5.8 and compared with an analytical approach whose time-domain solution is found by the numerical inverse Fourier Transform calculation [97]. A good agreement between two methods can be observed.

5.5 Conclusion

A novel procedure based on time-frequency transformation for interfacing TLM algorithm with frequency-domain solutions is presented. It uses the *a priori* knowledge of the frequency behavior of the parameters such as reflection coefficients, network parameters or impedances which are known in many practical situations. The relationship between the frequency-domain parameters and the corresponding Johns Matrix of the network based on a DFT was presented in details. An example pertaining to modeling of the absorbing waveguide termination shows the excellent return loss level obtained with this method. Also the field penetration through highly conductive sheet demonstrates the efficiency of the approach that allows the TLM to be used for problems involving highly conducting media. It is important to mention that the procedure for finding the Johns matrix pertaining to such a problem is with CPU time orders of magnitude below the one required for the other methods. Finally, the method is not restricted to two-dimensional problems and can be extended to 3D and more general geometry cases without great difficulties.

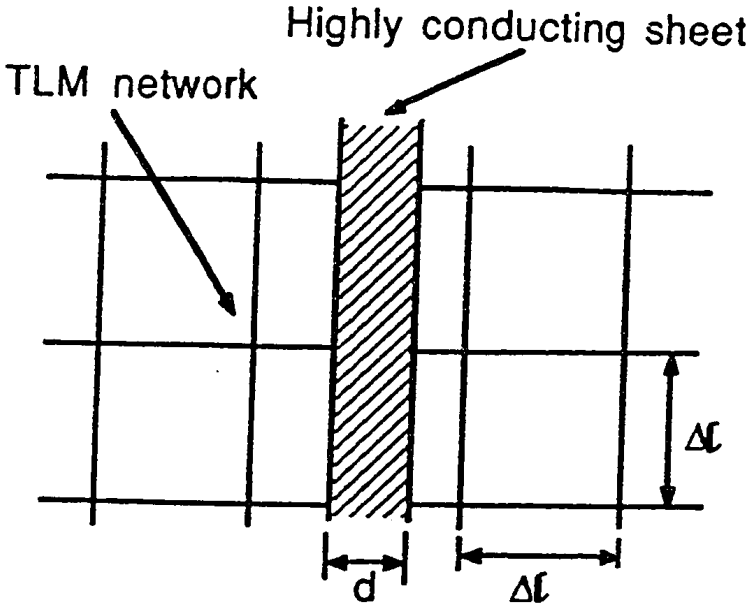

(a) A TLM network containing a highly conducting sheet

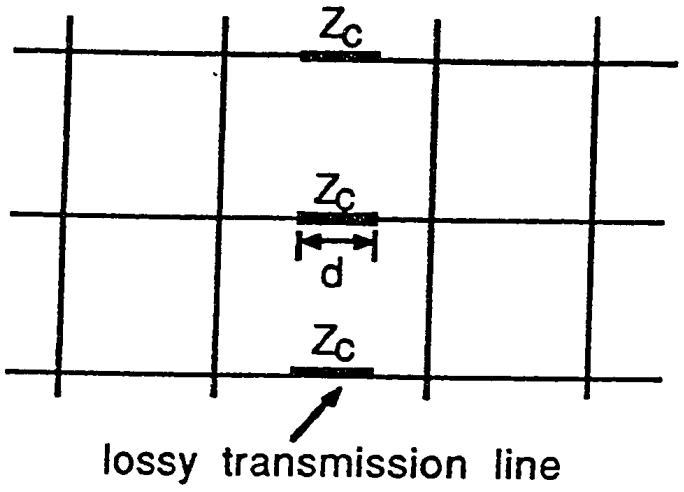

(b) Equivalent TLM network for (a)

Figure 5.6: A TLM Network incorporating with a Highly Conductive Sheet ($d << \Delta l$)

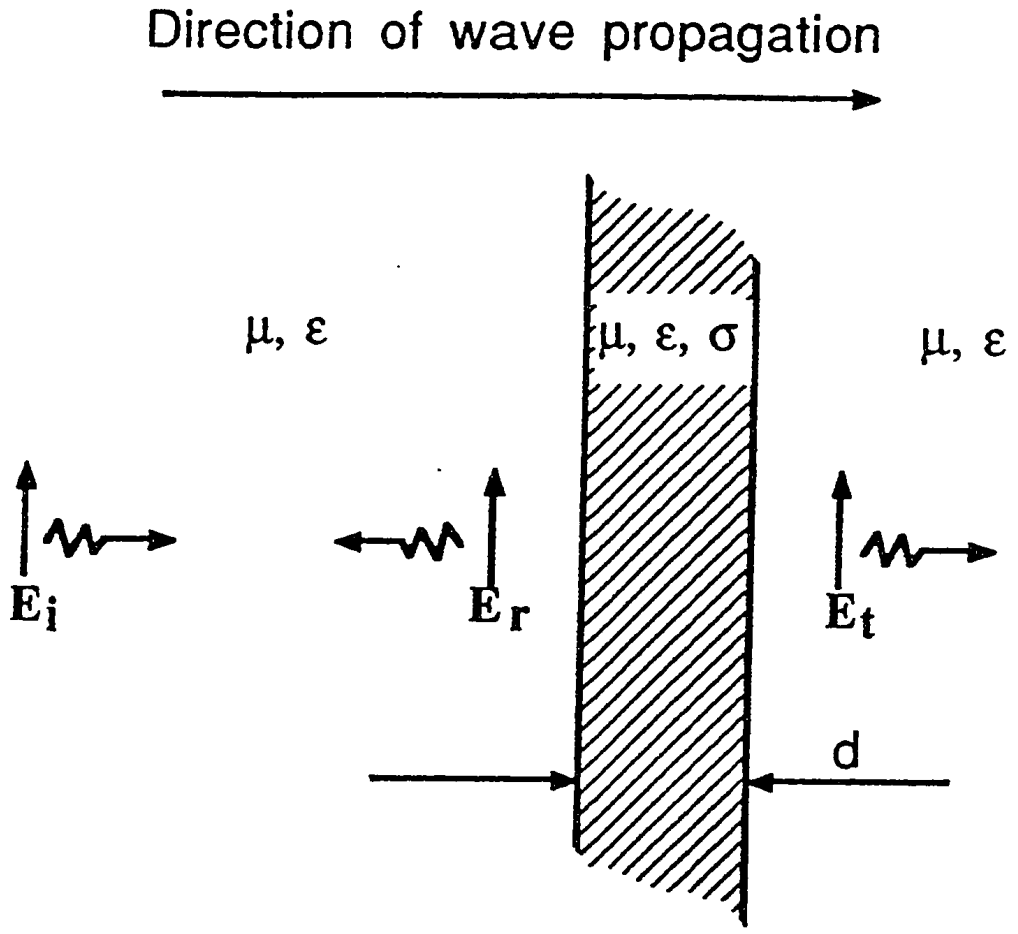

Figure 5.7: An Infinite Conducting Sheet with Thickness d and Conductivity σ Irradiated by a Plane Wave

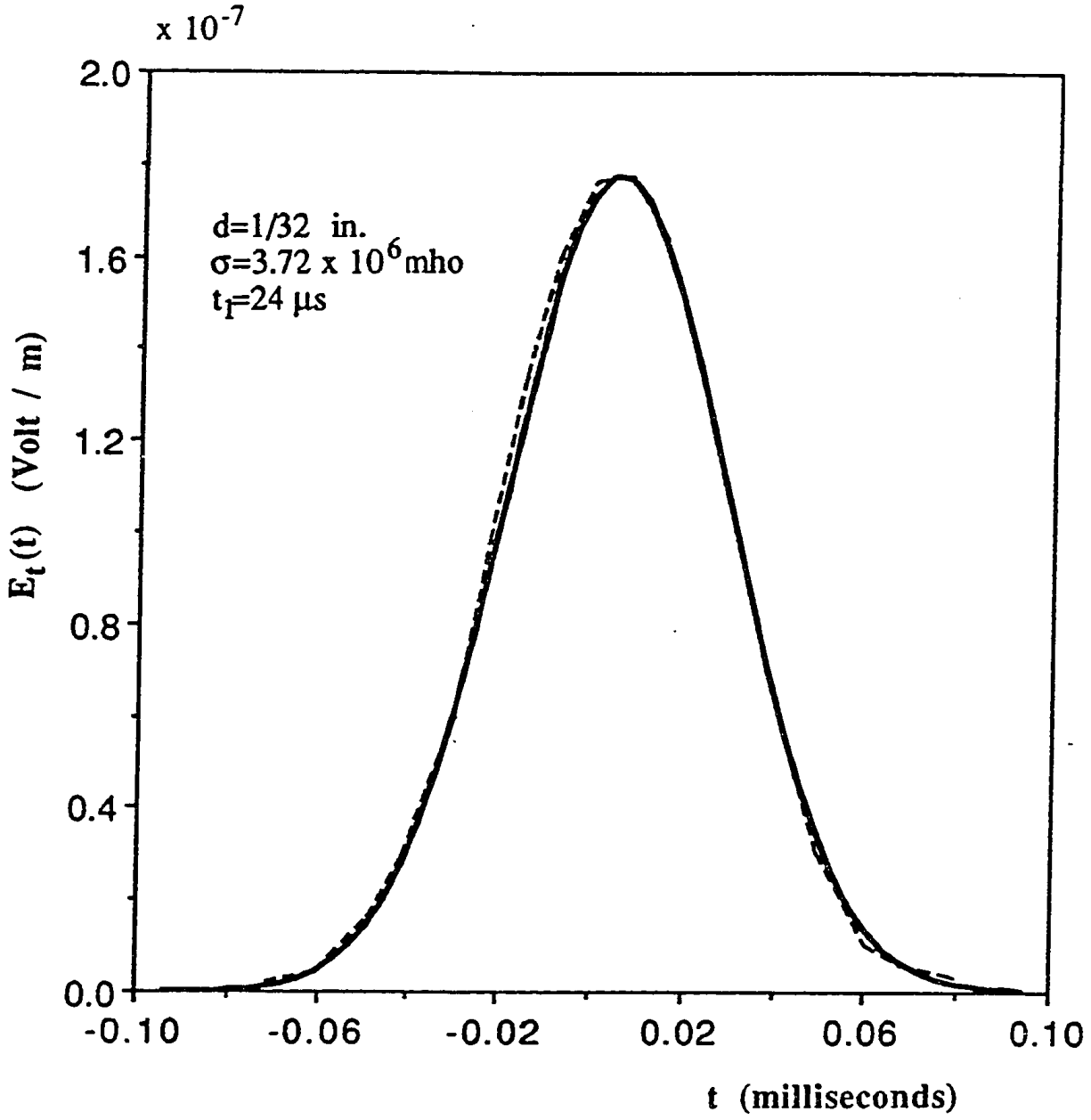

Figure 5.8: Comparison of the TLM Results (solid line) and the Solutions of Inverse Fourier Transformation (dash line) for the E-field Transmitted through the Conducting Sheet

Chapter 6

Conclusion

The equivalence between the Transmission Line Matrix (TLM) method and the Finite-Difference Time-Domain (FD-TD) approach has been explored. It provides the theoretical basis for mathematically understanding the TLM algorithm, and the systematic ways for developing boundary conditions. As a result, the conventional boundary conditions has been verified theoretically and a new boundary conditions has been formulated. In addition, the conversion of the TLM solutions has been presented.

Absorbing boundary conditions and the connecting boundary conditions play an important role in applying the TLM method to scattering, radiation and open structure problems. Based on the techniques employed in the present FD-TD scheme, the formulations of absorbing and connecting conditions for the TLM simulations have been developed, and validations of these conditions have been obtained. This makes the TLM method applicable to deal with more realistic problems, extensively broadening the application spectrum of the TLM approach.

A new procedure for interfacing the TLM method with the frequency-domain solutions has been presented. It reveals the relationship between the TLM method and the frequency-domain solutions. By employing this relation, the memory and CPU time requirement can be significantly reduced for certain practical problems.

In conclusions, the work presented in thesis has broadened the knowledge and applications of the TLM method. However, it has been found that throughout the simulations done for this thesis, CPU time and memory required to model realistic electromagnetic structures have been very intensive, especially when it comes to model 3D structures. Therefore, to the author's knowledge, the future research efforts should still concentrate on the ways to reduce the computation expenditure significantly and to adopt new compu-

tation techniques into the TLM simulation with the recent development of more powerful high-speed computers.

Appendix A

The General Formulations of the New FD-TD Method

Consider a 3D cell with the side widths of δx, δy and δz as shown in Fig. A.1. At the center of the 3D cell, all the six field components are defined while on the boundary surfaces of the 3D cell, only the tangential field components are defined. Assume that $\delta l = c_o\ \delta t$, where c_o is equal to either $1/\sqrt{\mu_0 \varepsilon_0}$ or $2/\sqrt{\mu \varepsilon}$ ($\varepsilon = 2\,\varepsilon_0\,\varepsilon_r$, $\mu = 2\,\mu_0 \mu_r$, ε_0 and μ_0 are the permittivity and permeability of the vacuum medium) and δt is the time step of the FD-TD model.

Then, by finite-differencing Maxwell's equations, one can obtain the following equations to update the six field components at the center of the cell:

$$-\mu \frac{{}^{n+1}H_x(i_x, i_y, i_z) - {}_n H_x(i_x, i_y, i_z)}{\delta t} = \frac{{}^{n+\frac{1}{2}}E_z(i_x, i_y + \frac{1}{2}, i_z) - {}_{n+\frac{1}{2}} E_z(i_x, i_y - \frac{1}{2}, i_z)}{\delta y} - \frac{{}^{n+\frac{1}{2}}E_y(i_x, i_y, i_z + \frac{1}{2}) - {}_{n+\frac{1}{2}} E_y(i_x, i_y, i_z - \frac{1}{2})}{\delta z} \tag{A.1}$$

$$-\mu \frac{{}^{n+1}H_y(i_x, i_y, i_z) - {}_n H_y(i_x, i_y, i_z)}{\delta t} = \frac{{}^{n+\frac{1}{2}}E_x(i_x, i_y, i_z + \frac{1}{2}) - {}_{n+\frac{1}{2}} E_x(i_x, i_y, i_z - \frac{1}{2})}{\delta z} - \frac{{}^{n+\frac{1}{2}}E_z(i_x + \frac{1}{2}, i_y, i_z) - {}_{n+\frac{1}{2}} E_z(i_x - \frac{1}{2}, i_y, i_z)}{\delta x} \tag{A.2}$$

$$-\mu \frac{{}^{n+1}H_z(i_x, i_y, i_z) - {}_n H_z(i_x, i_y, i_z)}{\delta t} = \frac{{}^{n+\frac{1}{2}}E_y(i_x + \frac{1}{2}, i_y, i_z) - {}_{n+\frac{1}{2}} E_y(i_x - \frac{1}{2}, i_y, i_z)}{\delta x} - \frac{{}^{n+\frac{1}{2}}E_x(i_x, i_y + \frac{1}{2}, i_z) - {}_{n+\frac{1}{2}} E_x(i_x, i_y - \frac{1}{2}, i_z)}{\delta y} \tag{A.3}$$

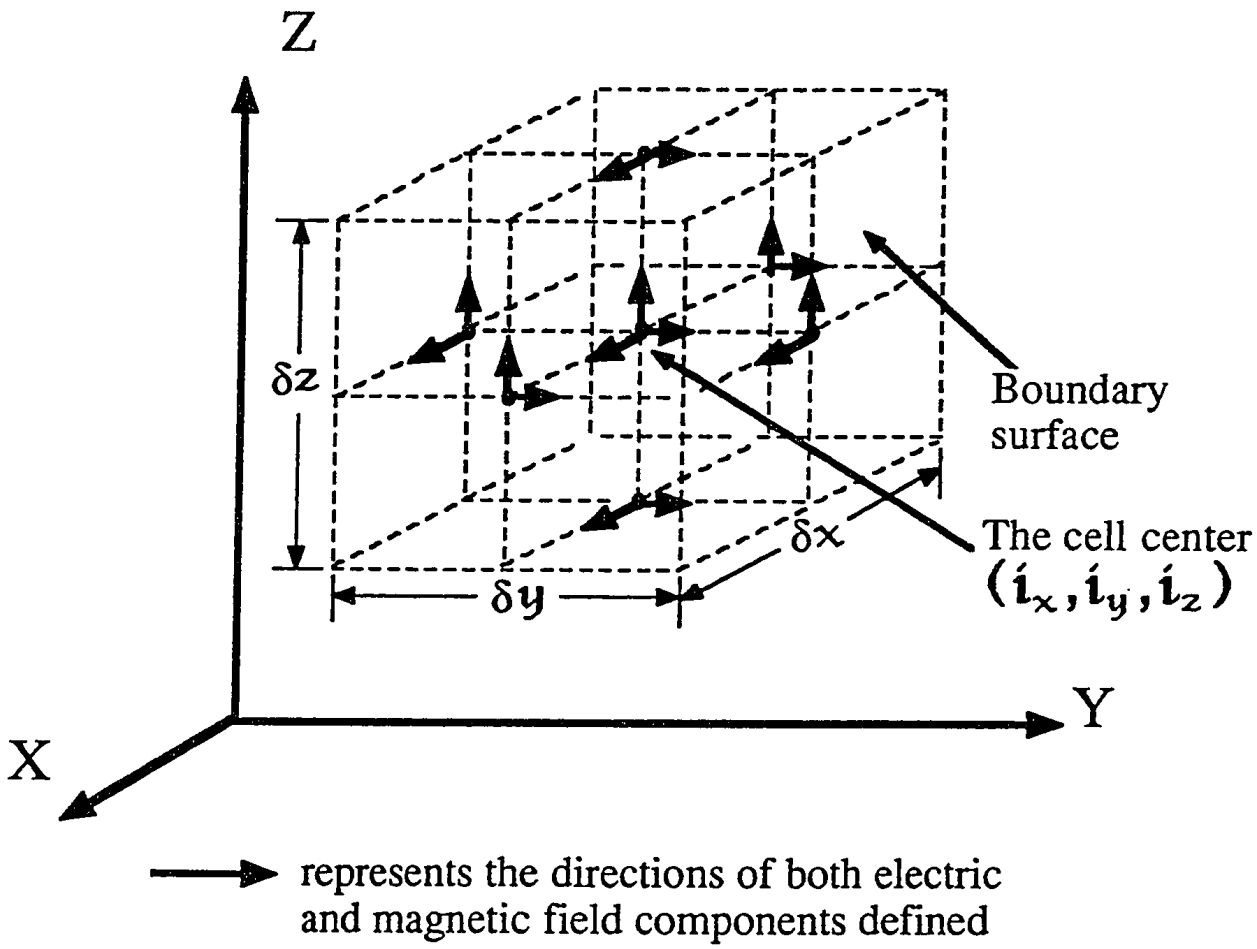

Figure A.1: **The Grid Position about a 3D Cell of the FD-TD formulation**

$$\varepsilon\frac{{}^{n+1}E_x(i_x,i_y,i_z)-{}_n\,E_x(i_x,i_y,i_z)}{\delta t}+\sigma\frac{{}^{n+1}E_x(i_x,i_y,i_z)+{}_n\,E_x(i_x,i_y,i_z)}{2}=$$
$$\frac{{}^{n+\frac{1}{2}}H_z(i_x,i_y+\frac{1}{2},i_z)-{}_{n+\frac{1}{2}}\,H_z(i_x,i_y-\frac{1}{2},i_z)}{\delta y}-\frac{{}^{n+\frac{1}{2}}H_y(i_x,i_y,i_z+\frac{1}{2})-{}_{n+\frac{1}{2}}\,H_y(i_x,i_y,i_z-\frac{1}{2})}{\delta z} \tag{A.4}$$

$$\varepsilon\frac{{}^{n+1}E_y(i_x,i_y,i_z)-{}_n\,E_y(i_x,i_y,i_z)}{\delta t}+\sigma\frac{{}^{n+1}E_y(i_x,i_y,i_z)+{}_n\,E_y(i_x,i_y,i_z)}{2}=$$
$$\frac{{}^{n+\frac{1}{2}}H_x(i_x,i_y,i_z+\frac{1}{2})-{}_{n+\frac{1}{2}}\,H_x(i_x,i_y,i_z-\frac{1}{2})}{\delta z}-\frac{{}^{n+\frac{1}{2}}H_z(i_x+\frac{1}{2},i_y,i_z)-{}_{n+\frac{1}{2}}\,H_z(i_x-\frac{1}{2},i_y,i_z)}{\delta x} \tag{A.5}$$

$$\varepsilon\frac{{}^{n+1}E_z(i_x,i_y,i_z)-{}_n\,E_z(i_x,i_y,i_z)}{\delta t}+\sigma\frac{{}^{n+1}E_z(i_x,i_y,i_z)+{}_n\,E_z(i_x,i_y,i_z)}{2}=$$
$$\frac{{}^{n+\frac{1}{2}}H_y(i_x+\frac{1}{2},i_y,i_z)-{}_{n+\frac{1}{2}}\,H_y(i_x-\frac{1}{2},i_y,i_z)}{\delta x}-\frac{{}^{n+\frac{1}{2}}H_x(i_x,i_y+\frac{1}{2},i_z)-{}_{n+\frac{1}{2}}\,H_x(i_x,i_y-\frac{1}{2},i_z)}{\delta y} \tag{A.6}$$

where σ is the conductivity of the medium being modeled.

By taking the space and time averaging processes similar to those described in Chapter 2, one can obtain the following equations to update the field components on the surfaces of the 3D cell:

$$\begin{aligned}&{}_nE_x(i_x,i_y,i_z)-Z_o\;{}_nH_z(i_x,i_y,i_z)=\\&\quad\frac{1}{2}\frac{\delta l}{\delta y}[{}_{n+\frac{1}{2}}E_x(i_x,i_y+\frac{1}{2},i_z)-Z_o\;{}_{n+\frac{1}{2}}H_z(i_x,i_y+\frac{1}{2},i_z)\\&\quad+{}_{n-\frac{1}{2}}\,E_x(i_x,i_y-\frac{1}{2},i_z)-Z_o\;{}_{n-\frac{1}{2}}H_z(i_x,i_y-\frac{1}{2},i_z)]\end{aligned} \tag{A.7}$$

$$\begin{aligned}&{}_nE_x(i_x,i_y+1,i_z)+Z_o\;{}_nH_z(i_x,i_y+1,i_z)=\\&\quad\frac{1}{2}\frac{\delta l}{\delta y}[{}_{n+\frac{1}{2}}E_x(i_x,i_y+\frac{1}{2},i_z)+Z_o\;{}_{n+\frac{1}{2}}H_z(i_x,i_y+\frac{1}{2},i_z)\\&\quad+{}_{n-\frac{1}{2}}\,E_x(i_x,i_y+\frac{3}{2},i_z)+Z_o\;{}_{n-\frac{1}{2}}H_z(i_x,i_y+\frac{3}{2},i_z)]\end{aligned} \tag{A.8}$$

$$\begin{aligned}&{}_nE_z(i_x,i_y,i_z)+Z_o\;{}_nH_x(i_x,i_y,i_z)=\\&\quad\frac{1}{2}\frac{\delta l}{\delta y}[{}_{n+\frac{1}{2}}E_z(i_x,i_y+\frac{1}{2},i_z)+Z_o\;{}_{n+\frac{1}{2}}H_x(i_x,i_y+\frac{1}{2},i_z)\\&\quad+{}_{n-\frac{1}{2}}\,E_z(i_x,i_y-\frac{1}{2},i_z)+Z_o\;{}_{n-\frac{1}{2}}H_x(i_x,i_y-\frac{1}{2},i_z)]\end{aligned} \tag{A.9}$$

$$
\begin{aligned}
&{}_nE_z(i_x, i_y+1, i_z) - Z_o\ {}_nH_x(i_x, i_y+1, i_z) = \\
&\quad \frac{1}{2}\frac{\delta l}{\delta y}[{}_{n+\frac{1}{2}}E_z(i_x, i_y+\frac{1}{2}, i_z) - Z_o\ {}_{n+\frac{1}{2}}H_x(i_x, i_y+\frac{1}{2}, i_z) \\
&\quad +{}_{n-\frac{1}{2}}E_z(i_x, i_y+\frac{3}{2}, i_z) - Z_o\ {}_{n-\frac{1}{2}}H_x(i_x, i_y+\frac{3}{2}, i_z)] \qquad \text{(A.10)}
\end{aligned}
$$

$$
\begin{aligned}
&{}_nE_y(i_x, i_y, i_z) - Z_o\ {}_nH_x(i_x, i_y, i_z) = \\
&\quad \frac{1}{2}\frac{\delta l}{\delta z}[{}_{n+\frac{1}{2}}E_y(i_x, i_y, i_z+\frac{1}{2}) - Z_o\ {}_{n+\frac{1}{2}}H_x(i_x, i_y, i_z+\frac{1}{2}) \\
&\quad +{}_{n-\frac{1}{2}}E_y(i_x, i_y, i_z-\frac{1}{2}) - Z_o\ {}_{n-\frac{1}{2}}H_x(i_x, i_y, i_z-\frac{1}{2})] \qquad \text{(A.11)}
\end{aligned}
$$

$$
\begin{aligned}
&{}_nE_y(i_x, i_y, i_z+1) + Z_o\ {}_nH_x(i_x, i_y, i_z+1) = \\
&\quad \frac{1}{2}\frac{\delta l}{\delta z}[{}_{n+\frac{1}{2}}E_y(i_x, i_y, i_z+\frac{1}{2}) + Z_o\ {}_{n+\frac{1}{2}}H_x(i_x, i_y, i_z+\frac{1}{2}) \\
&\quad +{}_{n-\frac{1}{2}}E_y(i_x, i_y, i_z+\frac{3}{2}) + Z_o\ {}_{n-\frac{1}{2}}H_x(i_x, i_y, i_z+\frac{3}{2})] \qquad \text{(A.12)}
\end{aligned}
$$

$$
\begin{aligned}
&{}_nE_x(i_x, i_y, i_z) + Z_o\ {}_nH_y(i_x, i_y, i_z) = \\
&\quad \frac{1}{2}\frac{\delta l}{\delta z}[{}_{n+\frac{1}{2}}E_x(i_x, i_y, i_z+\frac{1}{2}) + Z_o\ {}_{n+\frac{1}{2}}H_y(i_x, i_y, i_z+\frac{1}{2}) \\
&\quad +{}_{n-\frac{1}{2}}E_x(i_x, i_y, i_z-\frac{1}{2}) + Z_o\ {}_{n-\frac{1}{2}}H_y(i_x, i_y, i_z-\frac{1}{2})] \qquad \text{(A.13)}
\end{aligned}
$$

$$
\begin{aligned}
&{}_nE_x(i_x, i_y, i_z+1) - Z_o\ {}_nH_y(i_x, i_y, i_z+1) = \\
&\quad \frac{1}{2}\frac{\delta l}{\delta z}[{}_{n+\frac{1}{2}}E_x(i_x, i_y, i_z+\frac{1}{2}) - Z_o\ {}_{n+\frac{1}{2}}H_y(i_x, i_y, i_z+\frac{1}{2}) \\
&\quad +{}_{n-\frac{1}{2}}E_x(i_x, i_y, i_z+\frac{3}{2}) - Z_o\ {}_{n-\frac{1}{2}}H_y(i_x, i_y, i_z+\frac{3}{2})] \qquad \text{(A.14)}
\end{aligned}
$$

$$
\begin{aligned}
&{}_nE_z(i_x, i_y, i_z) - Z_o\ {}_nH_y(i_x, i_y, i_z) = \\
&\quad \frac{1}{2}\frac{\delta l}{\delta x}[{}_{n+\frac{1}{2}}E_z(i_x+\frac{1}{2}, i_y, i_z) - Z_o\ {}_{n+\frac{1}{2}}H_y(i_x+\frac{1}{2}, i_y, i_z) \\
&\quad +{}_{n-\frac{1}{2}}E_z(i_x-\frac{1}{2}, i_y, i_z) - Z_o\ {}_{n-\frac{1}{2}}H_y(i_x-\frac{1}{2}, i_y, i_z)] \qquad \text{(A.15)}
\end{aligned}
$$

$$
\begin{aligned}
&{}_nE_z(i_x+1,i_y,i_z)+Z_o\ {}_nH_y(i_x+1,i_y,i_z)= \\
&\quad\frac{1}{2}\frac{\delta l}{\delta x}[{}_{n+\frac{1}{2}}E_z(i_x+\frac{1}{2},i_y,i_z)+Z_o\ {}_{n+\frac{1}{2}}H_y(i_x+\frac{1}{2},i_y,i_z) \\
&\quad+{}_{n-\frac{1}{2}}E_z(i_x+\frac{3}{2},i_y,i_z)+Z_o\ {}_{n-\frac{1}{2}}H_y(i_x+\frac{3}{2},i_y,i_z)] \qquad \text{(A.16)}
\end{aligned}
$$

$$
\begin{aligned}
&{}_nE_y(i_x,i_y,i_z)+Z_o\ {}_nH_z(i_x,i_y,i_z)= \\
&\quad\frac{1}{2}\frac{\delta l}{\delta x}[{}_{n+\frac{1}{2}}E_y(i_x+\frac{1}{2},i_y,i_z)+Z_o\ {}_{n+\frac{1}{2}}H_z(i_x+\frac{1}{2},i_y,i_z) \\
&\quad+{}_{n-\frac{1}{2}}E_y(i_x-\frac{1}{2},i_y,i_z)+Z_o\ {}_{n-\frac{1}{2}}H_z(i_x-\frac{1}{2},i_y,i_z)] \qquad \text{(A.17)}
\end{aligned}
$$

$$
\begin{aligned}
&{}_nE_y(i_x+1,i_y,i_z)-Z_o\ {}_nH_z(i_x+1,i_y,i_z)= \\
&\quad\frac{1}{2}\frac{\delta l}{\delta x}[{}_{n+\frac{1}{2}}E_y(i_x+\frac{1}{2},i_y,i_z)-Z_o\ {}_{n+\frac{1}{2}}H_z(i_x+\frac{1}{2},i_y,i_z) \\
&\quad+{}_{n-\frac{1}{2}}E_y(i_x+\frac{3}{2},i_y,i_z)-Z_o\ {}_{n-\frac{1}{2}}H_z(i_x+\frac{3}{2},i_y,i_z)] \qquad \text{(A.18)}
\end{aligned}
$$

where $Z_o=\sqrt{\frac{\mu_0}{\varepsilon_0}}$ if c_0 is chosen to equal to $1/\sqrt{\mu_0\varepsilon_0}$, or, $Z_o=\sqrt{\frac{\mu}{\varepsilon}}$ if c_0 is chosen to be equal to $2/\sqrt{\mu\varepsilon}$. It is recommended that $Z_o=\sqrt{\frac{\mu_0}{\varepsilon_0}}$ and $c_0=1/\sqrt{\mu_0\varepsilon_0}$ be chosen since (A.7) to (A.18) would be independent of the medium permeability and permittivity.

(A.1) to (A.18) form a recursive numerical algorithm for the new FD-TD method which is equivalent to the 3D TLM symmetrical condensed node model.

Appendix B

Derivation of Voltage and Current Relations in the 2D TLM Shunt Node Model

Taking the same notation as in Chapter 2 and referring to Fig.2.6, one can note that ${}_{n+\frac{1}{2}}V_2^i(i_x, i_z-\frac{1}{2})$ arrives at the node (i_x, i_z) at time $(n+1)\Delta t$ and is denoted as ${}_{n+1}V_2^i(i_x, i_z)$, and ${}_nV_2^r(i_x, i_z)$ arrives at the mid-point $(i_x, i_z - \frac{1}{2})$ at time $(n + \frac{1}{2})\,\Delta t$ and is denoted as ${}_{n+\frac{1}{2}}V_2^r(i_x, i_z-\frac{1}{2})$, that is: ${}_{n+\frac{1}{2}}V_2^i(i_x, i_z-\frac{1}{2}) = {}_{n+1}V_2^i(i_x, i_z)$, and ${}_{n+\frac{1}{2}}V_2^r(i_x, i_z - \frac{1}{2}) = {}_nV_2^r(i_x, i_z)$. For this reason, one has:

$$ {}_{n+\frac{1}{2}}V_y(i_x, i_z - \frac{1}{2}) = {}_{n+1}V_2^i(i_x, i_z) + {}_nV_2^r(i_x, i_z) \tag{B.1} $$

$$ {}_{n+\frac{1}{2}}I_z(i_x, i_z - \frac{1}{2}) = [{}_{n+1}V_2^i(i_x, i_z) - {}_nV_2^r(i_x, i_z)]/Z_0 \tag{B.2} $$

$$ \begin{aligned} {}_{n+\frac{1}{2}}V_y(i_x + \frac{1}{2}, i_z) &= {}_{n+\frac{1}{2}}V_3^i(i_x + \frac{1}{2}, i_z) + {}_{n+\frac{1}{2}}V_3^r(i_x + \frac{1}{2}, i_z) \\ &= {}_{n+1}V_3^i(i_x, i_z) + {}_nV_3^r(i_x, i_z) \end{aligned} \tag{B.3} $$

$$ \begin{aligned} {}_{n+\frac{1}{2}}V_y(i_x - \frac{1}{2}, i_z) &= {}_{n+\frac{1}{2}}V_1^i(i_x - \frac{1}{2}, i_z) + {}_{n+\frac{1}{2}}V_1^r(i_x - \frac{1}{2}, i_z) \\ &= {}_{n+1}V_1^i(i_x, i_z) + {}_nV_1^r(i_x, i_z) \end{aligned} \tag{B.4} $$

$$ \begin{aligned} {}_{n+\frac{1}{2}}V_y(i_x, i_z + \frac{1}{2}) &= {}_{n+\frac{1}{2}}V_4^i(i_x, i_z + \frac{1}{2}) + {}_{n+\frac{1}{2}}V_4^r(i_x, i_z + \frac{1}{2}) \\ &= {}_{n+1}V_4^i(i_x, i_z) + {}_nV_4^r(i_x, i_z) \end{aligned} \tag{B.5} $$

$$
\begin{aligned}
{}_{n+\frac{1}{2}}V_y(i_x, i_z - \frac{1}{2}) &= {}_{n+\frac{1}{2}}V_2^i(i_x, i_z - \frac{1}{2}) +_{n+\frac{1}{2}} V_2^r(i_x, i_z - \frac{1}{2}) \\
&= {}_{n+1}V_2^i(i_x, i_z) +_n V_2^r(i_x, i_z) \qquad \text{(B.6)}
\end{aligned}
$$

$$
\begin{aligned}
{}_{n+\frac{1}{2}}I_x(i_x - \frac{1}{2}, i_z) &= [{}_{n+\frac{1}{2}}V_1^i(i_x - \frac{1}{2}, i_z) -_{n+\frac{1}{2}} V_1^r(i_x - \frac{1}{2}, i_z)]/Z_0 \\
&= [{}_{n+1}V_1^i(i_x, i_z) -_n V_1^r(i_x, i_z)]/Z_0
\end{aligned}
$$

$$
\begin{aligned}
{}_{n+\frac{1}{2}}I_x(i_x + \frac{1}{2}, i_z) &= [{}_{n+\frac{1}{2}}V_3^r(i_x + \frac{1}{2}, i_z) -_{n+\frac{1}{2}} V_3^i(i_x + \frac{1}{2}, i_z)]/Z_0 \\
&= [{}_nV_3^r(i_x, i_z) -_{n+1} V_3^i(i_x, i_z)]/Z_0 \qquad \text{(B.7)}
\end{aligned}
$$

$$
\begin{aligned}
{}_{n+\frac{1}{2}}I_z(i_x, i_z - \frac{1}{2}) &= [{}_{n+\frac{1}{2}}V_2^i(i_x, i_z - \frac{1}{2}) -_{n+\frac{1}{2}} V_2^r(i_x, i_z - \frac{1}{2})]/Z_0 \\
&= [{}_{n+1}V_2^i(i_x, i_z) -_n V_2^r(i_x, i_z)]/Z_0 \qquad \text{(B.8)}
\end{aligned}
$$

$$
\begin{aligned}
{}_{n+\frac{1}{2}}I_z(i_x, i_z + \frac{1}{2}) &= [{}_{n+\frac{1}{2}}V_4^r(i_x, i_z + \frac{1}{2}) -_{n+\frac{1}{2}} V_4^i(i_x, i_z + \frac{1}{2})]/Z_0 \\
&= [{}_nV_4^r(i_x, i_z) -_{n+1} V_4^i(i_x, i_z)]/Z_0 \\
{}_nV_y(i_x, i_z) &= \frac{1}{2}({}_nV_1^i(i_x, i_z) +_n V_2^i(i_x, i_z) +_n V_3^i(i_x, i_z) +_n V_4^i(i_x, i_z)) \qquad \text{(B.9)}
\end{aligned}
$$

$$
{}_nI_z(i_x, i_z) = ({}_nV_4^i(i_x, i_z) -_n V_2^i(i_x, i_z))/Z_o \qquad \text{(B.10)}
$$

$$
{}_nI_x(i_x, i_z) = ({}_nV_3^i(i_x, i_z) -_n V_1^i(i_x, i_z))/Z_o \qquad \text{(B.11)}
$$

(B.12)

In addition, the TLM impulse scattering process is defined as follows[67]:

$$
{}_n\mathbf{V}^r(i_x, i_z) = [\mathrm{S}] \quad {}_n\mathbf{V}^i(i_x, i_z) \qquad \text{(B.13)}
$$

Recalling that $Z_O = \sqrt{\frac{L}{C}}$ and $\frac{\Delta l}{\Delta t} = \frac{1}{\sqrt{LC}}$, one can easily shows from the above relations that

$$
-L\frac{{}_{n+1}I_x(i_x, i_z) -_n I_x(i_x, i_z)}{\Delta t} = \frac{{}_{n+\frac{1}{2}}V_y(i_x + \frac{1}{2}, i_z) -_{n+\frac{1}{2}} V_y(i_x - \frac{1}{2}, i_z)}{\Delta l} \qquad \text{(B.14)}
$$

$$-L\frac{{}^{n+1}I_z(i_x,i_z)-{}_nI_z(i_x,i_z)}{\Delta t}=\frac{{}_{n+\frac{1}{2}}V_y(i_x,i_z+\frac{1}{2})-{}_{n+\frac{1}{2}}V_y(i_x,i_z-\frac{1}{2})}{\Delta l} \tag{B.15}$$

$$2\,C\frac{{}^{n+1}V_y(i_x,i_z)-{}_nV_y(i_x,i_z)}{\Delta t}=$$
$$-\frac{{}_{n+\frac{1}{2}}I_z(i_x,i_z+\frac{1}{2})-{}_{n+\frac{1}{2}}I_z(i_x,i_z-\frac{1}{2})}{\Delta l}-\frac{{}_{n+\frac{1}{2}}I_x(i_x+\frac{1}{2},i_z)-{}_{n+\frac{1}{2}}I_x(i_x-\frac{1}{2},i_z)}{\Delta l} \tag{B.16}$$

(B.17)

and

$${}_nV_y(i_x,i_z)+Z_o\ {}_nI_z(i_x,i_z)=$$
$$\frac{[{}_{n+\frac{1}{2}}V_y(i_x,i_z+\frac{1}{2})+Z_o\ {}_{n+\frac{1}{2}}I_z(i_x,i_z+\frac{1}{2})]+[{}_{n-\frac{1}{2}}V_y(i_x,i_z-\frac{1}{2})+Z_o\ {}_{n-\frac{1}{2}}I_z(i_x,i_z-\frac{1}{2}]}{2} \tag{B.18}$$

$${}_nV_y(i_x,i_z+1)-Z_o\ {}_nI_z(i_x,i_z+1)=$$
$$\frac{[{}_{n+\frac{1}{2}}V_y(i_x,i_z+\frac{1}{2})-Z_o\ {}_{n+\frac{1}{2}}I_z(i_x,i_z+\frac{1}{2})]+[{}_{n-\frac{1}{2}}V_y(i_x,i_z+\frac{3}{2})-Z_o\ {}_{n-\frac{1}{2}}I_z(i_x,i_z+\frac{3}{2})]}{2} \tag{B.19}$$

$${}_nV_y(i_x,i_z)+Z_o\ {}_nI_x(i_x,i_z)=$$
$$\frac{[{}_{n+\frac{1}{2}}V_y(i_x+\frac{1}{2},i_z)+Z_o\ {}_{n+\frac{1}{2}}I_x(i_x+\frac{1}{2},i_z)]+[{}_{n-\frac{1}{2}}V_y(i_x-\frac{1}{2},i_z)+Z_o\ {}_{n-\frac{1}{2}}I_x(i_x-\frac{1}{2},i_z)]}{2} \tag{B.20}$$

$${}_nV_y(i_x+1,i_z)-Z_o\ {}_nI_x(i_x+1,i_z)=$$
$$\frac{[{}_{n+\frac{1}{2}}V_y(i_x+\frac{1}{2},i_z)-Z_o\ {}_{n+\frac{1}{2}}I_x(i_x+\frac{1}{2},i_z)]+[{}_{n-\frac{1}{2}}V_y(i_x+\frac{3}{2},i_z)-Z_o\ {}_{n-\frac{1}{2}}I_x(i_x+\frac{3}{2},i_z)]}{2} \tag{B.21}$$

From above, one can have:

$$
\begin{aligned}
&{}_{n+\frac{1}{2}}V_y(i_x, i_z+\frac{1}{2}) = \\
&\quad {}_nV_y(i_x, i_z) + Z_o\ {}_nI_z(i_x, i_z) + {}_nV_y(i_x, i_z+1) - Z_o\ {}_nI_z(i_x, i_z+1) \\
&\quad -\frac{1}{2}[{}_{n-\frac{1}{2}}V_y(i_x, i_z-\frac{1}{2}) + Z_o\ {}_{n-\frac{1}{2}}I_z(i_x, i_z-\frac{1}{2}) \\
&\quad +{}_{n-\frac{1}{2}}V_y(i_x, i_z+\frac{3}{2}) - Z_o\ {}_{n-\frac{1}{2}}I_z(i_x, i_z+\frac{3}{2})]
\end{aligned} \tag{B.22}
$$

$$
\begin{aligned}
&-Z_o\ {}_{n+\frac{1}{2}}I_z(i_x, i_z+\frac{1}{2}) = \\
&\quad [-{}_nV_y(i_x, i_z) - Z_o\ {}_nI_z(i_x, i_z) + {}_nV_y(i_x, i_z+1) - Z_o\ {}_nI_z(i_x, i_z+1)] \\
&\quad -\frac{1}{2}[-{}_{n-\frac{1}{2}}V_y(i_x, i_z-\frac{1}{2}) - Z_o\ {}_{n-\frac{1}{2}}I_z(i_x, i_z-\frac{1}{2}) \\
&\quad +{}_{n-\frac{1}{2}}V_y(i_x, i_z+\frac{3}{2}) - Z_o\ {}_{n-\frac{1}{2}}I_z(i_x, i_z+\frac{3}{2})]
\end{aligned} \tag{B.23}
$$

$$
\begin{aligned}
&{}_{n+\frac{1}{2}}V_y(i_x+\frac{1}{2}, i_z) = \\
&\quad {}_nV_y(i_x, i_z) + Z_o\ {}_nI_x(i_x, i_z) + {}_nV_y(i_x+1, i_z) - Z_o\ {}_nI_x(i_x+1, i_z) \\
&\quad -\frac{1}{2}[{}_{n-\frac{1}{2}}V_y(i_x-\frac{1}{2}, i_z) + Z_o\ {}_{n-\frac{1}{2}}I_x(i_x-\frac{1}{2}, i_z) \\
&\quad +{}_{n-\frac{1}{2}}V_y(i_x+\frac{3}{2}, i_z) - Z_o\ {}_{n-\frac{1}{2}}I_x(i_x+\frac{3}{2}, i_z)]
\end{aligned} \tag{B.24}
$$

$$
\begin{aligned}
&Z_o\ {}_{n+\frac{1}{2}}I_x(i_x+\frac{1}{2}, i_z) = \\
&\quad [{}_nV_y(i_x, i_z) + Z_o\ {}_nI_x(i_x, i_z) - {}_nV_y(i_x+1, i_z) + Z_o\ {}_nI_x(i_x+1, i_z)] \\
&\quad -\frac{1}{2}[{}_{n-\frac{1}{2}}V_y(i_x-\frac{1}{2}, i_z) + Z_o\ {}_{n-\frac{1}{2}}I_x(i_x-\frac{1}{2}, i_z) \\
&\quad -{}_{n-\frac{1}{2}}V_y(i_x+\frac{3}{2}, i_z) + Z_o\ {}_{n-\frac{1}{2}}I_x(i_x+\frac{3}{2}, i_z)]
\end{aligned} \tag{B.25}
$$

Appendix C

Derivation of the Voltage and Current Relations in the 3D TLM Symmetrical Condensed Node Model

Again, similar to the 2D case (Appendix B), referred to Fig.2.7 ${}_{n+\frac{1}{2}}V_1^i(i_x, i_y - \frac{1}{2}, i_z)$ arrives at the node (i_x, i_y, i_z) at time $(n+1)\Delta t$ and is denoted as ${}_{n+1}V_1^i(i_x, i_y, i_z)$, and ${}_nV_1^r(i_x, i_y, i_z)$ arrives at the mid-point $(i_x, i_y - \frac{1}{2}, i_z)$ at time $(n+\frac{1}{2})\Delta t$ and is denoted as ${}_{n+\frac{1}{2}}V_1^r(i_x, i_y - \frac{1}{2}, i_z)$, that is: ${}_{n+\frac{1}{2}}V_1^i(i_x, i_y - \frac{1}{2}, i_z) = {}_{n+1}V_1^i(i_x, i_y, i_z)$, and ${}_{n+\frac{1}{2}}V_1^r(i_x, i_y - \frac{1}{2}, i_z) = {}_nV_1^r(i_x, i_y, i_z)$. Thus,

$$
\begin{aligned}
{}_{n+\frac{1}{2}}V_{x1}(i_x, i_y - \frac{1}{2}, i_z) &= {}_{n+1}V_1^i(i_x, i_y, i_z) + {}_nV_1^r(i_x, i_y, i_z) && \text{(C.1)} \\
{}_{n+\frac{1}{2}}I_{y1}(i_x, i_y - \frac{1}{2}, i_z) &= [{}_{n+1}V_1^i(i_x, i_y, i_z) - {}_nV_1^r(i_x, i_y, i_z)]/Z_0 && \text{(C.2)}
\end{aligned}
$$

Consequently, one has:

$$
\begin{aligned}
{}_{n+\frac{1}{2}}V_{x12}(i_x, i_y + \frac{1}{2}, i_z) &= {}_{n+\frac{1}{2}}V_{12}^r(i_x, i_y + \frac{1}{2}, i_z) + {}_{n+\frac{1}{2}}V_{12}^i(i_x, i_y + \frac{1}{2}, i_z) \\
&= {}_nV_{12}^r(i_x, i_y, i_z) + {}_{n+1}V_{12}^i(i_x, i_y, i_z) && \text{(C.3)}
\end{aligned}
$$

$$
\begin{aligned}
{}_{n+\frac{1}{2}}I_{y12}(i_x, i_y + \frac{1}{2}, i_z) &= [{}_{n+\frac{1}{2}}V_{12}^r(i_x, i_y + \frac{1}{2}, i_z) - {}_{n+\frac{1}{2}}V_{12}^i(i_x, i_y + \frac{1}{2}, i_z)]/Z_0 \\
&= [{}_nV_{12}^r(i_x, i_y, i_z) - {}_{n+1}V_{12}^i(i_x, i_y, i_z)]/Z_0 && \text{(C.4)}
\end{aligned}
$$

$$
\begin{aligned}
{}_{n+\frac{1}{2}}V_{x1}(i_x, i_y - \frac{1}{2}, i_z) &= {}_{n+\frac{1}{2}}V_1^i(i_x, i_y - \frac{1}{2}, i_z) + {}_{n+\frac{1}{2}}V_1^r(i_x, i_y - \frac{1}{2}, i_z) \\
&= {}_{n+1}V_1^i(i_x, i_y, i_z) + {}_{n}V_1^r(i_x, i_y, i_z) \qquad \text{(C.5)}
\end{aligned}
$$

$$
\begin{aligned}
{}_{n+\frac{1}{2}}I_{y1}(i_x, i_y - \frac{1}{2}, i_z) &= [{}_{n+\frac{1}{2}}V_1^i(i_x, i_y - \frac{1}{2}, i_z) - {}_{n+\frac{1}{2}}V_1^r(i_x, i_y - \frac{1}{2}, i_z)]/Z_0 \\
&= [{}_{n+1}V_1^i(i_x, i_y, i_z) - {}_{n}V_1^r(i_x, i_y, i_z)]/Z_0 \qquad \text{(C.6)}
\end{aligned}
$$

$$
\begin{aligned}
{}_{n+\frac{1}{2}}I_{z2}(i_x, i_y, i_z - \frac{1}{2}) &= [{}_{n+\frac{1}{2}}V_2^i(i_x, i_y, i_z - \frac{1}{2}) - {}_{n+\frac{1}{2}}V_2^r(i_x, i_y, i_z - \frac{1}{2})]/Z_0 \\
&= [{}_{n+1}V_2^i(i_x, i_y, i_z) - {}_{n}V_2^r(i_x, i_y, i_z)]/Z_0 \qquad \text{(C.7)}
\end{aligned}
$$

$$
\begin{aligned}
{}_{n+\frac{1}{2}}I_{z9}(i_x, i_y, i_z + \frac{1}{2}) &= [{}_{n+\frac{1}{2}}V_9^r(i_x, i_y, i_z + \frac{1}{2}) - {}_{n+\frac{1}{2}}V_9^i(i_x, i_y, i_z + \frac{1}{2})]/Z_0 \\
&= [{}_{n}V_9^r(i_x, i_y, i_z) - {}_{n+1}V_9^i(i_x, i_y, i_z)]/Z_0 \qquad \text{(C.8)}
\end{aligned}
$$

In the paper presented by Johns [14], scattered voltages are related to the incident voltages through a scattering matrix [S] at node (i_x, i_y, i_z):

$$
{}_{n}\mathbf{V}^r(i_x, i_y, i_z) = [\mathrm{S}] \quad {}_{n}\mathbf{V}^i(i_x, i_y, i_z) \qquad \text{(C.9)}
$$

with

$$
[\mathrm{S}] = \frac{1}{2}\begin{bmatrix}
 & 1 & 1 & & & & & 1 & & -1 & & \\
1 & & & & & 1 & & & -1 & & 1 & \\
1 & & & 1 & & & 1 & & & & -1 & \\
 & & 1 & & 1 & & -1 & & & 1 & & \\
 & & & 1 & & 1 & & -1 & 1 & & & \\
 & 1 & & & 1 & & 1 & & -1 & & & \\
 & & & -1 & & 1 & & 1 & & 1 & & \\
 & & 1 & & -1 & & 1 & & & & 1 & \\
1 & & & & & -1 & & & & 1 & & 1 \\
 & -1 & & & 1 & & 1 & & 1 & & & \\
-1 & & & 1 & & & & 1 & & & & 1 \\
 & 1 & -1 & & & & & & 1 & & 1 &
\end{bmatrix}
$$

The total voltages and circular currents at the nodes are also related to the incident voltages as follows:

$$
\begin{aligned}
{}_{n+1}V_x(i_x,i_y,i_z) &= \frac{2}{4}[{}_{n+1}V_1^i(i_x,i_y,i_z) + {}_{n+1}V_2^i(i_x,i_y,i_z) \\
&+ {}_{n+1}V_9^i(i_x,i_y,i_z) + {}_{n+1}V_{12}^i(i_x,i_y,i_z)] \qquad \text{(C.10)}
\end{aligned}
$$

$$
\begin{aligned}
{}_{n}V_x(i_x,i_y,i_z) &= \frac{2}{4}[{}_{n}V_1^i(i_x,i_y,i_z) + {}_{n}V_2^i(i_x,i_y,i_z) \\
&+ {}_{n}V_9^i(i_x,i_y,i_z) + {}_{n}V_{12}^i(i_x,i_y,i_z)] \qquad \text{(C.11)}
\end{aligned}
$$

$$
\begin{aligned}
{}_{n}I_{xy}(i_x,i_y,i_z) &= \frac{1}{2}[{}_{n}V_1^i(i_x,i_y,i_z) - {}_{n}V_3^i(i_x,i_y,i_z) \\
&+ {}_{n}V_{11}^i(i_x,i_y,i_z) - {}_{n}V_{12}^i(i_x,i_y,i_z)]/Z_o \qquad \text{(C.12)}
\end{aligned}
$$

where ${}_{n}I_{xy}(i_x,i_y,i_z)$ is the circular current on x-y plane at node (i_x,i_y,i_z).

Together with $Z_o = \sqrt{L/C}$, it is not difficult to show from the above equations:

$$
\begin{aligned}
2\,C\frac{{}_{n+1}V_x(i_x,i_y,i_z) - {}_{n}V_x(i_x,i_y,i_z)}{\Delta t} &= \\
-\frac{{}_{n+\frac{1}{2}}I_{y12}(i_x,i_y+\frac{1}{2},i_z) - {}_{n+\frac{1}{2}}I_{y1}(i_x,i_y-\frac{1}{2},i_z)}{\Delta l} & \\
-\frac{{}_{n+\frac{1}{2}}I_{z9}(i_x,i_y,i_z+\frac{1}{2}) - {}_{n+\frac{1}{2}}I_{z2}(i_x,i_y,i_z-\frac{1}{2})}{\Delta l} & \qquad \text{(C.13)}
\end{aligned}
$$

and

$$
\begin{aligned}
{}_{n}V_x(i_x,i_y,i_z) + Z_o\ {}_{n}I_{xy}(i_x,i_y,i_z) &= \\
\frac{[{}_{n+\frac{1}{2}}V_{x12}(i_x,i_y+\frac{1}{2},i_z) + Z_o\ {}_{n+\frac{1}{2}}I_{y12}(i_x,i_y+\frac{1}{2},i_z)]}{2} &+ \\
\frac{[{}_{n-\frac{1}{2}}V_{x1}(i_x,i_y-\frac{1}{2},i_z) + Z_o\ {}_{n-\frac{1}{2}}I_{y1}(i_x,i_y-\frac{1}{2},i_z)]}{2} &
\end{aligned}
\qquad \text{(C.14)}
$$

$$
\begin{aligned}
{}_{n}V_x(i_x,i_y+1,i_z) - Z_o\ {}_{n}I_{xy}(i_x,i_y+1,i_z) &= \\
\frac{[{}_{n+\frac{1}{2}}V_{x12}(i_x,i_y+\frac{1}{2},i_z) - Z_o\ {}_{n+\frac{1}{2}}I_{y12}(i_x,i_y+\frac{1}{2},i_z)]}{2} &+ \\
\frac{[{}_{n-\frac{1}{2}}V_{x12}(i_x,i_y+\frac{3}{2},i_z) - Z_o\ {}_{n-\frac{1}{2}}I_{y12}(i_x,i_y+\frac{3}{2},i_z)]}{2} &
\end{aligned}
\qquad \text{(C.15)}
$$

From above, one can have:

$$
\begin{aligned}
&{}_{n+\frac{1}{2}}V_{x12}(i_x, i_y+\frac{1}{2}, i_z) = \\
&\quad {}_nV_x(i_x, i_y, i_z) + Z_o\ {}_nI_{xy}(i_x, i_y, i_z) + {}_n\,V_x(i_x, i_y+1, i_z) - Z_o\ {}_nI_{xy}(i_x, i_y+1, i_z) \\
&\quad -\frac{1}{2}[{}_{n-\frac{1}{2}}V_{x1}(i_x, i_y-\frac{1}{2}, i_z) + Z_o\ {}_{n-\frac{1}{2}}I_{y1}(i_x, i_y-\frac{1}{2}, i_z) \\
&\quad +{}_{n-\frac{1}{2}}V_{x12}(i_x, i_y+\frac{3}{2}, i_z) - Z_o\ {}_{n-\frac{1}{2}}I_{y12}(i_x, i_y+\frac{3}{2}, i_z)] \qquad \text{(C.16)}
\end{aligned}
$$

$$
\begin{aligned}
&-Z_o\ {}_{n+\frac{1}{2}}I_{y12}(i_x, i_y+\frac{1}{2}, i_z) = \\
&\quad -{}_nV_x(i_x, i_y, i_z) - Z_o\ {}_nI_{xy}(i_x, i_y, i_z) + {}_n\,V_x(i_x, i_y+1, i_z) - Z_o\ {}_nI_{xy}(i_x, i_y+1, i_z) \\
&\quad -\frac{1}{2}[-{}_{n-\frac{1}{2}}V_{x1}(i_x, i_y-\frac{1}{2}, i_z) - Z_o\ {}_{n-\frac{1}{2}}I_{y1}(i_x, i_y-\frac{1}{2}, i_z) \\
&\quad +{}_{n-\frac{1}{2}}V_{x12}(i_x, i_y+\frac{3}{2}, i_z) - Z_o\ {}_{n-\frac{1}{2}}I_{y12}(i_x, i_y+\frac{3}{2}, i_z)] \qquad \text{(C.17)}
\end{aligned}
$$

Bibliography

[1] Itoh et. al.,"Numerical techniques for passive microwave and millimeter-wave structures", edited by T. Itoh, *Johns Wiley & Sons, Inc.,* New York, 1989

[2] H. L. Bertoni and L. B. Felsen et. al.,"Directions in Electromagnetic Wave Modeling", edited by H. L. Bertoni and L. B. Felsen, *Plenum Press,* New York, 1991

[3] P. B. Johns and R. L. Beurle, "Numerical solution of 2-dimensional scattering problems using a transmission-line matrix", *Proc. Inst. Elec. Eng.,* Vol. 118, No.9, pp. 1203-1208, Sept. 1971.

[4] J. R. Whinnery and S. Ramo, "A new approach to the solution of high frequency field problems," *Proc. IRE,* Vol. 32, pp. 282-288, May 1944.

[5] G. Kron, "Equivalent circuit of the field equations of Maxwell-I," *Proc. IRE* Vol. 32, pp. 289-299, May 1944.

[6] J. R. Whinnery, C. Concordia and G. Kron "Network analyzer studies of electromagnetic cavity resonators," *Proc. IRE.* Vol. pp. 360-367, June 1944.

[7] P. B. Johns , "A new mathematical model to describe the physics of propagation ", *The Radio and Electronic Engineer,* Vol. 44, No.12, pp. 657-666, Dec. 1974.

[8] S. Akhtarzad and P. B. Johns , "Solution of 6-component electromagnetic fields in three space dimensions and time by the TLM method", *Electron. Lett.,* Vol. 10, pp. 535-537, Dec. 12, 1975.

[9] S. Akhtarzad and P. B. Johns , "The solution of Maxwell's equations in three space dimensions and time by the TLM method of numerical analysis", *Proc. Inst. Elec. Eng.,* Vol. 122, No.12, pp. 1344-1348, Dec. 1975.

[10] P. Saguet and E. Pic, "Utilisation d'un nouveau type de noeud dans la method TLM en 3 dimensions," *Electron. Lett.*, Vol. 18, No.11, pp. 478-480, May 1982.

[11] P. Saguet and S. Tedjini , "Method des lignes de transmission en trois dimensions: modefications du processus de simulation," *Ann. Telecommun.*, Vol. 40, Nos. 3-4, pp. 1-8, Mar.-Apr. 1985.

[12] A. Amer , "Condensed node TLM method and its application to transmission in power system," *Ph.D Thesis*, Nottingham University, 1980.

[13] P. B. Johns , "Use of condensed and symmetrical TLM nodes in computer-aided electromagnetic design," *IEE Proceedings*, Pt. H, Vol. 133, pp. 368-374, 1986

[14] P. B. Johns, "A symmetrical condensed node for the TLM method," *IEEE Trans. on Microwave Theory Tech.*, Vol. MTT-35, No.4 , pp. 370-377, April, 1987.

[15] P. Naylor and R. A. Desai, "New three dimensional symmetrical condensed lossy node for solution of electromagnetic wave problems by TLM," *Electron. Lett.*, Vol. 26, No. 7, pp. 492-494, March 29. 1990.

[16] A. Al-Mukhtar and J. E. Sitch , "Transmission-line Matrix method with irregularly graded space," *Proc. Inst. Elec. Eng.*, Vol. 128, pt. H, No. 6, pp. 299-305, Dec. 1981.

[17] P. Saguet and E. Pic, "Le Maillage rectangulaire at le changement de maille dans la methode en deux dimensions," *Electron Lett.*, Vol. 17, No. 7, pp. 277-278, April 1981

[18] R. Scaramuzza and A. J. Lowery, "Hybrid symmetrical condensed node for the TLM method," *Electron Lett.*, Vol. 26, No. 23, pp. 1947-1949, Nov. 1990

[19] D. H. Choi and W. J. R. Hoefer , "The simulation of three-dimensional wave propagation by a scalar TLM method," *IEEE MTT Symposium Digest*, May 1984.

[20] C. Shin and W. J. R. Hoefer , "Dominant and second-order mode cutoff frequencies in fin lines calculated with a two dimensional TLM method," *IEEE Trans. Microwave Theory Tech.* , Vol. MTT-28, No. 12, pp. 1443-1448, Dec. 1980.

[21] P. B. Johns and S. Akhtarzad, "The use of time domain diakoptics in time discrete models of fields," *Int. J. Numer. Methods Eng.*, 17, pp. 1-14, 1981

[22] P. B. Johns and S. Akhtarzad, "Time-domain approximations in the solution of fields by time domain diakoptics," *Int. J. Numer. Methods Eng.*, 18, pp.1361-1373,1982

[23] G. Mariki and C. Yeh, "Dynamic three-dimensional TLM analysis of microstrip lines on anisotropic substrates," *IEEE Trans. Microwave Theory Tech.*, Vol. MTT-33, No. 9, pp. 789-799, Sept. 1985.

[24] P. B. Johns and M. O'Brien , "Use of transmission line modeling (T,L.M.) method to solve nonlinear lumped networks," *Radio Electron. Eng.*, Vol. 50, Nos. 1-2, pp. 59-70, 1980

[25] W. J. R. Hoefer, "The transmission-line matrix method-theory and applications", *IEEE Trans. on Microwave Theory Tech.*, Vol. MTT-33, pp. 882-893, Oct. 1985.

[26] W. J. R. Hoefer, "The discrete time domain Green's function or Johns matrix-a new powerful concept in transmission line modelling," *International Journal of Numerical Modelling : Electronic Networks, Devices and Fields*, Vol.2, No.4, pp.215-225, 1990

[27] Eswarappa and W. J. R. Hoefer, "Application of time domain diakoptics to 3-D TLM method with symmetrical condensed nodes," *1990 IEEE-AP Symposium and URSI Meeting*, Dallas, Tx, U.S.A., May 7-11, 1990

[28] Eswarappa, "New developments in the transmission line matrix and the finite element methods for numerical modelling of microwave and millimeter-wave structures," *Ph.D Thesis*, University of Ottawa, Ottawa, Ontario, 1990

[29] P. So, Eswarappa and W. J. R. Hoefer, "A two-dimensional TLM microwave field simulator using new concepts and procedures," *IEEE Trans. on Microwave Theory Tech.*, Vol. MTT-37, pp.1877-1883, Dec. 1989

[30] Eswarappa, G. I. Costache and W. J. R. Hoefer, "TLM modelling of dispersive wide-band absorbing boundaries with time domain diakoptics for S-parameters extraction," *IEEE Trans. on Microwave Theory Tech.*, Vol. MTT-41, April 1990

[31] R. Ait-Sadi, A. J. Lowery and B. Tuck "Combined fine-coarse mesh transmission-line modelling method for diffusion problems," *International Journal of Numerical Modelling : Electronic Networks, Devices and Fields*, Vol.3, pp. 111-126, 1990

[32] J. L. Dubard, D. Pompei, J. Le Roux and A. Papiernik "Characterization of microstrip antennas using the TLM simulation associated a Prony-Pisarenko method," *International Journal of Numerical Modelling : Electronic Networks, Devices and Fields*, Vol.3, pp. 269-285, 1990

[33] S. A. Kosmopoulous, W. J. R. Hoefer and A. Gagnon, "Non-linear TLM modelling of high-frequency varactor multipliers and halvers," *Intl. J. Infrared Millimeter Waves*, Vol.10, No.3, pp. 343-352, Mar. 1989.

[34] P. Russer, P. So and W. J. R. Hoefer , "Modelling of nonlinear active regions in TLM," *IEEE Trans. Microwave Guided Wave Lett.* , Vol.1, No.1, pp. 10-13, Jan. 1991.

[35] F. H. Bellamine and E. F. Kuester, "Development of a frequency-dependent TLM," *1991 North American Radio Science Meeting Digest,*, pp. 78, June, 1991, London, Ontario

[36] N. R. S. Simons, A. A. Sebak and Y. M. M. Antar, "Two dimensional hexagonal TLM node and velocity error correction," *1991 IEEE Antennas and Propagation Symposium Digest,*, pp. 902-905, June, 1991, London, Ontario

[37] R. Sorrentino, P. So and W. J. R. Hoefer, "Numerical microwave synthesis by inversion of the TLM process," *21st European Microwave Conference Dig.*, Stuttgart, Germany, Sept. 1991

[38] P. B. Johns, "Application of the transmission-line matrix method to homogeneous waveguides of arbitrary cross-section", *Proc. Inst. Elec. Eng.*, Vol. 119, No.8, pp. 1086-1091, Aug. 1972.

[39] P. B. Johns, "The solution of inhomogeneous waveguide problems using transmission-line matrix", *IEEE Trans. on Microwave Theory Tech.*, Vol. MTT-22, pp. 209-215, Mar. 1974.

[40] K. Akhtarzad and P. B. Johns , "Numerical solution of lossy waveguides: T.L.M. computer program," *Electron Lett.*, Vol. 10, No. 15, pp. 309-311, July 25, 1974.

[41] K. Akhtarzad and P. B. Johns , "TLM analysis of the dispersion characteristics of microstrip lines on magnetic substrates using 3-dimensional resonators," *Electron Lett.*, Vol. 11, No. 6, pp. 130-131, Mar. 1975.

[42] K. Akhtarzad and P. B. Johns , "Three-dimensional transmission-line matrix computer analysis of microstrip resonators," *IEEE Trans. Microwave Theory Tech.*, Vol. MTT-23, No. 12, pp. 990-997, Dec. 1975.

[43] K. Akhtarzad and P. B. Johns , "Generalized elements for T.L.M. method of numerical analysis," *Proc. Inst. Elec. Eng.*, Vol. 122, No. 12, pp. 1349-1352, Dec. 1975.

[44] J. E. Sitch and P. B. Johns , "Transmission-line matrix analysis of continuous waveguiding structures using stepped-impedance cavities,"

Microwave, Opt. and Acoustics, 1977, 1, (5), pp. 181-184

[45] P. Saguet and E. Pic, "An improvement for the TLM method," *Electron Lett.* , Vol. 16, No. 7, pp. 247-248, May 1980.

[46] Y. Shih and W. J. R. Hoefer, "The accuracy of TLM analysis of finned rectangular waveguides," *IEEE Trans. Microwave Theory Tech.*, Vol. MTT-28, No.7, pp.743-746, July 1980.

[47] R. Allen, A. Mallik and P. B. Johns , "Numerical results for the symmetrical condensed TLM node," *IEEE Trans. Microwave Theory Tech.* , Vol. MTT-35, pp. 378-382, Dec. 1987.

[48] P. Saguet and W. J. R. Hoefer , "The modelling of multiaxial discontinuities in quasi-planar structures with the modified TLM method," *International Journal of Numerical Modelling: Electronic Networks, Devices and Fields,* Vol. 1, pp. 7-17, 1988.

[49] H. Meliani, D. De Cogan and P. B. Johns "The use of orthogonal curvilinear meshes in TLM models," *International Journal of Numerical Modelling: Electronic Networks, Devices and Fields,* Vol. 1, pp. 221-238, 1988.

[50] P. Saguet , "The 3D transmission-line matrix method: theory and comparison of the process," *International Journal of Numerical Modelling: Electronic Networks, Devices and Fields,* Vol. 2, pp. 191-201, 1989.

[51] F. J. German, G. K. Gothard, L. S. Riggs and P. M. Goggans , "The calculation of radar cross-section (RCS) using the TLM method," *International Journal of Numerical Modelling: Electronic Networks, Devices and Fields,* Vol. 2, pp. 267-278, 1989.

[52] F. J. German, G. K. Gothard, L. S. Riggs and P. M. Goggans , "The calculation of radar cross-section (RCS) using the TLM method," *International Journal of Numerical Modelling: Electronic Networks, Devices and Fields,* Vol. 2, pp. 267-278, 1989.

[53] A. H. M. Saleh , "Analysis of acoustic radiation patterns of array transducers using the TLM method," *International Journal of Numerical Modelling: Electronic Networks, Devices and Fields,* Vol. 3, pp. 39-56, 1990.

[54] S. H. Pulko, I. A. Halleron and C. P. Phizacklea , "Substructuring of space and time in TLM diffusion applications," *International Journal of Numerical Modelling: Electronic Networks, Devices and Fields,* Vol. 3, pp. 207-214, 1990.

[55] K. S. Yee, "Numerical solution of initial boundary value problems involving Maxwell's equations," *IEEE Trans. on Antennas and Propagation,* Vol. AP-14, No. 3,pp. 302-307 , May, 1966.

[56] A. Taflove and M, E. Brodwin, "Numerical solution of steady-state electromagnetic scattering problems using the time-dependent Maxwell's equations," *IEEE Trans. on Microwave Theory Tech.,* Vol. MTT-23, No. 8, , pp. 623-630, Aug. 1975.

[57] A. Taflove and K. R. Umashankar, "The Finite-Difference Time-Domain (FD-TD) Method for electromagnetic scattering and interaction problems," *Journal of Electromagnetic Waves and Applications,* Vol. 1, No. 3, pp. 243-267, Mar. 1987.

[58] X. Zhang and K. Mei, "Time domain finite difference approach for the calculation of the frequency-dependent characteristic of microstrip discontinuities," *IEEE Trans. on Microwave Theory Tech.,* Vol. MTT-36, No. 12, pp. 1775-1787, Dec., 1987.

[59] A. Taflove, "Review of the formulation and application of the finite-difference time-domain method for numerical modelling of electromagnetic wave interactions with arbitrary structures," *Wave Motion,* 10, pp. 547-582, 1988, North-Holland.

[60] A. Taflove and K. R. Umashankar "Finite-Difference Time-Domain Solution of Maxwell's Equations," *1991 PIERS Proceedings,* pp. 84, Boston, 1991

[61] P. B. Johns and G. Butler, "The consistency and accuracy of the TLM method for diffusion and its relationship to existing methods," *Int. J. Numerical Methods Eng.,* Vol. 19 , pp. 1549-1554, 1983.

[62] P. B. Johns, "On the relation between TLM method and Finite-Difference Methods for Maxwell's equations," *IEEE Trans. on Microwave Theory Tech.,* Vol. MTT-35, No.1 , pp. 60-61, Jan. 1987.

[63] R. H. Voelker and R. J. Lomax, "A finite-difference transmission line matrix method incorporating a nonlinear device model," *IEEE Trans. on Microwave Theory Tech.,* Vol. MTT-38, No.3 , pp. 302-312, Mar. 1990.

[64] P. B. Johns, "Simulation of electromagnetic wave interactions by transmission-line modelling (TLM)," *Wave Motion,* No. 10, pp. 597-610, 1988.

[65] D. H. Choi, "A comparison of the dispersion characteristics associated with the TLM and FD-TD methods," *International Journal of Numerical Modelling: Electronic Network, Devices and Fields,* Vol. 2, pp. 203-214, 1989.

[66] J. Nielsen and W. J. R. Hoefer, "A complete dispersion analysis of the condensed node TLM mesh," *4th Biennial IEEE Conference on Electromagnetic Field Computation Digest,* Toronto, Ontario, Oct. 1990

[67] W. J. R. Hoefer, "The transmission line matrix (TLM) method", Chapter 8 of "Numerical techniques for passive microwave and millimeter-wave structures", edited by T. Itoh, *Johns Wiley & Sons, Inc.,* New York, 1989 pp. 486-591

[68] W. J. R. Hoefer, "TLM modelling of electromagnetic fields", International Workshop of the German IEEE MTT/AP Joint Chapter and the German IEEE CAD Chapter on *Discrete Time Domain Modelling of Electromagnetic Fields and Networks,* Munich, Oct. 1991

[69] N. R. S. Simons and E. Bridges, "Method for modelling free space boundaries in TLM simulations," *Electronics Letters*, Vol.26, No.7, 29th March, 1990

[70] N. R. S. Simons and E. Bridges, "Application of absorbing boundary conditions to TLM simulations," *1990 IEEE International Antennas and Propagation Symposium Digest,* pp.2-1, 1990

[71] J. H. Chen, "Numerical boundary conditions and computational modes," *Journal of Computational Physics,* 13, pp. 522-535, 1973

[72] W. D. Smith, "A nonreflecting plane boundary for wave propagation problems," *Journal of Computational Physics,* 15, pp. 492-503, 1974

[73] E. L. Lindman, "'Free-space' boundary conditions for the time dependent wave equations," *Journal of Computational Physics,* 18, pp. 66-78, 1975

[74] L. N. Trefethen and L. Halpern, "Well-posedness of one-way equations and absorbing boundary conditions," *Mathematics of Computations,* Vol. 47, No. 176, pp. 421-435, Oct. 1976

[75] B. Engquist and A. Majda, "Radiation boundary conditions for acoustic and elastic wave calculations," *Communications on Pure and Applied Mathematics,* Vol. XXXII, pp. 313-357, 1979

[76] B. Engquist and A. Majda, "Absorbing boundary conditions for the numerical simulation of waves," *Math. Comp.,* 15, Vol. 31, pp. 313-354, 1979

[77] G. Mur, "Absorbing boundary conditions for the finite-difference approximation of the time-domain electromagnetic-field equations, " *IEEE Trans. Electromag. Compact.,* Vol. EMC-23, No. 4, pp. 377-382, 1981

[78] R. M. Beam, R. F. Warming and H. C. Yee, "Stability analysis of numerical boundary conditions and implicit difference approximations for hyperbolic equations," *Journal of Computational Physics,* 48, pp. 200-222, 1982

[79] Z. Liao, L. Wong, B. Yang and Y. Yuan, "A transmitting boundary for transient wave analysis," *Scientia Sinica (Series A),* Vol. XXVII, No. 10, pp. 1062-1076, Oct. 1984

[80] R. G. Keys, "Absorbing boundary conditions for acoustic media," *Geophysics,* Vol. 50, No. 6, pp. 892-902, June 1985

[81] R. L. Higdon, "Absorbing boundary conditions for difference approximations to the multi-dimensional wave equation," *Math. Comp.,* Vol. 47, No. 176, pp. 437-459, Oct. 1986

[82] R. L. Higdon, "Numerical absorbing boundary conditions for the wave equation", *Math. Comp.,* Vol. 49, No. 179, pp. 65-91, July 1987

[83] J. G. Blaschak and G. A. Kriegsmann, "A comparative study of absorbing boundary conditions," *Journal of Computational Physics,* 77, pp. 109-139, 1988

[84] L. Halpern, "Wide-angle one-way equations," *J. Acoust. Soc.,* Am. 84(4), pp. 1397-1404, Oct. 1988

[85] A. Bamberger, P. Joly and J. E. Roberts "Second-order absorbing boundary conditions for the wave equation: a solution for the corner problem ," *1990 SIAM,* Vol. 27, No. 2, pp. 323-352, 1990

[86] Hong Jiang, "Absorbing boundary conditions for second-order hyperbolic equations," *Journal of Computational Physics*, 88, pp.205-231, 1990

[87] J. Fang, "Time-domain finite-difference computation for Maxwell's equations," *Ph.D Dissertation, University of California at Berkeley,* 1989

[88] P. Saguet, "TLM method for the three dimensional analysis of microwave and mm-wave structures", *International Workshop of the German IEEE MTT/AP chapter on CAD Oriented Numerical Techniques For the Analysis of Microwave and MM-Wave Transmission-Line Discontinuities and Junctions*, Stuttgart, Germany, Sept. 13, 1991

[89] T. G. Moore, J. G. Blashchak, A. Taflove and G. A. Kriegsmann, "Theory and application of radiation boundary operators," *IEEE Trans. Antennas and Propagation,* Vol. AP-36, No. 12, pp. 1797-1811, Dec. 1988

[90] J. Nielsen "Spurious modes of the TLM-condensed node formulation", *IEEE Trans. Microwave and Guided Wave Letters*, Vol.1, No.8, Aug. 1991, pp. 201-203

[91] A. Taflove and K. Umashankar, "Solution of complex electromagnetic penetration and scattering problems in unbounded regions," *Computational Methods for Infinite Domain Media-Structure Interaction*, AMD-Vol. 46, pp.83-113, Nov. 1981

[92] K. Umashankar and A. Taflove, "A novel method to analyze electromagnetic scattering of complex objects," *IEEE Trans. Electromagnetic Compatibility*, Vol. EMC-24, No. 4, pp. 397-405, Nov. 1982

[93] A. Taflove and K. Umashankar, "Radar cross section of general three-dimensional scatterers," *IEEE Trans. Electromagnetic Compatibility*, Vol. EMC-25, No. 4, pp. 433-440, Nov. 1983

[94] A. Taflove and K. Umashankar, B. Beker, F. Harfoush and Y. S. Yee "Detailed FD-TD analysis of electromagnetic fields penetrating narrow slots and lapped joints in thick conducting screens," *IEEE Trans. Antennas Propagat.*, Vol. AP-36, pp. 247-257, 1988

[95] R. F. Harrington, "Time-harmonic electromagnetic fields", *McGraw-Hill*, New York, 1961

[96] Vaclav Cizek, "Discrete Fourier Transform and Their Applications", *Bristol, Hilger*, 1986

[97] Charles W. Harrison, JR., "Transient electromagnetic field propagation through infinite sheets, into spherical shells, and into hollow cylinders", *IEEE Trans. on Antennas and Propagation*, Vol.AP-12, pp. 319-334, May, 1964

[98] Z. Chen, M. M. Ney and W. J. R. Hoefer, "A new boundary description in two-dimensional TLM models of microwave circuits", *IEEE Trans. Microwave Theory and Techniques*, Vol. MTT-39, No.3, pp.377-382, Mar. 1991

[99] Z. Chen, W. J. R. Hoefer and M. M. Ney, "A new procedure for interfacing the Transmission Line Matrix (TLM) method with frequency-domain solutions", *IEEE Trans. Microwave Theory and Techniques*, Vol. MTT-39, No.10, pp. 1788-1791, Oct. 1991

[100] Z. Chen, M.M. Ney and W. J. R. Hoefer, "A new finite-difference time-domain formulation and its equivalence with the TLM symmetrical condensed node", *IEEE Trans. Microwave Theory and Techniques*, Vol. MTT-39, No.12, Dec. 1991